

**Titre:** Fatigue Crack Propagation Under Variable Amplitude Loading in Steels Used in Francis Turbine Runners  
Title:

**Auteur:** Meysam Hassanipour  
Author:

**Date:** 2017

**Type:** Mémoire ou thèse / Dissertation or Thesis

**Référence:** Hassanipour, M. (2017). Fatigue Crack Propagation Under Variable Amplitude Loading in Steels Used in Francis Turbine Runners [Ph.D. thesis, École Polytechnique de Montréal]. PolyPublie. <https://publications.polymtl.ca/2814/>  
Citation:

 **Document en libre accès dans PolyPublie**  
Open Access document in PolyPublie

**URL de PolyPublie:** <https://publications.polymtl.ca/2814/>  
PolyPublie URL:

**Directeurs de recherche:** Sylvain Turenne, & Jacques Lanteigne  
Advisors:

**Programme:** Génie mécanique  
Program:

ÉCOLE POLYTECHNIQUE DE MONTRÉAL

FATIGUE CRACK PROPAGATION UNDER VARIABLE AMPLITUDE LOADING IN  
STEELS USED IN FRANCIS TURBINE RUNNERS

MEYSAM HASSANIPOUR

DÉPARTEMENT DE GÉNIE MÉCANIQUE  
ÉCOLE POLYTECHNIQUE DE MONTRÉAL

THÈSE PRÉSENTÉE EN VUE DE L'OBTENTION  
DU DIPLÔME DE PHILOSOPHIAE DOCTOR  
(GÉNIE MÉCANIQUE)

OCTOBRE 2017

UNIVERSITÉ DE MONTRÉAL

ÉCOLE POLYTECHNIQUE DE MONTRÉAL

Cette thèse intitulée :

FATIGUE CRACK PROPAGATION UNDER VARIABLE AMPLITUDE LOADING IN  
STEELS USED IN FRANCIS TURBINE RUNNERS

présentée par : HASSANIPOUR Meysam

en vue de l'obtention du diplôme de : Philosophiae Doctor

a été dûment acceptée par le jury d'examen constitué de :

M. VADEAN Aurelian, Doctorat, président

M. TURENNE Sylvain, Ph. D., membre et directeur de recherche

M. LANTEIGNE Jacques, Ph. D., membre et codirecteur de recherche

Mme BROCHU Myriam, Ph. D., membre

M. LAROUCHE Daniel, Ph. D., membre externe

## **DEDICATION**

I hereby dedicate this thesis  
to everyone who contributes to  
better understanding of  
the phenomena in this universe.

## ACKNOWLEDGEMENTS

First of all, I would like to thank Yves Verreman, who is more than just a supervisor for me; He taught me how to conduct research, how to think, and how to express myself. He helped me to gain knowledge in this field and also contributed to my writing and speaking skills. I am grateful to have him as a supervisor and thankful for his great contribution to this thesis.

I would also like to thank senior researcher, Jacques Lanteigne, who co-supervised me and gave me access to the facilities at Institut de Recherche d'Hydro-Québec (IREQ), Hydro-Québec's research center. Jianqiang Chen had a remarkable contribution in the beginning of this project and helped me to plan and develop the experimental program, so I am grateful to him for his help. I would like to thank Carlo Baillargeon who always found time to help me regarding problems that I encountered with the hydraulic machines during my 2-year experimental program at IREQ. I would also like to thank Stéphane Godin who supported me morally and scientifically while I was conducting my experiments. I am also thankful for the help and support I received from other researchers and technicians at IREQ.

I am grateful to the Natural Science and Engineering Research Council of Canada, Alstom Renewable Power Canada and Hydro-Québec Research Institute for their support.

Finally, I would like to thank my family who supported from a big distance. My dear friends Matjaz Panjan and Pierre Schell who put their time on reading and correcting some parts of this manuscript. I appreciate the help and encouragement of my beautiful friends in Montreal that kept me motivated during these 6 years. Thanks to my new friends here in Japan, especially Fransisca van Esterik and Ziane Izri, for their support and encouragement to reach the end of the line.

## RÉSUMÉ

Les turbines hydrauliques sont soumises à de très grands nombres de cycles à faible amplitude de contrainte et à haute fréquence. Ces petits cycles sont générés par des phénomènes hydrauliques et sont superposés à une contrainte statique de tension. Aussi, dépendant des conditions de fonctionnement, il est possible d'avoir superposé aux petits cycles un plus faible nombre de grands cycles à forte amplitude de contrainte et basse fréquence. On a ainsi en pratique une superposition de petits cycles, de grands cycles et d'une contrainte statique de tension durant les 70 ans de durée de vie de la turbine.

Les turbines hydrauliques qui sont fabriquées à partir des aciers AISI 415, ASTM A516, et AISI 304L (notés 415, A516, et 304L pour simplification) sont soumises à de telles contraintes cycliques et statique. Ces contraintes ont pour effet de favoriser la propagation des défauts existants dans les roues des turbines et peuvent mener à leur rupture.

Pour éviter la propagation des fissures, les petits cycles doivent induire un  $\Delta K$  qui est en dessous du seuil de fatigue. Néanmoins, les grands cycles peuvent contribuer à propager ces fissures. Ainsi, pour prédire la vitesse de propagation des fissures dans de telles conditions de cycles superposés, on a recours à la sommation linéaire de dommage (SLD). Il a été observé que les grands cycles superposés aux petits cycles peuvent induire une diminution du seuil de fatigue des petits cycles.

Différentes procédures ont été proposées dans la littérature pour mesurer les seuils associés aux petits cycles seuls et avec superposition des grands cycles. Cependant, la plupart des procédures ne minimise pas la fermeture induite lors de la mesure du seuil conduisant ainsi à une surestimation de leur valeur. La présente étude propose de nouvelles procédures d'essais pour réduire la fermeture lors de la mesure du seuil de fatigue pour les aciers mentionnés précédemment. De plus, différentes études ont démontré que les fissures peuvent se propager plus rapidement sous l'effet des grands cycles que ce que prédit la SLD. Nous vérifierons ainsi la précision de la prédiction LDS par rapport aux mesures de propagation.

Dans une première étude, la propagation des fissures par l'interaction de petits et de grands cycles est caractérisée dans les trois aciers. Les cycles de base sont entrecoupés par les grands cycles. Les vitesses de propagation des fissures par les cycles de base et les grands cycles de sous-charge sont additionnées dans la SLD pour évaluer la vitesse de propagation de fissure. Les mesures expérimentales de vitesse de propagation en sous-charge périodiques sont ensuite comparées avec

la prévision de la SLD. Le ratio entre la mesure de propagation de fissure et la prédiction SLD est définie comme facteur d'accélération.

Les résultats montrent que les mesures de propagation par les sous-charges périodiques dans l'acier 415 sont proches de celles déterminées par la méthode de SLD. Cependant, le facteur d'accélération est égal à trois dans l'acier 304L. Des valeurs intermédiaires sont obtenues pour l'acier A516. On montre que le facteur d'accélération est directement relié au coefficient d'écrouissage de chacun des aciers. En ordre croissant, l'acier 415 a le plus faible coefficient d'écrouissage, suivi par l'acier A516 et par l'acier 304L.

Les observations fractographiques montrent que la sous-charge cause une accélération de la propagation de fissure pendant les cycles de base. La cause de cette accélération est attribuée à une combinaison de contrainte résiduelle en tension et d'écrouissage causée par les sous-charges.

Une deuxième étude avait pour but de mesurer le seuil de fatigue des petits cycles (cycles de base) et de vérifier comment il pouvait être diminué par la superposition de grands cycles (sous-charges périodiques). Les essais de fatigue de cette seconde étude ont été réalisés dans la région du seuil de propagation sur les aciers avec le plus petit et le plus grand facteur d'accélération, soit les aciers 415 et 304L respectivement.

Le ratio de nombre de cycles de base sur nombre de sous-charges est noté  $n$ . Deux procédures d'essais ont été réalisés. Le premier a été réalisé par une réduction de  $\Delta K$  pour mesurer un seuil conventionnel,  $\Delta K_{th,conv}$ , de  $2 \times 10^{-7}$  mm/cycle en amplitude constante et avec les sous-charges périodiques avec différents  $n$ . Le deuxième procédé a été réalisé par une croissance de  $\Delta K_{BL}$  de zero avec les sous-charge periodiques pour  $n = 1.25 \times 10^3$  pour atteindre un seuil réel,  $\Delta K_{th,true}$ , avec une vitesse de propagation de  $6.7 \times 10^{-9}$  mm/cycle et ensuite  $\Delta K_{th,conv}$ .

Le seuil de fatigue des petits cycles ne décroît pas pour  $n > 1.25 \times 10^5$ . Le nombre de petits cycles est de l'ordre de  $7 \times 10^{10}$  pendant une durée de vie de 70 ans. Le nombre de grands cycles ne doit donc pas dépasser  $5.6 \times 10^5$  cycles. Lorsque  $n < 10^5$ , le seuil de fatigue commence à décroître. Cette décroissance est moins importante dans le 415 que dans le 304L. Il a été démontré que le seuil de fatigue décroît 5 fois plus quand la vitesse de propagation est en dessous de  $6.7 \times 10^{-9}$  mm/cycle par rapport à  $2 \times 10^{-7}$  mm/cycle.

Les contraintes résiduelles de tension sont induites dans les roues lors de la fabrication et du soudage. Ces contraintes augmentent le facteur d'intensité de contrainte maximal,  $K_{max}$ , induit aux défauts et peuvent favoriser la propagation des fissures. L'effet d'une augmentation de  $K_{max}$  sur le

seuil de fatigue en amplitude constante et sous-charges périodiques doit être étudiée. Il a été démontré qu'une augmentation de  $K_{\max}$  décroît légèrement les deux seuils.

## ABSTRACT

Hydraulic turbine runners are subjected to a very large number of cycles with small stress amplitudes at high frequencies. These cycles are generated by hydraulic phenomena and are superimposed to a tensile static stress. Depending on the operating conditions, much lower number of large cycles are generated with large stress amplitudes at low frequencies. As a summary, the whole stress spectrum consists of small cycles superimposed to a tensile static stress that is intercut with large cycles during the 70 years design life of turbine runners.

Turbine runners, which are fabricated from AISI 415, ASTM A516, and AISI 304L steels (i.e. called 415, A516 and 304L for simplicity), are subjected to the aforementioned stress cycles. The imposed stress spectrum propagates the existing defects or cracks in turbine runners and may lead to their failure.

In order to avoid crack propagation, the small cycles should induce a  $\Delta K$  that is lower than the fatigue threshold. Nonetheless, the crack can grow due to large cycles. As a result, linear damage summation (LDS) is employed to predict the crack growth. The large cycles superimposed to small cycles can also induce a decrease in fatigue threshold of the small cycles.

Different test procedures have been proposed to measure the fatigue threshold of small cycles and the ones superimposed to large cycles; however, most of them do not minimize the crack closure while reaching the fatigue threshold leading to an overestimation of fatigue thresholds. In this study new test procedures are proposed in order to minimize crack closure while reaching the fatigue thresholds in turbine runner steels. Different studies have shown that crack can grow faster than the LDS prediction due to the interaction between large cycles. Therefore, we verify the precision of LDS prediction compared to the measured crack growth rates.

In this first study, crack growth due to the interaction between two large cycles is investigated in the three aforementioned turbine runner steels. Baseline cycles are periodically intercut by an underload cycle. This variable amplitude loading is hereafter called periodic underloads. Crack growth rates of baseline cycles and underload cycles are summated in LDS to predict crack growth under periodic underloads. Crack growth measured under periodic underloads is then compared to LDS prediction. A ratio between the measured and predicted crack growth, that is greater than unity, is defined as an acceleration factor.

Results show that the measured crack growths under periodic underloads in the 415 steel are close to the ones predicted by LDS. On the other hand, the acceleration factor in the 304L steel can reach

up to three. Intermediate values are obtained for the A516 steel. We show that there is a direction relationship between the strain hardening exponent and the acceleration factors in each steel. In increasing order, the 415 steel has the lowest monotonic strain hardening exponent, followed by A516 and 304L steels.

The fractography analysis showed that an underload followed by baseline cycles causes an increase in crack growth during baseline cycles, which leads to acceleration factors. It is presumed that an underload induces a combination of tensile residual stress and strain hardening that increase crack growth during subsequent baseline cycles.

In the second study, the aim is to measure the fatigue threshold of small cycles (baseline cycles) and to verify its reduction due to large cycles (periodic underloads) are called periodic underloads.. Given that these tests in this region are time-consuming, fatigue tests were only conducted on steels with the lowest and highest acceleration factors in the first study; thus, the 415 and 304L steels, respectively.

The ratio of the number of baseline cycles over number of periodic underloads is defined as  $n$ . Two load procedures were conducted to investigate the effect of underloads on the baseline cycles. A first load procedure was conducted with decreasing  $\Delta K$  to measure a conventional fatigue threshold,  $\Delta K_{th,conv}$ , at a crack growth rate of  $2 \times 10^{-7}$  mm/cycle under constant amplitude loading and under periodic underloads at different  $n$  ratios. Then a second load procedure was conducted with increasing  $\Delta K_{BL}$  from zero to measured  $\Delta K_{th,true}$  at a crack growth rate of  $6.7 \times 10^{-9}$  mm/cycle and  $\Delta K_{th,conv}$  under periodic underloads at  $n = 1.25 \times 10^3$ .

The fatigue threshold of small cycles does not decrease for  $n > 1.25 \times 10^5$ . In turbine runners, the number of small cycles during 70 years of design life (about  $7 \times 10^{10}$ ). In order to avoid a decrease in the fatigue threshold, the number of large cycles (periodic underloads) should be kept below  $5.6 \times 10^5$ . The fatigue threshold of small cycles starts to decrease for  $n < 1.25 \times 10^5$ . This decrease is lower for the 415 steel as compared to 304L. The decrease in fatigue threshold due to periodic underloads is about five times higher when it is measured at  $6.7 \times 10^{-9}$  mm/cycle.

Tensile residual stress is induced in turbine runners during the fabrication and welding procedure. This stress increases the tensile static stress in runners, which leads to an increase in the  $K_{max}$  at the defect tip. As a result, the effect of an increase in the  $K_{max}$  on crack growth under constant and periodic underloads was also investigated. It is revealed that an increase in the  $K_{max}$  slightly decreases the fatigue threshold under constant and under periodic underloads.

## TABLE OF CONTENTS

DEDICATION .....	iii
ACKNOWLEDGEMENTS .....	iv
RÉSUMÉ.....	v
ABSTRACT .....	viii
TABLE OF CONTENTS .....	x
LIST OF TABLES .....	xiii
LIST OF FIGURES.....	xiv
LIST OF SYMBOLS AND ABBREVIATIONS.....	xviii
CHAPTER 1 INTRODUCTION .....	1
1.1 Context.....	1
1.2 Problematics .....	3
1.3 Research objectives .....	4
1.4 Outline of the thesis.....	5
CHAPTER 2 LITERATURE REVIEW .....	6
2.1 Brief historical review .....	6
2.2 Approaches in structural fatigue design .....	6
2.2.1 Total life approach .....	6
2.2.2 Defect tolerant approach.....	7
2.3 Fatigue life.....	7
2.3.1 Crack nucleation .....	8
2.3.2 Short crack growth.....	9
2.3.3 Long crack growth .....	9
2.4. Crack growth under constant amplitude loading.....	12
2.4.1 Crack growth regions.....	12
2.4.2 Crack closure .....	15
2.4.3 Crack growth prediction methods.....	23
2.5 Crack growth under variable amplitude loading .....	25
2.5.1 Basics and definitions .....	25
2.5.2 Effects of overloads and underloads in crack growth regions .....	26
2.5.3 Crack growth prediction methods.....	31
2.6 Conclusion of the literature .....	36

CHAPTER 3 METHODOLOGY AND EXPERIMENTAL PROCEDURE .....	38
3.1 Methodology.....	38
3.1.1 Stress spectra in turbine runners .....	38
3.1.2 Stress spectra simplifications .....	41
3.2 Experimental procedure.....	44
3.2.1 Material characterization .....	44
3.2.2 Tensile testing .....	45
3.2.3 Fatigue testing.....	45
CHAPTER 4 ORGANIZATION OF THE FOLLOWING SECTIONS .....	49
CHAPTER 5 CRACK GROWTH UNDER CONSTANT AMPLITUDE LOADING .....	51
5.1 ASTM load procedure .....	51
5.2 Materials and experimental procedures .....	51
5.2.1 Materials .....	51
5.2.2 Fatigue testing.....	51
5.3 Results .....	52
5.4 Discussion.....	54
5.4.1 Plastic zone size and phase transformation.....	54
5.4.2 Crack path irregularities.....	56
CHAPTER 6 ARTICLE 1: EFFECT OF PERIODIC UNDERLOADS ON FATIGUE CRACK GROWTH IN THREE STEELS USED IN HYDRAULIC TURBINE RUNNERS .....	58
6.1 Introduction .....	61
6.2 Materials .....	64
6.2.1 Chemical compositions and heat treatments.....	64
6.2.2 Microstructural characterization and tensile properties .....	65
6.3 Experimental procedures .....	67
6.3.1 Loading parameters.....	67
6.3.2 Fatigue testing.....	68
6.4 Results .....	70
6.4.1 Constant amplitude loading .....	70
6.4.2 Periodic underloads.....	74
6.5 Discussion.....	78
6.6 Conclusions .....	80

CHAPTER 7 ARTICLE 2: FATIGUE THRESHOLD AT HIGH STRESS RATIO UNDER PERIODIC UNDERLOADS IN TURBINE RUNNER STEELS .....	82
7.1 Introduction .....	84
7.2 Materials and experimental procedure .....	89
7.2.1 Materials .....	89
7.2.2 Fatigue testing.....	90
7.3 Results and discussion.....	94
7.3.1 First load procedure .....	94
7.3.2 Second load procedure.....	98
7.4 Conclusions .....	100
CHAPTER 8 GENERAL DISCUSSION .....	102
8.1 Crack growth under constant amplitude loading.....	102
8.2 Crack growth under periodic underloads.....	105
CHAPTER 9 CONCLUSION AND RECOMMENDATIONS.....	112
9.1 Conclusions .....	112
9.2 Further recommendations .....	113
REFERENCES.....	115

## LIST OF TABLES

Table 6.1 Typical load pattern for a Francis turbine runner [1].....	61
Table 6.2 Chemical compositions of studied materials (wt. %).....	64
Table 6.3 Average prior austenite grain size on the three orthogonal planes of each steel ( $\mu\text{m}$ ) ..	66
Table 6.4 Tensile properties of the three wrought steels in L and T directions at room temperature .....	67
Table 6.5 Maximum SIF at the tip of initial defects corresponding to runner lifetimes of 20 and 70 years .....	68
Table 6.6 Loading parameters for POV and SS sequences.....	68
Table 6.7 Parameters of Walker equation for each steel.....	73
Table 6.8 Maximum acceleration factors for the three steels at both $K_{\text{max}}$ and $n$ .....	75
Table 6.9 Comparison of measured crack growth with different prediction methods for the three steels (acceleration factors are calculated at $K_{\text{max},70}$ , $\Psi = 0.33$ and $n = 10$ ) .....	77
Table 8.1 Comparison of tensile properties in the old and new A516 steel with ASTM A516...106	106
Table 8.2 Comparison of acceleration factors in the old and new A516 steels at $n = 3$ and 10 at $K_{\text{max}} = 19.44 \text{ MPa}\cdot\text{m}^{1/2}$ .....	107

## LIST OF FIGURES

Figure 1.1 Hydraulic Francis turbine and runner components.....	1
Figure 2.1 Different periods of fatigue life [14].....	7
Figure 2.2 Slips bands under a) monotonous load, and b) cyclic load [11].....	8
Figure 2.3 Stress intensity factor at the tip of a sharp crack in an infinite plane [14].....	10
Figure 2.4 a) Three load modes of fatigue crack in a specimen, and b) monotonous plastic zones for each load mode under plane stress and plane stress using the Von Mises yield criterion [21].....	11
Figure 2.5 Crack growth rates versus $\Delta K$ in three different regions (adapted from [34]) .....	13
Figure 2.6 Two different procedures to measure the fatigue threshold, a) constant R ratio (ASTM standard), b) constant $K_{max}$ [32, 37].....	15
Figure 2.7 Crack growth rates versus $\Delta K_{eff}$ in the three different crack propagation regions [25, 31] .....	16
Figure 2.8 a) Variation in plastic zone throughout the thickness, and b) variations in $K_{cl}$ at three different $\Delta K$ due to a decrease in thickness in an 7075-T6 aluminum alloy specimen [21, 49]....	17
Figure 2.9 a) Surface asperities in the crack wake in an 2090-T8E41 aluminum lithium alloy, b) variations in $K_{cl}$ at three different $\Delta K$ due to removal of the crack wake asperities in an 7075-T6 aluminum alloy specimen [21, 49].....	18
Figure 2.10 Schematic illustration of a zigzag crack path to estimate the $K_{cl}$ [59, 60].....	18
Figure 2.11 Crack closure mechanisms at different crack growth regions at $R = 0.05$ [29].....	20
Figure 2.12 Schematic of load and crack opening displacement measured from crack mouth clip gauges behind the crack tip .....	21
Figure 2.13 Test procedures to determine the SIF corresponding to the crack propagation, a) at low R ratios, b) at high R ratios [93-94] .....	22
Figure 2.14 Crack growth after an applied overload, a) crack growth rate as a function of crack length, b) crack length as a function of number of cycles [108].....	27
Figure 2.15 Crack growth rates as a function of crack length after an applied overload and compressive underloads in austenitic stainless steel 316L [118].....	28

Figure 2.16 Schematic of crack closure variation after an applied overload and underload at different crack growth regions (adapted from [123]).....	29
Figure 2.17 Two prediction models, a) Wheeler, and b) Willenborg (adapted from [144]).....	33
Figure 2.18 Prediction of the crack growth rate following a single overload [148] .....	35
Figure 2.19 Example of CORPUS crack closure model in a simplified spectrum [151].....	36
Figure 3.1 a) Different regions of a runner blade based on stress magnitude [154], and b) steel plate filled with epoxy and silicone to protect strain gauges installed on region A of a runner blade [4].....	38
Figure 3.2 Typical stress spectrum imposed on turbine runners with small cycles superimposed to the highest tensile static stress, a) small cycles with low stress amplitudes, and b) small cycles with high stress amplitudes (adapted from [155, 156]).....	39
Figure 3.3 a) Linear damage summation employed to predict initial defect dimensions that will not cause rupture for 70 years, b) initial allowable semi-elliptical defect dimensions in different regions of a blade runner .....	40
Figure 3.4 Simplified load spectrum with POVs and SS sequences.....	42
Figure 3.5 Simplified load spectrum with small cycles and SS sequences.....	43
Figure 3.6 Compact tension specimen installed in an Instron servo-hydraulic machine .....	46
Figure 5.1 Crack growth rates versus $\Delta K$ and $\Delta K_{\text{eff}}$ at $R = 0.1$ in the 415 and 304L steels.....	53
Figure 5.2 Comparison of crack growth rates at $R = 0.1$ and $0.7$ in the 415 steel .....	54
Figure 5.3 Comparison of crack growth rates at $R = 0.1$ and $0.7$ in the 304L steel.....	54
Figure 5.4 Microstructure of the 304L in the LS orientation, a) as received, b) close to the necking of the tensile specimen (L direction) .....	55
Figure 5.5 Crack path on the surface of the specimen at $\Delta K_{\text{th,conv}}$ in the 415 steel at, a) $R = 0.1$ , and b) $R = 0.7$ .....	56
Figure 5.6 Crack path on the surface of the specimen at $\Delta K_{\text{th,conv}}$ in the 304L steel at, a) $R = 0.1$ , and b) $R = 0.7$ .....	56
Figure 6. 1 Different load cycles under variable amplitude loading.....	62
Figure 6.2 Microstructure of the three wrought steels, a) 415, b) A516, and c) 304L.....	66

Figure 6.3 Applied loading sequence on the three steels at constant $K_{max}$ , .....	69
Figure 6.4 Schematic of crack deflection angle ( $\theta$ ) and crack deflection length ( $l$ ) .....	70
Figure 6.5 Crack path deflection under constant amplitude loading at $K_{max,70}$ and $R = 0.1$ in the a) 415 steel, b) A516 steel, and c) 304L steel (crack propagates from left to right in the three cases) .....	71
Figure 6.6 Crack growth rates versus load ratio and corresponding Walker predictions at $K_{max,70}$ .....	72
Figure 6.7 Crack growth rates versus load ratio and corresponding Walker predictions at $K_{max,20}$ .....	72
Figure 6.8 Fatigue striations on fatigue surfaces under constant amplitude loading at $K_{max,20}$ , (a) 415 steel at $R = 0.1$ , (b) A516 steel at $R = 0.1$ , (c) 304L steel at $R = 0.1$ , and (d) 304L steel at $R = 0.7$ (crack propagates from left to right in all cases).....	74
Figure 6.9 Acceleration factors for the three steels at $K_{max,70}$ and $n = 10$ (curves are obtained from a third order polynomial regression of the data) .....	76
Figure 6.10 Acceleration factors for the three steels at $K_{max,20}$ and $n = 10$ (curves are obtained from a third order polynomial regression of the data) .....	76
Figure 6.11 Striations on fatigue surfaces in the 304L steel at $K_{max,20}$ under periodic underloads ( $R_{BL} = 0.7$ , $R_{UL} = 0.1$ and $n = 10$ ). Figure 5.11 (b) is an enlargement of Figure 5.11 (a) (the crack propagates from left to right in all cases).....	79
Figure 7.1 Two different load procedures to measure the fatigue threshold at high R ratio, (a) constant R ratio (ASTM standard), (b) constant $K_{max}$ [37].....	86
Figure 7.2 Step-by-step decreasing $K_{max}$ load procedure to measure the fatigue threshold at constant high R ratio under PUL (adapted from [128]) .....	87
Figure 7.3 Effect of $n$ ratio on the fatigue threshold at high R ratio of an 2024-T351 aluminum alloy under periodic underloads (PUL) and periodic compressive underloads (PCUL) (adapted from [128]) .....	88
Figure 7.4 Constant $K_{max}$ procedure to measure the fatigue threshold at high R ratio under PUL (adapted from [132]) .....	88
Figure 7.5 $K_{max}$ effect on the fatigue threshold under CAL and PUL (adapted from [132]) .....	89

Figure 7.6 Microstructure of the two wrought steels: (a) 415 steel, and (b) 304L steel .....	90
Figure 7.7 Load sequences in the first load procedure with decreasing $\Delta K$ under CAL and PUL at a given $n$ ratio .....	92
Figure 7.8 Expected results of load procedure in Figure 7.7 in a $da/dN - \Delta K_{BL}$ plot.....	92
Figure 7.9 Load sequences in the second load procedure with increasing $\Delta K_{BL}$ under PUL ( $n = 10^3$ ) .....	94
Figure 7.10 Expected results of load procedure in Figure 7.9 in a $da/dN - \Delta K_{BL}$ plot.....	94
Figure 7.11 Log-linear plot of crack growth rates versus SIF range of baseline cycles under CAL and PUL at different $n$ ratios in the 415 steel.....	96
Figure 7.12 Log-linear plot of crack growth rates versus SIF range of baseline cycles under CAL and PUL at different $n$ ratios in the 304L steel .....	96
Figure 7.13 Decrease in $\Delta K_{th,conv}$ due to periodic underloads in both steels.....	97
Figure 7.14 Effect of periodic underloads at $n = 10^3$ on $\Delta K_{th,conv}$ and $\Delta K_{th,true}$ of the 415 steel in a log-linear $da/dN - \Delta K_{BL}$ plot .....	99
Figure 7.15 Effect of periodic underloads at $n = 10^3$ on $\Delta K_{th,conv}$ and $\Delta K_{th,true}$ of the 304L steel in a log-linear $da/dN - \Delta K_{BL}$ plot.....	99
Figure 8.1 Effect of $K_{max}$ on crack growth rates at high R ratios in the 415 steel.....	104
Figure 8.2 Effect of $K_{max}$ on crack growth rates at high R ratios in the 304L steel .....	105
Figure 8.3 Log-linear of $da/dN$ versus $\Delta K_{BL}$ curve under CAL and PUL in the 415 and the 304L steels at $n = 10^2$ .....	109
Figure 8.4 Crack growth rates versus linear $\Delta K_{BL}$ from different test procedures under CAL and PUL in 415 steel.....	111
Figure 8.5 Crack growth rates versus linear $\Delta K_{BL}$ from different test procedures under CAL and PUL in 304L steel .....	111
Figure 9.1 Startup and SNL in an operating turbine runner with a repeated sequence.....	113
Figure 9.2 Stress spectrum with three stress cycles imposed at the defect tip .....	114

## LIST OF SYMBOLS AND ABBREVIATIONS

### Latin symbols

$a$ and $c$	length and width of semi-elliptical defect
$a_{20}$	maximum initial crack length allowed for 20 years design life
$a_{70}$	maximum initial crack length allowed for 70 years design life
$b$ and $t$	runner blade length and thickness
$b'$	Basquin equation exponent
$c'$	Coffin-Manson equation exponent
$C_{R0}$ and $p$	Walker equation parameters
$F$ and $Q$	geometric functions for calculating stress intensity factor
$H$	strength coefficient
$K_{\max,OL}$	maximum stress intensity factor of an overload
$K_t$	stress concentration factor
$K_{\max,th}$	maximum stress intensity factor range at the fatigue threshold
$K_{\max,1}$	maximum stress intensity factor of $11.11 \text{ MPa}\cdot\text{m}^{1/2}$
$K_{\max,2}$	maximum stress intensity factor of $19.43 \text{ MPa}\cdot\text{m}^{1/2}$
$l$	crack length deflection
$m$	Paris equation exponent
$n$	frequency of baseline cycles over underload cycles, $\Delta N_{BL}/\Delta N_{UL}$
$q$	number of underload cycles in one block
$R$	stress ratio
$R_{BL}$	load ratio of baseline cycles
$R_{UL}$	load ratio of underload cycles
$r_{y,OL}$	monotonous plastic zone size created by an overload
$r_y$	monotonous plastic zone size

$r_{yc}$	cyclic plastic zone size
$r_{yc}'$	cyclic plastic zone size of an underload cycle
$s$	strain hardening exponent
$W$	compact tension specimen width

### Greek symbols

$\Delta a_{\text{block}}$	crack growth in one load block
$\Delta K$	stress intensity factor range
$\Delta K_{\text{eff}}$	effective SIF range
$\Delta K_{\text{BL}}$	stress intensity factor range of baseline cycles
$\Delta K_{\text{th}}$	stress intensity factor range at the fatigue threshold
$\Delta K_{\text{th,eff}}$	effective stress intensity factor range at the fatigue threshold
$\Delta K_{\text{th,conv}}$	conventional fatigue threshold ( $2 \times 10^{-7}$ mm/cycle)
$\Delta K_{\text{th,true}}$	true fatigue threshold ( $6.7 \times 10^{-9}$ mm/cycle)
$\Delta K_{\text{th,CAL}}$	true fatigue threshold under constant amplitude loading
$\Delta K_{\text{UL}}$	stress intensity factor range of an underload
$\Delta N_{\text{BL}}$	number of baseline cycles in one load block
$\Delta N_{\text{UL}}$	number of underload cycles in one load block
$\delta_{\text{UL}}$	underload cycle striation width
$\delta_{\text{BL}}$	baseline cycle striation width
$\varepsilon$	true strain
$\varepsilon_e$	elastic strain
$\varepsilon_f$	true strain at fracture
$\varepsilon_p$	plastic strain
$\varepsilon_r$	relative elongation at rupture
$\theta$	crack deflection angle

$\sigma$	true stress
$\sigma_{ij}$	stress components
$\sigma_f$	true stress at fracture
$\phi$	angle of a specific point at the front of a semi-elliptical defect
$\Psi$	ratio of stress intensity factor ranges, $\Delta K_{BL}/\Delta K_{UL}$

### Abbreviations

BL	baseline cycles
CAL	constant amplitude loading
CT	compact tension specimen
COD	crack opening displacement
L	longitudinal (rolling) direction of the plate
LT	long transverse orientation
LS	long-short transverse orientation
LDS	linear damage summation
OL	single overload
POV	power output variations
PUL	periodic underloads
S	short-transverse direction of the plate
SS	start/stop sequences
SIF	stress intensity factor
T	transverse direction of the plate
TS	transverse-short transverse orientation
UL	single underload

## CHAPTER 1 INTRODUCTION

### 1.1 Context

Hydraulic turbines are the main sources of electricity generation from hydro energy. This energy is renewable, non-polluting, and more efficient than the one generated by fossil fuels [1]. A hydraulic Francis turbine and its components are shown in Figure 1.1. In this type of turbine, water enters a spiral casing in a radial direction with respect to a shaft. It is then directed inside a runner by the circumferential wicket gates [1]. It hits the runner blades successively and leaves a torque on the runner. This torque induces a spin in the runner, which is coupled to a rotor by the shaft. When the rotor spins inside the magnetic field of a stator, electricity is generated.

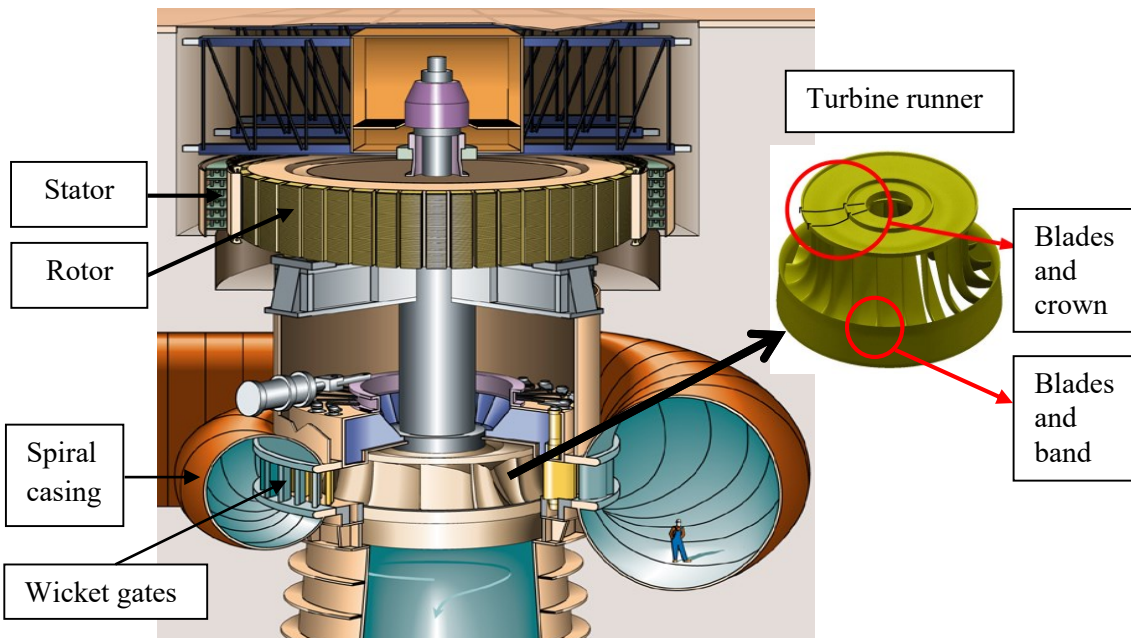


Figure 1.1 Hydraulic Francis turbine and runner components

The water flow creates a tensile static stress on the blade. This stress leaves a torque that induces a spin in the runner with respect to the shaft. As the blade moves forward, the induced stress gradually decreases; however, the subsequent wicket gate directs the water to hit the blade and re-increase the stress to its maximum. So the blade continues to move forward [2]. These repeated sequences, known as wicket gates and blade interactions, and other hydraulic phenomena create stress fluctuations on the blade which vary from maximum to minimum values [3]. These small pressure

fluctuations create cycles with small stress amplitudes that are superimposed to the tensile static stress.

During an initial period, where the runner is not coupled to the rotor, the wicket gates are partially opened and direct the water flow to spin the runner. This flow generates an initial startup and spin-no-load in the stress spectrum. Subsequently, to generate electricity, the runner becomes coupled to the rotor and the wicket gates become completely open. As a result, the tensile static stress increases to a maximum level.

During the runner operation, electricity demands vary and cause variations in the electricity production known as power output variations. These variations are adjusted by pivoting the wicket gates that control the water flow. By completely closing the wicket gates, the static stress induced on the runner blades is reduced to zero, so that the runner stops spinning. These start/stop sequences are repeated throughout the design life of the runner. In some cases, a sudden uncoupling between the rotor and runner may occur [4]. As a result, the runner does not transfer the torque to the rotor. This causes the runner to spin at a higher speed (overspeed) till the wicket gates stop the water flowing into the runner. This is known as load rejection or overspeed [4, 5]. The aforementioned changes in the operating conditions create cycles with large stress amplitude, which intercut the tensile static stress.

As a summary, on one hand, interaction between the wicket gates and blade plus other hydraulic phenomena creates small stress amplitude cycles in the runner. On the other hand, power output variations, start/stop sequences, and load rejections create large stress amplitude cycles in the runner. Therefore, the runner is subjected to small stress amplitude cycles that are superimposed to tensile static stress, which is intercut with large stress amplitude cycles in the stress spectrum. For convenience, we refer to the aforementioned stress cycles as small and large cycles, hereafter.

## 1.2 Problematics

Runners are mostly fabricated from cast steels. A martensitic stainless steel, ASTM CA6NM, has recently been used to fabricate the turbine runners. The ASTM A36, a ferritic-pearlitic cast steel, was used to fabricate many runners which are installed in Hydro-Quebec power stations. Some other runners are fabricated from the ASTM CF8, a cast austenitic stainless steel. Runners may also be fabricated using the wrought version of the aforementioned steels, which are the AISI 415, ASTM 516, and 304L steels, respectively. In this study, the wrought steels are chosen in order to have less dispersion in the results.

Defects are formed during the fabrication process (i.e. casting and welding) or the operation (i.e. cavitation) of runners. Defects or cracks in high stress regions of the blade propagate due to small cycles superimposed to a tensile static stress intercut with large cycles.

In some power stations with recently built runners, the stress amplitude of small cycles is low (few MPa) and induces a  $\Delta K$  that is below the crack propagation threshold. As a result, they do not induce crack growths and can be neglected; however, large cycles generated by operating conditions can grow the defects in the runner and can lead to its failure within 70 years of design life.

In the engineering approach, linear damage summation (LDS) is employed to predict defect growth due to large stress amplitude cycles. Thus, using the LDS prediction method, during the operation runners are periodically stopped to inspect and verify defect growth as compared to the one predicted by LDS; however, stopping runners for an inspection decreases energy production, which is a costly procedure. Thus, there is a tendency to rely on crack growth predicted by LDS and minimize inspections or carry them out when it is necessary.

In reality, however, interaction between large cycles can increase defect growth in runners. Consequently, defects will grow faster than the one predicted by LDS and may lead to the failure of the runners before a scheduled inspection. As a result, there is a need for a precise crack growth prediction that will enable designers to minimize the frequency of inspections.

In some power stations with aged runners, the stress amplitude of small cycles is high (tens of MPa) and induces a  $\Delta K$  that is close to the fatigue threshold. The hydraulic phenomena generate a large number of small cycles during the life design of the runners. Therefore, the  $\Delta K$  at the defect tips will be below the fatigue threshold. Otherwise, small cycles will propagate the defects, which

lead to an early failure of runners. Large cycles can further decrease the fatigue threshold of small cycles and lead to the propagation of defects. Thus, the fatigue threshold of small cycles and the one intercut with large should be measured.

Tensile residual stresses are induced in the runners during the fabrication and welding process. As the crack propagates in the runner it can be subjected to these tensile residual stresses, which will increase the tensile static stress at the defect tip. Higher tensile static stress may decrease the fatigue threshold of small cycles. Moreover, higher tensile static stress may decrease the fatigue threshold of small cycles intercut with periodic underloads.

### **1.3 Research objectives**

In a first study, small cycles induce a  $\Delta K$  that is below the fatigue threshold. So they do not cause crack propagation. Thus, the cycles are neglected in the load spectrum and the effect of large cycles on crack growth is investigated. Crack growths measured under large cycles will be compared to the ones predicted using linear damage summation.

In a second study, small cycles induce a  $\Delta K$  that is close to the fatigue threshold. So the crack can grow and may lead to runner's premature failure. Thus, the fatigue threshold of small cycles will be measured. Moreover, large cycles can decrease the fatigue threshold of small cycles. Thus, the decrease in the fatigue threshold of small cycles due to large cycles will be defined.

A higher tensile static stress may induce a decrease in the fatigue threshold of small cycles and the ones intercut with large cycles. Therefore, the decrease in both fatigue thresholds due to higher tensile static stress will be defined.

#### **Specific objectives**

Crack growth under constant amplitude loading in the three different steels at different R ratios will be investigated. Factors that may affect crack growth at different R ratios will also be investigated.

Different load procedures proposed in literature will be studied, and a procedure leading to better estimation of load interaction between load cycles and more accurate measurement of  $\Delta K_{th}$  will be conducted. Fatigue testing with two different amplitude cycles (small and large) in a load spectrum will be developed and implemented.

Accuracy of LDS prediction is verified for each steel, and factors leading to an increase in crack growth due to small and large cycles will be analyzed. The effect of large cycles on the fatigue threshold of small cycles measured with low and very low crack growth rate will be investigated.

## **1.4 Outline of the thesis**

The second chapter is a literature review on fatigue. The fatigue initiation that may lead to propagation is shortly summarized. A review of different studies on fatigue crack propagation under constant amplitude loading and variable amplitude loading is then presented. Finally, factors influencing crack propagation and the suggested prediction methods are presented.

The third chapter explains the methodology that was chosen to carry out the studies and conduct fatigue tests. The microstructural characterization and tensile test are then explained in detail.

The fourth chapter, explains about the following chapter and the organization of the whole

The fifth chapter presents the fatigue tests conducted under constant amplitude loading. The results of this chapter are employed in chapter 6.

The sixth chapter presents the fatigue tests conducted according to the first study and the corresponding results. This chapter is presented as a published article.

The seventh chapter presents the fatigue tests conducted according to the second study and the corresponding results. This chapter is presented as a published article.

The eighth chapter is a general discussion on the studies conducted in the previous chapters. Crack growth rates under constant amplitude loading and periodic underloads are discussed.

The final chapter covers the main conclusion and proposes to study a real and non-simplified stress spectrum in runners.

## CHAPTER 2 LITERATURE REVIEW

### 2.1 Brief historical review

During the first industrial revolution, most structures were made of steels that could be loaded under a high tensile load [6]. Steels were widely used in the railroad industry. In the design, stress applied on steels was limited to monotonous yield stress while taking into account a safety factor; however, regular failures were reported on railroad axles made of steels [7]. These failures implied that cyclic stresses below the yield stress can induce local deformation in the railroad axles leading to their failure. This was a first incident implying the importance of considering cyclic stresses and loads in design.

During the Second World War, failure occurred in a large number of ships that were made of steels and whose hulls were welded. In 2003, in Quebec, at the Sainte-Marguerite 3 power station, many defects grew during the operation of the Francis turbine runners, which were made of steels. This problem caused a huge reduction in the production of electricity [8]. Thus, different incidents such as those mentioned above have implied that more investigations should be conducted on the effect of the cyclic stresses on steels in order to improve their design in structures.

The term fatigue is defined as “ the process of progressive localized permanent structural change occurring in a material subjected to conditions which produce fluctuating stresses and strains at some points and which may culminate in cracks or complete fracture after a sufficient number of fluctuations [9].” Two major approaches in structural fatigue design employed to conduct fatigue tests in materials will be presented.

### 2.2 Approaches in structural fatigue design

#### 2.2.1 Total life approach

In the total life approach, a laboratory specimen is usually subjected to a cyclic nominal stress amplitude ( $\Delta S$ ) or cyclic local strain amplitude ( $\Delta \epsilon$ ) until it fails [10]. Different levels of cyclic stress or strain are applied as a function of the number of cycles until the failure occurs, which are known as the  $\Delta S$ -N or  $\Delta \epsilon$ -N curves. High amplitude of the stress or strain will result in failure with a low number of cycles, or low cycle fatigue. Otherwise, this is known as high cycle fatigue [11].

A real structure can be designed based on the aforementioned curves for a high or low number of cycles; however, a small defect free laboratory specimen subjected to  $\Delta S$  under stress will endure more cycles as compared to the real structure with defects [12]. Thus, in this case, the estimated fatigue life will be longer and the design approach is non-conservative; however, as the specimen becomes similar to the real structure, the design becomes realistic.

### 2.2.2 Defect tolerant approach

In this approach, a structure is considered to have defects. So, an initial crack length, which represents the defect, is generated in the laboratory specimen under nominal stress or strain [13]. The crack growth rates in materials are measured in the specimen. Then using the measured crack growth rates and Fracture Mechanics concepts, the initial defect dimensions that will not lead to the structure's failure during their design life is estimated.

## 2.3 Fatigue life

Figure 2.1 shows the different periods of fatigue life for any structure subjected to fluctuating stresses and strains. The fatigue life is divided into a nucleation period followed by a crack growth period until reaching the final failure. After the crack nucleation, a microcrack or short crack starts to grow. The local stress and strain distributions in front of the crack tip may arrest the growth of the short crack. Otherwise, it grows and becomes a macrocrack or long crack. This long crack may propagate until the final failure.

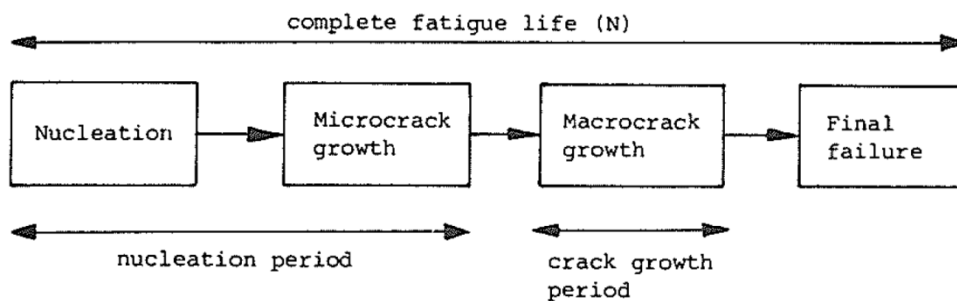


Figure 2.1 Different periods of fatigue life [14]

### 2.3.1 Crack nucleation

In crystalline materials such as steels, there are inherent defects in crystals called dislocations. Plastic deformation results from the dislocation movements in high atomic density planes, called slip planes [11]. When a steel specimen is monotonically loaded, local slip bands resembling to a staircase are formed on the specimen surface, as shown in Figure 2.2a [11]. When a specimen is loaded cyclically, the density of slip lines or bands increases and accumulates on the surface. These slip bands create some intrusions and extrusions on the surface as shown in Figure 2.2b. This leads to the crack nucleation after a certain number of cycles.

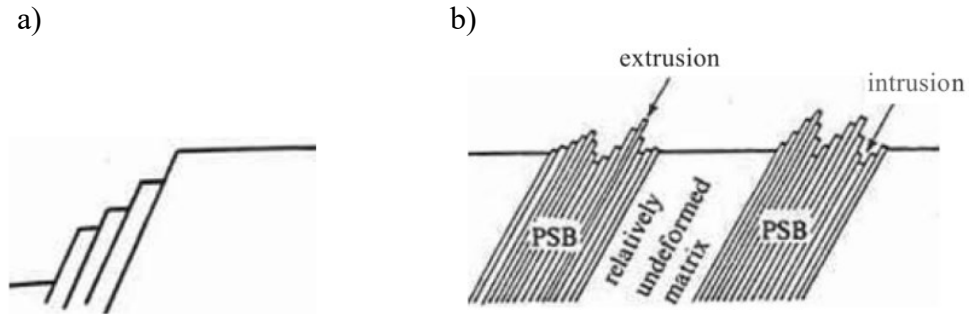


Figure 2.2 Slips bands under a) monotonous load, and b) cyclic load [11]

The relation between the nominal stress amplitude ( $\Delta S$ ) and number of cycles ( $N$ ) to failure is given by the Basquin equation:

$$\Delta S = \sigma'_f (N)^{b'} \quad (2.1)$$

where  $\sigma'_f$  is approximately equal to the true stress at fracture,  $\sigma_f$ , and  $b'$  is a fitting exponent. The relation between the local strain amplitude ( $\Delta \varepsilon$ ) and number of cycles to failure is given by the Coffin-Manson equation:

$$\Delta \varepsilon = \frac{\sigma'_f}{E} (N)^{b'} + \varepsilon'_f (N)^{c'} \quad (2.2)$$

where  $E$  is Young's Modulus,  $\varepsilon'_f$  is approximately equal to the true strain at fracture,  $\varepsilon_f$ , and  $c'$  is a fitting exponent. Both correlations were found for uniaxial stress or strain at an R ratio (minimum load over the maximum one) equal to -1. Other studies proposed a correlation between the stress or strain at different R ratios with the number of cycles to failure [15]. In the case where nucleation

does not occur for a specified high number of cycles (e.g.  $10^7$  cycles), it is assumed that the fatigue limit is reached and the specimen will not fail [16].

It was, however, observed that the specimen fails at a stress below the fatigue limit with a number of cycles that is higher than  $10^7$  [17]. In this case, it is observed that nucleation occurs below the surface from an inclusion or void in the steel [17].

### 2.3.2 Short crack growth

After that crack nucleates, it is still small or short and may continue to grow [18]. The cracks is *microstructurally small* if its length is comparable to the length of the microstructure, for example, a crack smaller than the grain size [19]. It is *mechanically small* if its length is small as compared to the local plastic deformation, for example, a crack growing out of a notch [20]. It is *physically small* if its length is small, for example, a length typically between 0.1 and 1 mm. A short crack must overcome microstructural barriers and the local plastic strain at its tip to propagate and become a macro crack, and leading to complete failure.

### 2.3.3 Long crack growth

Once the crack has overcome microstructural barriers and the plastic deformation at its tip, it becomes physically long. At this stage, the crack grows in a continuum medium. As it grows, the crack tip plasticity becomes negligible as compared to the crack length and specimen geometry [16]. Thus, the specimen is considered to be nominally elastic and plasticity is only limited to the crack tip. These conditions are called small scale yielding [21].

#### a) Stress intensity factor

Stress intensity factor is a parameter that characterizes the elastic field in the vicinity of a sharp crack tip under small scale yielding conditions. Structures in the linear elastic continuum mechanics must satisfy equilibrium and compatibility equations. The Airy stress function ( $\phi$ ) satisfies both equations which are combined in one equation called the bi-harmonic [22].

A singular stress field is created in the vicinity of a sharp crack. A complex stress function was proposed to satisfy bi-harmonic equations for singular stress fields [21]. This function was first proposed for a sharp crack under a bi-axial stress in an infinite plate. However, it was modified later for a uni-axial tensile stress, which results to the definition of a stress intensity factor (K) [23], which is given by following equation:

$$K_I = S\sqrt{2\pi a}$$

where  $S$  is the nominal applied stress, and  $2a$  is the crack length in the infinite plate shown in Figure 2.3. Later a geometric function,  $Y$ , was used to define a corresponding  $K$  in a finite plate.

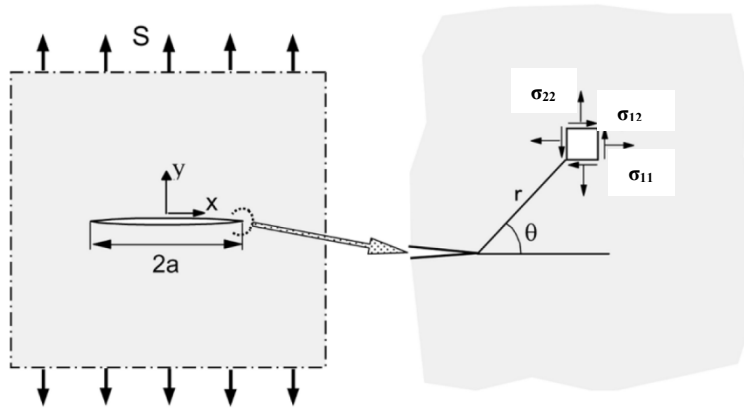


Figure 2.3 Stress intensity factor at the tip of a sharp crack in an infinite plane [14]

#### b) Load modes and plasticity

As shown in Figure 2.4a, crack may grow due to three different loads with respect to its plane. If the load opens the crack planes, it is called mode I. If it shears the crack planes, it is called mode II; and if it twists the tip of the crack plane, it is called mode III [24, 25].

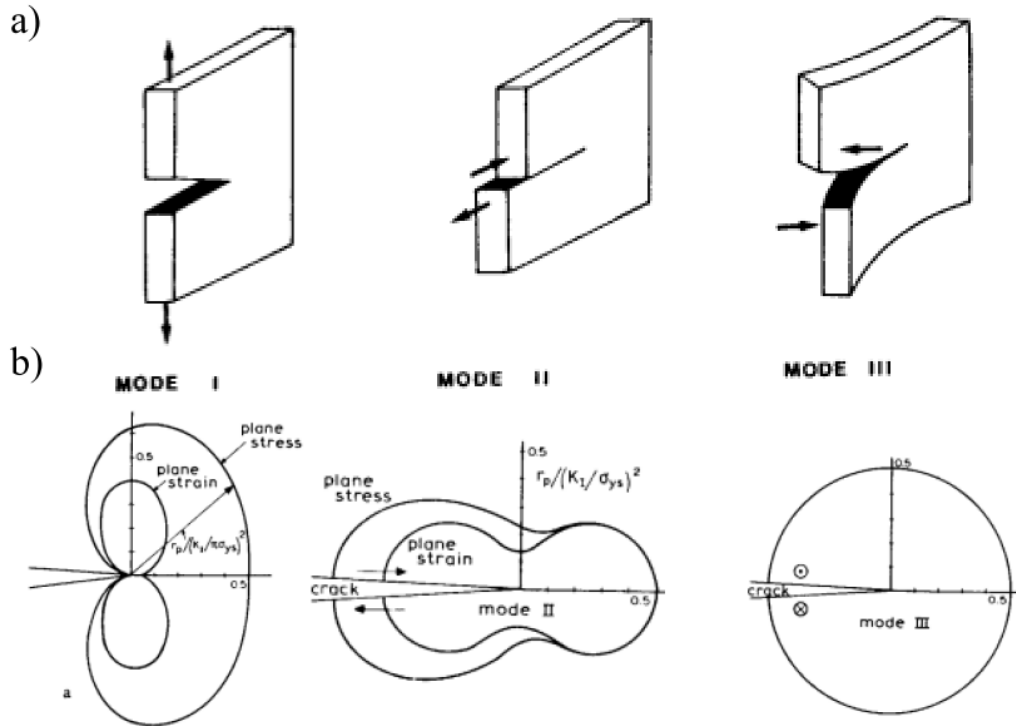


Figure 2.4 a) Three load modes of fatigue crack in a specimen, and b) monotonous plastic zones for each load mode under plane stress and plane stress using the Von Mises yield criterion [21]

Local stress components ( $\sigma_{ij}$ ) at a given distance ( $r$ ) and angle ( $\theta$ ) from the crack tip (see Figure 2.3) are correlated to  $K$  for all three load modes by the following equation.

$$\sigma_{ij} = \frac{K_I}{\sqrt{2\pi r}} f_{ij}(\theta) + \frac{K_{II}}{\sqrt{2\pi r}} g_{ij}(\theta) + \frac{K_{III}}{\sqrt{2\pi r}} h_{ij}(\theta) \quad (2.3)$$

The  $f_{ij}(\theta)$ ,  $g_{ij}(\theta)$ ,  $h_{ij}(\theta)$  are trigonometric functions [22]. The aforementioned equation terms can have a second higher order term [26], known as the T stress, but it is not considered here. Stress components close to the crack tip ( $r$  tends towards zero) increase towards infinity; however, plasticity at the crack tip limits stress components to the yield stress of the material. Three dimensional stress components are usually simplified into two dimensional ones, under a plane stress or plane strain state. Inserting stress components into the von Mises yield criterion gives an equivalent stress that is compared to the yield stress of the steel. The two dimensional stress components in Equation 2.3 are inserted into von Mises criterion to derive the boundary of the plastic zone size [21]. These boundaries for the three load modes are shown in Figure 2.4b. The size of the monotonous plastic boundary or zone,  $r_y$ , for Mode I and  $\theta = 0$ , can be written as:

$$r_y = \frac{I}{\alpha\pi} \left( \frac{K_{\max}}{\sigma_{ys}} \right)^2 \quad (2.4)$$

where  $K_{\max}$  is the maximum stress intensity factor (SIF),  $\sigma_{ys}$  is the yield stress of the steel, and the value of  $\alpha$  depends on the stress state at the crack tip. The value of  $\alpha$  is estimated by two different approaches for the plane stress state [27]. Both approaches results in roughly similar values, where  $\alpha$  is equal to 1 [21, 22]. The value of  $\alpha$  increases to 3 for the plane strain state due to stress triaxiality at the crack tip.

On the other hand, the size of the cyclic plastic zone,  $r_y$  is given as:

$$r_{yc} = \frac{I}{\beta\pi} \left( \frac{\Delta K}{\sigma_{yc}} \right)^2 \quad (2.5)$$

where  $\Delta K$  is the SIF range ( $K_{\max} - K_{\min}$ ),  $\sigma_{yc}$  is the cyclic yield stress of the steel, and the value of  $\beta$  depends on the cyclic stress at the crack tip. Some studies estimated that  $\beta$  is equal to  $4\alpha$  for a quasi-stationary crack. Thus, the cyclic plastic zone size is estimated to be roughly one-fourth of the monotonous one [28]; however, other studies suggested that the cyclic plastic zone may be one-fourth to one-tenth of the monotonous one for a growing crack [29, 30].

## 2.4. Crack growth under constant amplitude loading

### 2.4.1 Crack growth regions

Fatigue crack growth rates as a function of SIF range,  $\Delta K$ , in steels consists of three distinct regions, as shown in Figure 2.5 [31]. Most of the fatigue test procedures in literature were first conducted in the medium crack growth rates region, known as Paris [31]. Later, many tests were conducted in the low crack growth rates region, known as near-threshold. Thus, we first introduce the Paris region and then the near-threshold region.

#### a) Paris region

After a conventional pre-cracking, the initial  $\Delta K$  and  $K_{\max}$  are gradually increased at a constant R ratio to measure crack growth rates. The shape and the amount of the increasing gradient  $dK_{\max}/da$  do not affect crack growth rates [32]. A correlation between crack growth rates ( $da/dN$ ) and SIF range,  $\Delta K$ , was found in region II [33]. This correlation is given by the following equation;

$$\frac{da}{dN} = C(\Delta K)^m \quad \Delta K = K_{max} - K_{min} \quad (2.6)$$

which is known as the Paris equation and where  $c$  and  $m$  are the steel or material parameters. Crack growth rates versus  $\Delta K$  are measured using a laboratory specimen to obtain Paris equation parameters. In real structures,  $\Delta K$  is calculated by estimating a geometric factor ( $Y$ ), the applied load range and a typical crack length ( $a_0$ ) [21, 22]. Next, crack growth in each step ( $\Delta a_i$ ) is calculated at a given  $\Delta K$  using Paris equation parameters for a number of cycles. Finally, the total crack growth is incremented step-by-step to predict crack growth in the structure as shown in Equation 2.7.

$$\Delta a_i = C(\Delta K)^m \times \Delta N, \quad a_i = a_0 + \Delta a_i \quad (2.7)$$

Crack growth rates are high in Region III. Thus, a given crack length is reached with much fewer cycles as compared to the Paris region. Crack growth is quasi-static within this region, and when the maximum SIF reaches the critical SIF, catastrophic failure occurs.

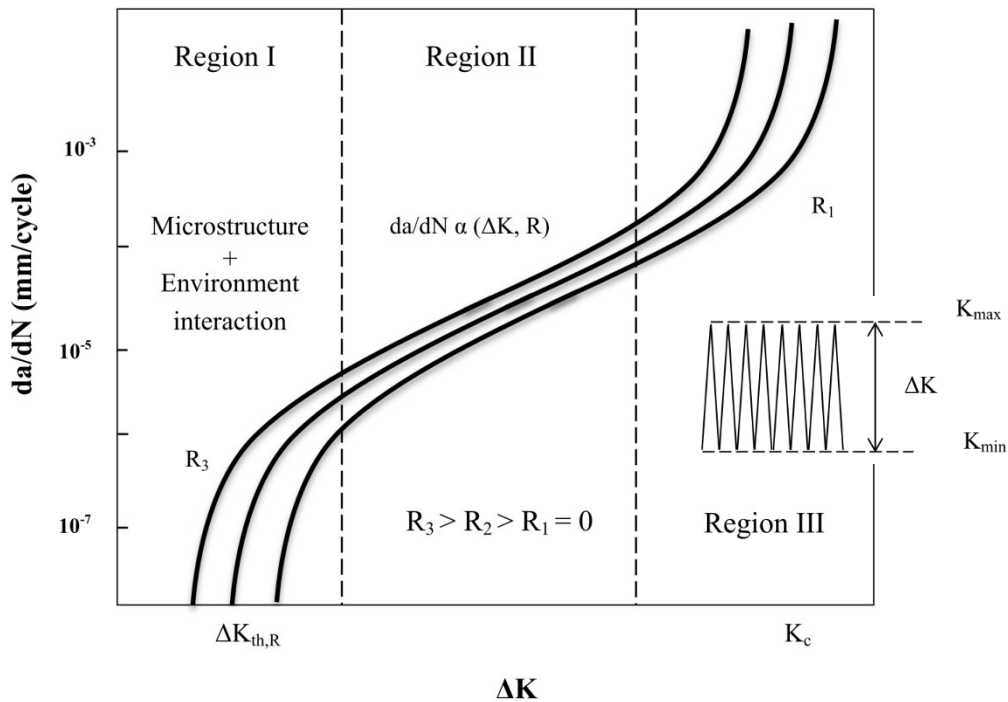


Figure 2.5 Crack growth rates versus  $\Delta K$  in three different regions (adapted from [34])

## b) Fatigue threshold region

After a conventional pre-cracking, the initial  $\Delta K$  and  $K_{\max}$  parameter should be decreased at a constant R ratio following a specific procedure to reach a  $\Delta K$  that will not induce crack growth, known as the fatigue threshold; however, a high decreasing gradient of the aforementioned parameter builds up a higher amount of plasticity and roughness in the crack wake, which can close the crack while reaching the fatigue threshold [25]. This can underestimate the crack growth rate at a given  $\Delta K$  in the near-threshold region and overestimate the fatigue threshold [32]. Consequently, different test procedures are proposed in literature to minimize extra crack closure, while reaching the fatigue threshold.

An early test procedure was conducted by keeping the maximum displacement constant as the crack length increases during the test; however, this procedure induces a constant and low decreasing gradient,  $dK_{\max}/da$ . Consequently, this test procedure is time consuming. Afterwards, it was proposed to decrease  $K_{\max}$  step-by-step but by imposing some limit conditions on the decrease in  $K_{\max}$  [32]. However, these conditions do not minimize the crack closure at the near-threshold region. Finally, a procedure known as the ASTM E647 was proposed to conduct a continuous decrease in the  $K_{\max}$  and limit the decreasing gradient of  $dK_{\max}/da$  in order for it not to be higher than  $0.08 \text{ mm}^{-1}$  (Figure 2.6).

That being said, even low  $dK_{\max}/da$  can induce extra crack closure [35]. Thus, in order to eliminate the consequences of  $dK_{\max}/da$ , some studies proposed a constant  $K_{\max}$  procedure where only  $\Delta K$  was decreased to reach  $\Delta K_{\text{th}}$  (Figure 2.6). This procedure minimizes extra crack closure induced in the crack wake [36]. The aforementioned test procedures are explained in detail in Chapter 7.

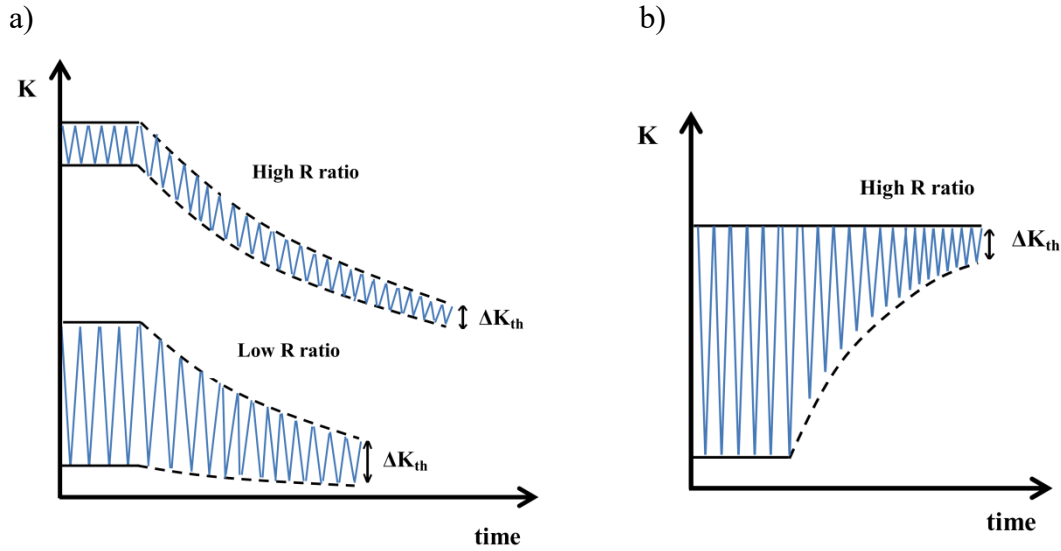


Figure 2.6 Two different procedures to measure the fatigue threshold, a) constant R ratio (ASTM standard), b) constant  $K_{max}$  [32, 37]

The near-threshold region is sensitive to the microstructure [21]. The beginning of this region corresponds to a crack growth rate that may vary from  $10^{-8}$  to  $10^{-7}$  mm/cycle, and the corresponding  $\Delta K$  is the so-called fatigue threshold ( $\Delta K_{th}$ ) [38]. The SIF at the crack tip below the  $\Delta K_{th}$  value is assumed to not cause any crack propagation [34]. The end of region I is estimated to be close to  $10^{-6}$  mm/cycle for steels, which is close to a lattice spacing per cycle [31, 39].

#### 2.4.2 Crack closure

As the R ratio increases, the crack growth rate versus  $\Delta K$  increases in the Paris region as shown in Figure 2.5. Crack growth rates further increase in the near threshold region and lead to a lower fatigue threshold,  $\Delta K_{th}$ , at a high R ratio as compared to a low R ratio [40-42].

It was reported that during the unloading, the crack may close at a SIF,  $K_{cl}$  above  $K_{min}$  at low R ratios. On the other hand, during the loading, the crack opens at a SIF,  $K_{op}$ , above  $K_{min}$ . The SIF at closure ( $K_{cl}$ ) and opening ( $K_{op}$ ) are close to each other [30]. It was concluded that crack grows only when the opening part of  $\Delta K$  is applied. Thus,  $K_{cl}$  is deducted from  $K_{max}$  to calculate the opening part of  $\Delta K$ , known as the effective SIF range,  $\Delta K_{eff}$ , and is given in Equation 2.8.

$$\Delta K_{eff} = K_{max} - K_{cl}(R, \Delta K) \quad , \quad K_{cl}(R, \Delta K) \geq K_{min} \quad (2.8)$$

At a given  $K_{max}$ , as R ratio increases,  $K_{min}$  increases until it becomes equal to or higher than  $K_{cl}$ . As a result,  $\Delta K_{eff}$  becomes equal to  $\Delta K$ . The estimated crack growth rate as a function of  $\Delta K_{eff}$  at different R ratios is given by the following equation,

$$\frac{da}{dN} = f(\Delta K_{eff}) = C(\Delta K_{eff})^m \quad (2.9)$$

results in similar crack growth rates and gives a constant  $\Delta K_{th}$ . Therefore, crack growth rates at different R ratios can be shown as a single curve as a function of  $\Delta K_{eff}$  as shown in Figure 2.7.

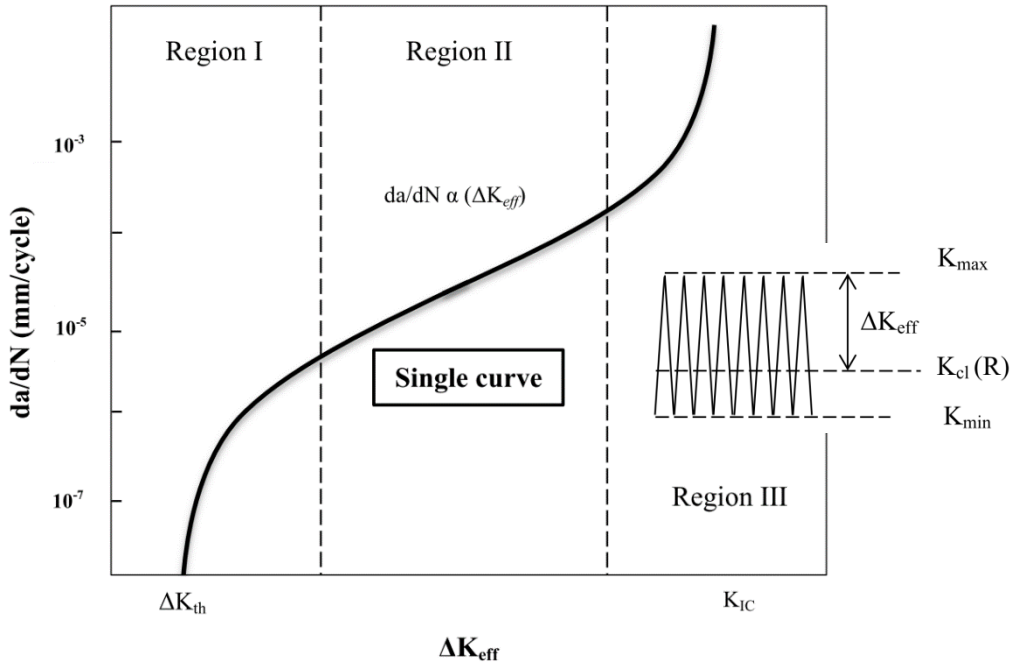


Figure 2.7 Crack growth rates versus  $\Delta K_{eff}$  in the three different crack propagation regions

[25, 31]

### a) Crack closure in different crack growth rates regions

It was reported that plasticity induces compressive residual stress in the crack wake, which leads to crack closure in the Paris region [43]. This assumption was validated with compliance measurements and fractographic evidence [44, 45]; however, fatigue tests in the near-threshold region revealed that other factors can also induce crack closure [46, 47].

Plasticity is higher on the surface of the specimen as compared to the center of it [48], as shown in Figure 2.8a. Removing material at the surface of the specimen around the crack and decreasing its thickness lead to a decrease in the estimated crack closure level at higher  $\Delta K$  values (8.8 and 17.6  $\text{MPa}\cdot\text{m}^{1/2}$ ) in the Paris region in an 7075-T6 aluminum alloy. Crack closure level reaches a constant value at certain thickness as shown in Figure 2.8b [49]; however, crack closure level remains constant throughout the thickness at the lowest  $\Delta K$  value (2.5  $\text{MPa}\cdot\text{m}^{1/2}$ ) corresponding to the near-threshold region as shown in Figure 2.8b. Thus, it was concluded that plasticity induces crack

closure (plasticity-induced crack closure) mainly on the surface of the specimen (crack flanks) and is higher in the Paris region than in the near-threshold region.

The plastic deformation left in the crack flanks transforms the austenite to martensite in some steels [50, 51]. The austenite phase in steels has a face centered cubic crystal structure. A sufficient amount of deformation transforms the face centered cubic crystals to the body centered tetragonal crystals, which is the martensitic phase [52-55]. It has been shown that this transformation leads to a decrease of ductility at the crack tip and increases crack growth rates in the Paris region. On the other hand, this transformation induces volume expansion in crack flanks, which induces crack closure in the near-threshold region [51, 54, 56, 57].

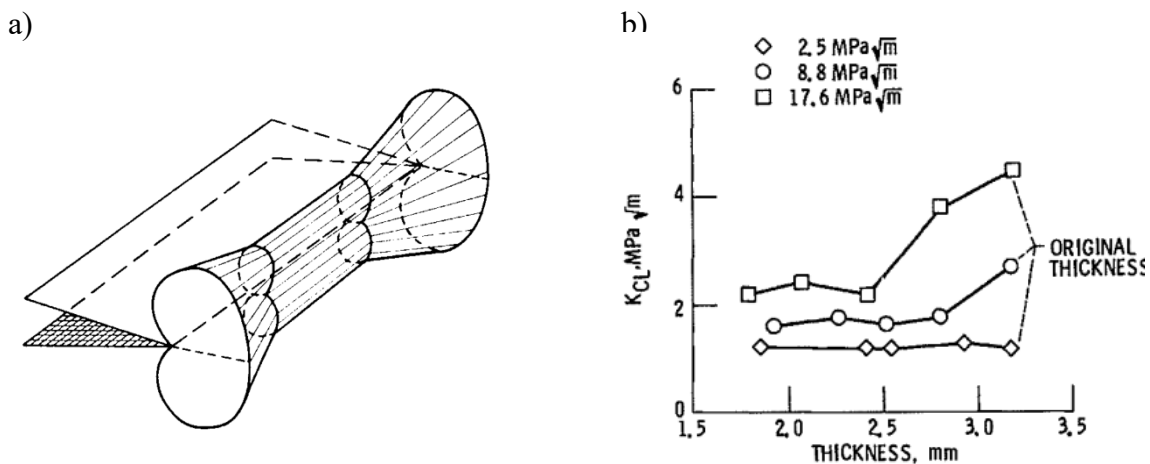


Figure 2.8 a) Variation in plastic zone throughout the thickness, and b) variations in  $K_{cl}$  at three different  $\Delta K$  due to a decrease in thickness in an 7075-T6 aluminum alloy specimen [21, 49]

On the other hand, as the crack grows and deflects from its straight path, it leaves some asperities in the crack wake [58]. A deflected crack under nominal load mode I becomes locally under load modes I and II, so both the tensile and sliding displacement occur [59]. A combination of the crack wake asperities and sliding displacement under mode II creates a mismatch in the crack wake, as shown in Figure 2.9a in an 2090-T8E41 aluminum lithium alloy [60]. This mismatch creates a contact point in the crack wake and makes the crack close before reaching the minimum load, inducing crack closure (roughness-induced crack closure) [61, 62].

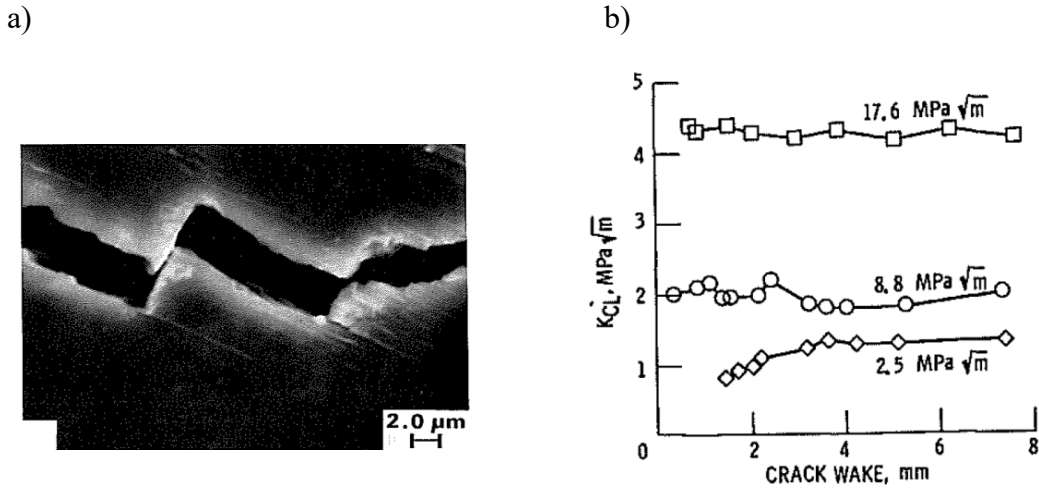


Figure 2.9 a) Surface asperities in the crack wake in an 2090-T8E41 aluminum lithium alloy, b) variations in  $K_{cl}$  at three different  $\Delta K$  due to removal of the crack wake asperities in an 7075-T6 aluminum alloy specimen [21, 49]

Removal of crack wake asperities at the lowest  $\Delta K$  ( $2.5 \text{ MPa}\cdot\text{m}^{1/2}$ ) value in the near-threshold region decreased the crack closure level, as shown in Figure 2.9b [49]; however, this wake removal did not affect crack closure levels at higher  $\Delta K$  values in the Paris region. Thus, it was concluded that surface asperities induce a higher crack closure in the near-threshold region than in the Paris region.

One study suggested that the stress intensity factor ( $K$ ) for a deflected crack under modes I and II ( $k_I$  and  $k_{II}$ ) can be estimated by considering the crack angle deflection,  $\theta$ , which is shown in Figure 2.10.

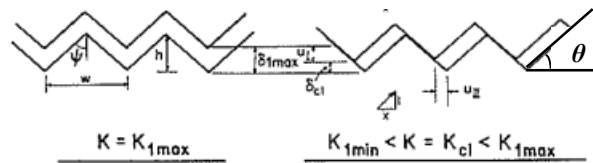


Figure 2.10 Schematic illustration of a zigzag crack path to estimate the  $K_{cl}$  [59, 60]

Thus, an equation was proposed to calculate  $k_1$  and  $k_2$  at the crack tip as followed [11]:

$$k_I = \cos^3(\theta/2)K_I \quad , \quad k_{II} = \sin(\theta/2)\cos^2(\theta/2)K_I \quad (2.10)$$

The  $k_I$  and  $k_{II}$  at the crack tip are lower than  $K_I$ . The equivalent effective SIF range at the crack tip can be estimated using the maximum energy release rate theory [6]:

$$k_{eff} \approx (k_I^2 + k_{II}^2)^{1/2} \quad (2.11)$$

The above equation leads to an effective SIF range ( $\Delta K_{eff}$ ) of a deflected crack. This range over SIF in load mode I ( $\Delta K_I$ ) for a straight crack leads to the following equation:

$$U = \Delta k_{eff} / \Delta K_I \approx \left( \cos^6\left(\frac{\theta}{2}\right) + \left( \sin^2\left(\frac{\theta}{2}\right) \cos^4\left(\frac{\theta}{2}\right) \right) \right)^{1/2} \quad (2.12)$$

Another study suggested that the crack closure can be estimated from surface asperities in the crack wake with the following equation (adapted from [58, 59]):

$$U = \frac{1}{1-R} \left( 1 - \sqrt{\frac{2\gamma x}{1+2\gamma x}} \right) \quad (2.13)$$

where  $x$  is equal to the displacement induced by load mode II over load mode I ( $x = u_{II}/u_I$ ), and  $\gamma$  is equal to the height of an irregularity ( $h$ ) over the crack length deflection from the straight path ( $w$ ), ( $\gamma = h/w$ ), as shown in Figure 2.10.

Another type of crack closure can be induced by oxidation in the crack wake. This closure occurs in steels sensitive to oxidation, where the environment can interact with a slow growing crack in the near-threshold region [31, 63].

The  $K_{op}/K_{max}$  is shown for three different alloys at  $R = 0.05$  in Figure 2.11. As the  $\Delta K$  decreases towards low  $\Delta K$  values in the near-threshold region, crack closure levels increase [29]. Crack closure is mainly induced by surface asperities and oxide at low  $\Delta K$ . On the other hand, it is mainly induced by plasticity and phase transformation at high  $\Delta K$ , as shown in Figure 2.11.

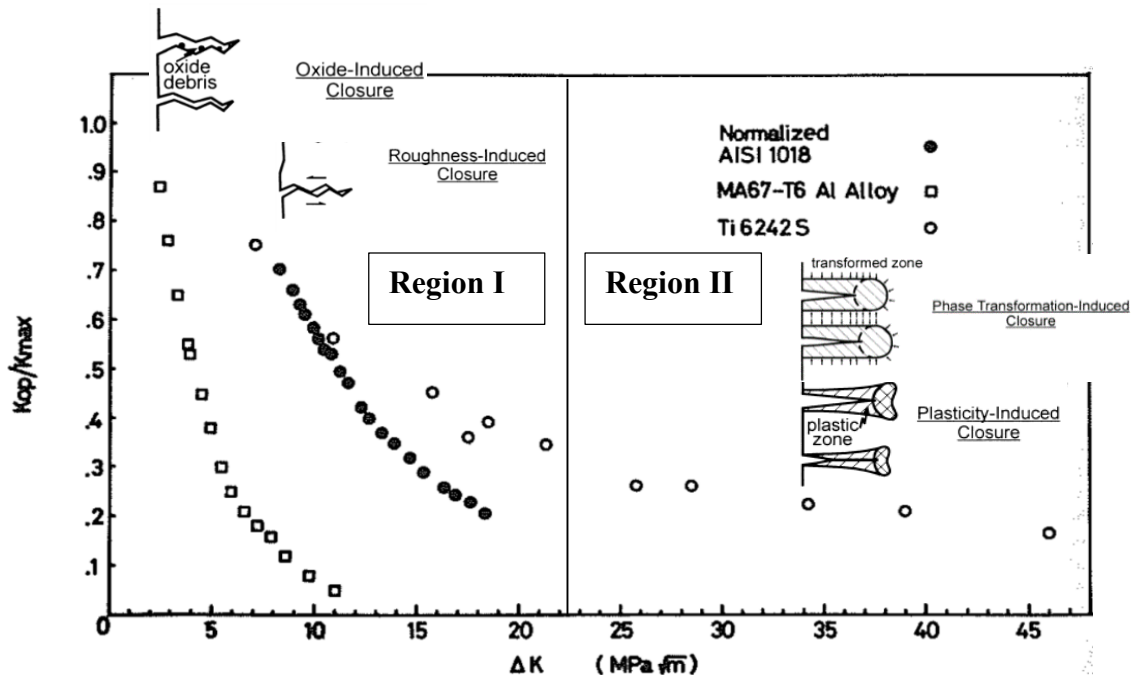


Figure 2.11 Crack closure mechanisms at different crack growth regions at  $R = 0.05$  [29]

### b) Errors in crack closure estimation

The SIF at crack closure,  $K_{cl}$ , is conventionally estimated from the point where a deviation occurs in the linear load-COD curve; this method is suggested by the ASTM E647 [64]. A first contact induced by plasticity and/or surface asperities in the crack wake creates the aforementioned deviation in the load-COD curve, which corresponds to the load at crack closure,  $P_{cl}$  (Figure 2.12).

Using the  $P_{cl}$  to estimate the  $\Delta K_{eff}$  leads to crack growth rates that are equal at all  $R$  ratios. This was conventionally accepted in the literature [25, 65]; however, some new studies have found that the  $K_{cl}$  estimated using the ASTM E647 method, leads to a  $\Delta K_{eff}$  at low  $R$  ratios that is lower than the one at high  $R$  ratios [66]. Therefore, different studies were conducted to explain the difference in  $K_{cl}$  and  $\Delta K_{eff}$  at low and high  $R$  ratios [43, 67-73].

Some studies stated that as the crack wake behind the crack tip is in contact locally, the crack tip can still be in tension [74, 75]. On the other hand, as the load gradually decreases to a minimum load ( $P_{min}$ ), the  $dP/dCOD$  gradually increases until it becomes equal to the one corresponding to the  $dP_{min}/dCOD_{min}$ . Therefore, there is a gradual decrease in the  $P_{cl}$  point until it reaches the  $P_{min}$ . This gradual decrease makes it difficult to define a  $P_{cl}$  point in the load-COD curve.

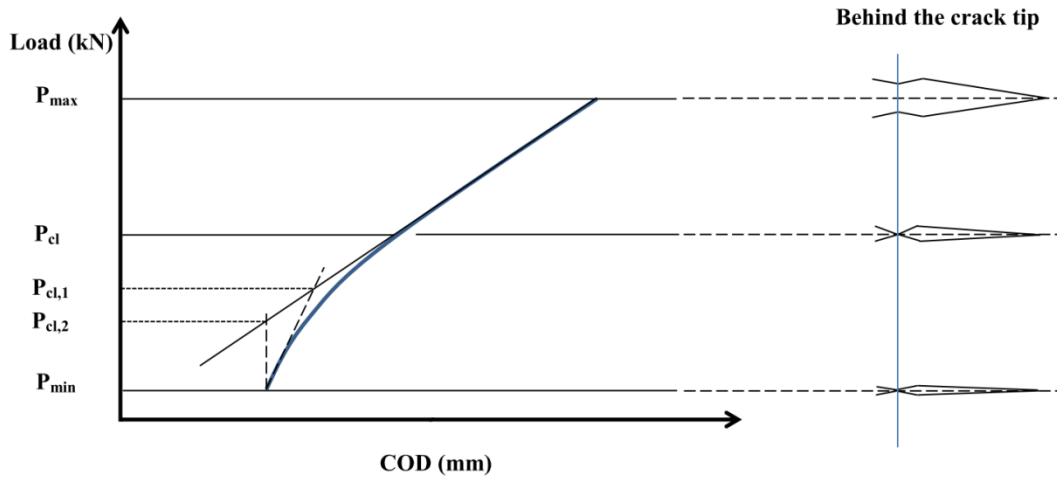


Figure 2.12 Schematic of load and crack opening displacement measured from crack mouth clip gauges behind the crack tip

As a result, different methods are proposed to estimate  $P_{cl}$  point in the P-COD curve [76-79]. Some studies proposed the intersection between the linear  $dP/dCOD$  at the maximum load ( $P_{max}$ ) and the minimum load should define the  $P_{cl}$  on the load-COD curve (see  $P_{cl,1}$  in Figure 2.12) [80, 81]. Other studies suggested that the intersection between the  $dP/dCOD$  at  $P_{max}$  and the one corresponding to a completely closed crack at  $dP_{min}/dCOD_{min}$  should define the  $P_{cl}$  on the load-COD curve (see  $P_{cl,2}$  in Figure 2.12) [79, 82, 83]. A review of the different estimation methods can be found in [72, 82, 84].

Crack closure at low R ratios is detected using global measurements, but this is not the case at high R ratios; however, it was shown in a recent study that local measurements (strain gauges) near the crack tip at low and high R ratios using the ASTM method lead to a unique  $\Delta K_{eff}$  at all R ratios [85].

Different studies have reported a wide dispersion in the crack closure estimations [36, 86]. For example, two tests were conducted using the same test procedure and measurement technique on two Astroloy nickel based alloys; however, the estimated crack closure levels were different while reaching the fatigue threshold [86]. Heterogeneity in the material causes random distribution of surface asperities in the crack wake, which leads to a variation in crack closure [87]. Other studies have shown that as the geometry, location, and number of asperities in the crack wake vary, the crack closure level also varies [87-89]. Therefore, they concluded that the crack closure cannot be used to estimate the  $\Delta K_{eff}$  [82, 90, 91].

Since it is difficult to determine the  $K_{cl}$  in the load-COD curve, a new test procedure was developed to determine crack closure at the crack tip at low and high  $R$ . This method suggests that the crack propagates when there is a transition in the local stresses from the compression to tension at the crack tip [92]. In this procedure, the crack is loaded at an initial  $\Delta K$  and it is increased step-by-step, as shown in Figure 2.13a at low  $R$  ratios and in Figure 2.13b at high  $R$  ratios, until the crack starts to grow. The SIF corresponding to the crack propagation,  $K_{pr}$ , is defined as the average between the  $K_{max}$  without crack growth and the one with crack growth. As a result, the effective SIF or  $\Delta K$  that makes the crack grow is defined as follows,  $\Delta K_{eff} = K_{max} - K_{pr}(R)$ , so  $K_{pr}$  is only a function of the  $R$  ratio [93]. It has been shown that the  $\Delta K_{eff}$  estimated using this method at low  $R$  ratios is equal to the one measured at high  $R$  ratios using the ASTM method and constant  $K_{max}$  procedure [94].

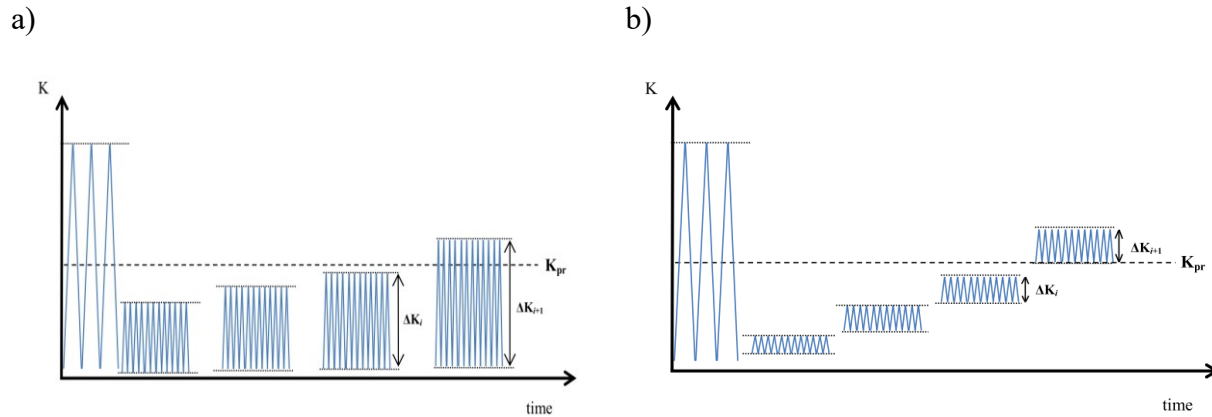


Figure 2.13 Test procedures to determine the SIF corresponding to the crack propagation, a) at low  $R$  ratios, b) at high  $R$  ratios [93-94]

### 2.4.3 Crack growth prediction methods

#### a) Predictions based on $\Delta S$ -N and $\Delta \varepsilon$ -N curves

One of the earliest crack growth prediction methods proposed that the crack grows to certain distance from its tip, called the process zone, for a number of cycles [17]. This number of cycles to accumulate local true plastic strain ( $\varepsilon_p$ ) and to reach true strain at rupture ( $\varepsilon_f$ ); is calculated by using the following equation:

$$\int_0^N 4 \left( \frac{\varepsilon_p}{\varepsilon_f} \right)^{m'} dN = 1 \quad (2.14)$$

It was suggested that a  $m'$  value equal to two gives good results. Other studies suggest that a  $m'$  value equal to the  $c'$  exponent of the Coffin-Manson gives better results [95].

Other methods consider the blunted crack tip as a notch. As shown in equation 2.15, nominal stress ( $\Delta S$ ) in a notched specimen is related to the local stress ( $\sigma$ ) and strain ( $\varepsilon$ ) at the tip of a notch by stress concentration factor,  $k_t$  [96]. The cyclic stress and strain are related by the Romberg-Osgood equation. So they are given as a function of stress  $f(\sigma)$  or strain  $f(\varepsilon)$  [97].

$$k_t^2 = k_\varepsilon k_\sigma = \frac{\Delta \varepsilon E}{\Delta S} \frac{\Delta \sigma}{\Delta S} \rightarrow k_t^2 \Delta S^2 = E \Delta \varepsilon \Delta \sigma = f(\Delta \sigma) = f(\Delta \varepsilon) \quad (2.15)$$

The local stress range,  $\Delta \sigma$ , or strain range,  $\Delta \varepsilon$ , at the notch tip are then considered equal to the estimated SIF range ( $\Delta K$ ) at a distance ( $x$ ) from the blunted crack tip.

$$k_t \Delta S = \Delta \sigma = \frac{\Delta K}{\sqrt{2\pi x}} = f(\Delta \sigma) = f(\Delta \varepsilon) \quad (2.16)$$

The elastic strain is assumed to be minor at the crack tip and is neglected. Thus, the total strain is equal to the plastic strain ( $\varepsilon_p$ ). The Coffin-Manson equation can be solved by estimating the plastic strain. So the number of cycles to rupture ( $N_x$ ) can be calculated as follows:

$$\Delta \varepsilon \approx \Delta \varepsilon_p = \varepsilon_f (N)^c \rightarrow N_x = \left( \frac{\Delta K}{\varepsilon_f \sqrt{2\pi x}} \right)^{1/c} \quad (2.17)$$

In one study, it was estimated that the crack grows when the accumulated damage using the Miner rule within the cyclic plastic zone ( $r_y$ ) reaches unity.

$$\frac{da}{dN} = \int_0^{r_y} \frac{dx}{N_x} \quad (2.18)$$

This method was modified by including a microstructural parameter to take into account the grain size of the material [98].

In another study, the front of the crack tip is divided into even number of blocks ( $\rho$ ). The crack growth rate is estimated from the number of cycles required to break each block [90, 91, 99]. In order to take into account the R ratio effect, the relation between the local stress-strain and the number of cycles to failure are considered using the Smith-Watson-Topper equation [16]. In this method, the linear damage accumulation is considered in order to estimate the damage accumulated at the crack tip.

$$\frac{da}{dN} = \frac{\rho}{N} \quad (2.19)$$

where  $\rho$  is obtained from the ratio between the measured fatigue threshold and the fatigue endurance limit at the corresponding R ratio [100]. Otherwise, the size of the aforementioned blocks is chosen by an initial guess. A trial and error procedure is then used to choose a  $\rho$  value that will correspond to the measured crack growth rate [91].

## b) Prediction methods based on crack growth measurements

The following prediction methods are more fitting methods that are derived from the measured crack growth rates versus the SIF range. The basic method used to predict crack growth in region II is the Paris equation; however, this method does not consider the effect of R ratios. This effect is considered in the following Walker equation [15]:

$$\frac{da}{dN} = \frac{C(\Delta K)^m}{(1-R)^n} \quad (2.20)$$

Another study proposed to consider the R ratios and fracture toughness of the material,  $K_c$ , in the Paris equation. This method predicts crack growth rates in regions II and III, and is given as the following equation [101]:

$$\frac{da}{dN} = \frac{C(\Delta K)^m}{(1-R)K_c - \Delta K} \quad (2.21)$$

Another suggestion was a method that also considered the fatigue threshold,  $\Delta K_{th}$ , and is given as the following equation [102]:

$$\frac{da}{dN} = \frac{A}{\sigma_y E} (\Delta K^2 - \Delta K_{th}^2) \left( 1 + \frac{\Delta K}{K_c - K_{max}} \right) \quad (2.22)$$

where  $A$  is a fitting parameter,  $\sigma_y$  is the yield stress and  $E$  is the young modulus of the material. Since  $K_{max}$  is equal to  $\Delta K/(1-R)$ , the effect of the R ratio is considered in the equation. The aforementioned method predicts crack growth rates in three regions.

On the other hand, one of the most successful prediction methods considers closure-free crack growth rates as a function of  $\Delta K_{eff}$ . As a result, crack growth rates can be predicted by using a single parameter ( $\Delta K_{eff}$ ) for all three regions and is given by Equation 2.9.

## 2.5 Crack growth under variable amplitude loading

### 2.5.1 Basics and definitions

The recorded load spectra of the majority of engineering structures are not subjected to a constant maximum load with constant amplitude. There are variation in both parameters, thus it is conventionally called variable amplitude loading. Depending on the structure, there are many variations in load parameters and their orders or sequences. Most of the studies have investigated the effect of really simplified variable load spectrum on crack growth rates in steels.

In the simplified load spectrum, load cycles that have equal amplitude are called baseline cycles. When a higher load amplitude cycle as compared to the baseline cycles intercut them, the load spectrum is a so-called variable amplitude loading. A higher load amplitude cycle that has a higher  $K_{max}$  level as compared to baseline cycles is called an overload. A higher load amplitude cycle that has a lower  $K_{min}$  level as compared to the baseline cycles is called an underload [103-105].

Overloads or underloads that intercut the baseline cycles periodically are called the periodic overloads or periodic underloads. Here the studies conducted on the effect of an overload, periodic overloads, underload, and periodic underloads on the crack growth of baseline cycles are reviewed in the Paris region first and then in the near-threshold region [45, 106].

## 2.5.2 Effects of overloads and underloads in crack growth regions

### a) Paris region

A procedure similar the one under constant amplitude loading can be conducted by increasing an initial  $\Delta K$  and  $K_{\max}$  at constant R ratio for baseline cycles and periodic underloads to measure crack growth rates; however, an increasing  $d\Delta K/da$  and  $dK_{\max}/da$  can affect the crack growth rate under periodic underloads [107]. Therefore, in most studies, it was decided to conduct crack growth at a constant  $K_{\max}$  in order to better measure the interaction between baseline cycles and overloads or underloads.

An overload is a load amplitude cycle that is larger than the baseline load cycles and which momentarily increases the size of the monotonous plastic zone [108]. The overload applied momentarily increases the crack growth rate of baseline cycles, as shown in Figure 2.14a [107]. The crack growth rate then decreases gradually until it reaches a minimum rate, then it gradually increases to reach the steady and constant growth rate of the baseline cycles under constant amplitude loading. The average crack growth is lower rate as compared to the constant amplitude loading. The crack length affected by the overload is denoted as  $\Delta a_{OL}$ .

The required number of cycles to grow the  $\Delta a_{OL}$  under constant amplitude loading is denoted as  $N_{CA}$  (Figure 2.14b); however, after an overload, a high number of cycles, denoted as  $N_{OL}$ , is needed for baseline cycles with low crack growth rates to grow  $\Delta a_{OL}$  [107, 109]. This number of cycles is deducted from the  $N_{CA}$  to estimate the number of cycles during which the crack does not grow after an applied overload. This number of cycles corresponds to the crack growth retardation and is denoted as  $N_R$  in Figure 2.14b[108].

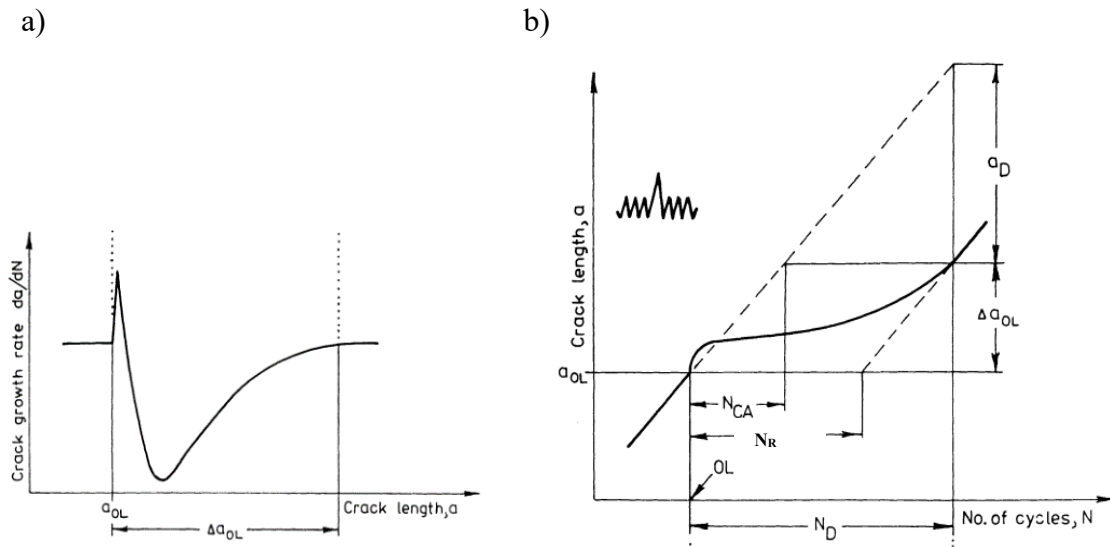


Figure 2.14 Crack growth after an applied overload, a) crack growth rate as a function of crack length, b) crack length as a function of number of cycles [108]

The crack length,  $\Delta a_{OL}$ , is equal to the monotonous plastic zone size created by the overload in an 2024-T3 aluminum alloy [107]. This is given by the following equation:

$$\Delta a_{OL} = \frac{1}{\pi d} \left( \frac{K_{max,OL}}{\sigma_{ys}} \right)^2 \quad (2.23)$$

where  $K_{max,OL}$  is the  $K_{max}$  level corresponding to the overload, and  $d$  depends on the stress state at the crack tip. It is equal to 1 under plane stress and equal to 3 under plane strain; however, the  $\Delta a_{OL}$  also depends on the crack growth rate of baseline cycles (Equation 2.24). This affected length is larger, when the crack growth rate of baseline cycles is in the near-threshold region as compared to the Paris region due to the higher induced crack closure [110-114].

The crack growth of baseline cycles intercut with periodic overloads was investigated in several studies [109, 112, 115, 116]. It was reported that as the distance between periodic overloads changes, it may induce an acceleration or retardation of the crack growth of baseline cycles. Periodic overloads applied after 10 baseline cycles induced a crack growth acceleration in baseline cycles [116]. It was concluded that strain hardening induced by overloads at the crack tip may cause this acceleration; but it decreases rapidly for the next cycles.

On the other hand, a maximum retardation occurs when the subsequent overload was applied at one-fourth of the monotonic plastic zone created by the previous overload in an 2024-T3 aluminum alloy [109]. This retardation was 20% higher than the one induced from each overload applied separately. Therefore, it was stated that there is an interaction between overloads. As the distance between overloads increases, the interaction between them decreases. There is no interaction when the subsequent overload is applied after a distance equal to three times the monotonous plastic zone size of the previous overload in an 2024-T3 aluminum alloy [109, 112].

An underload ( $R_{UL} \geq 0$ ) is a load amplitude cycle that is larger than baseline cycles and which momentarily increases the size of the cyclic plastic zone. A compressive underload ( $R_{UL} < 0$ ) slightly increases the crack growth rate of baseline cycles in the Paris region [106]. It was concluded that the crack is totally closed under compressive underloads. So it has a slight effect on the crack growth rate of subsequent baseline cycles [106]. As it is shown in Figure 2.15, after an applied compressive underload there is an increase in the crack growth rate of the baseline cycles followed by a gradual decrease until it reaches a steady state. This increase occurs in a much shorter crack length and with a lower change in the crack growth rate as compared to the one that occurs after an overload in a 316L austenitic stainless steel (Figure 2.15) [117, 118].

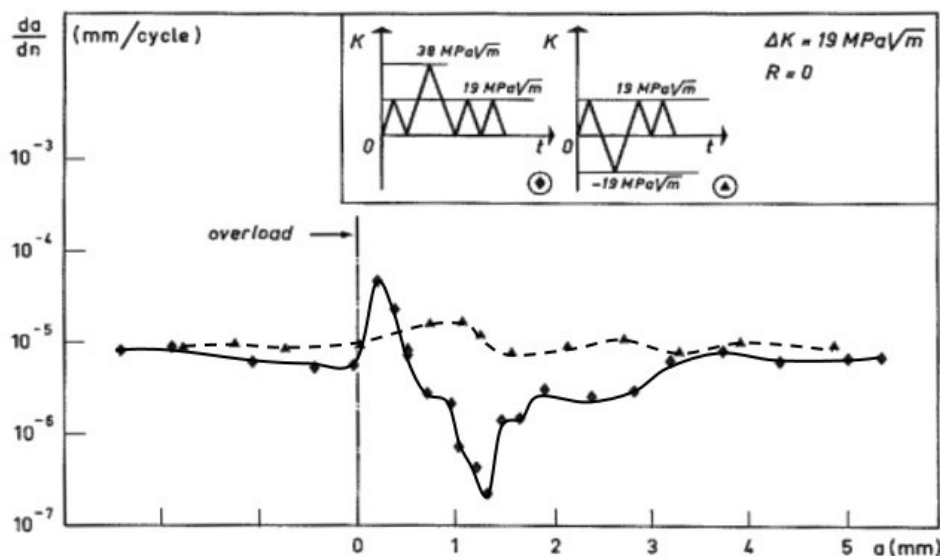


Figure 2.15 Crack growth rates as a function of crack length after an applied overload and compressive underloads in austenitic stainless steel 316L [118]

As discussed earlier, an overload increases the size of a monotonous plastic zone of baseline cycles and the plasticity left in the crack wake, leading to an increase in the compressive residual stress [119]. This increases the roughness-induced crack closure level at baseline cycles in the near-threshold region which leads to a decrease in crack growth rates. As  $\Delta K$  of the baseline cycles increases, the roughness-induced crack closure decreases, so the effect of overload on closure decreases as well. This effect increases again as  $\Delta K$  reaches a level that the plasticity-induced closure reached its maximum in the Region II [120].

On the other hand, compressive underloads crush surface asperities left in the crack wake of baseline cycles, leading to a decrease in the compressive residual stress [121]. This decreases the crack closure at baseline cycles, which leads to an increase in their crack growth rate. Residual stress after an overload or underload reaches a steady state value after a number of cycles [122]. A schematic representation of the crack closure level, the  $K_{op}/K_{max}$  variation after the application of an overload or underload as compared to the constant amplitude loading in the three different regions, is shown in Figure 2.16 [29, 103, 123].

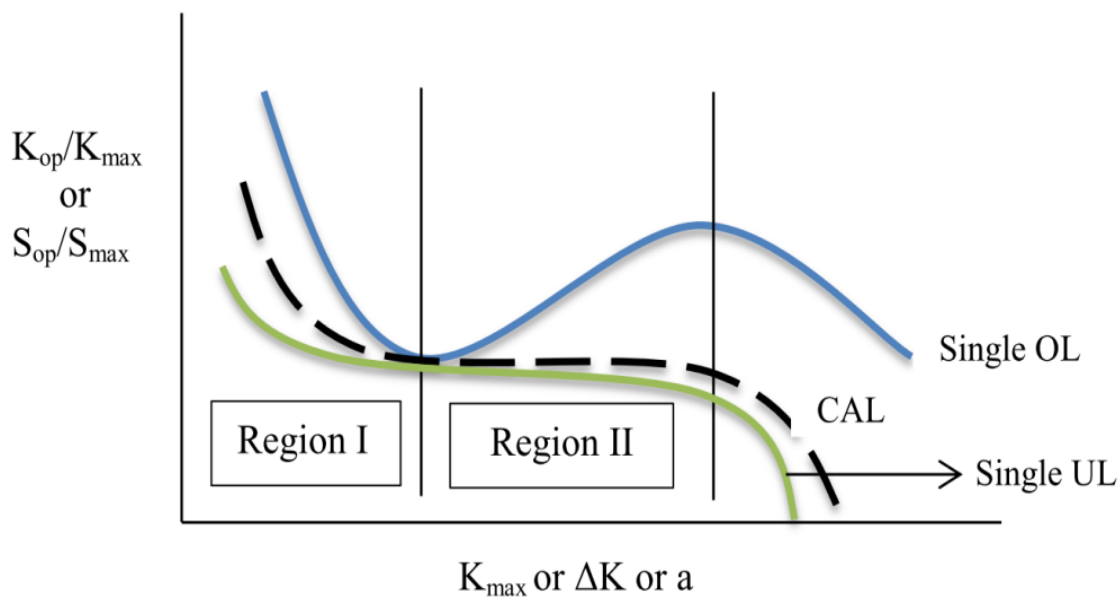


Figure 2.16 Schematic of crack closure variation after an applied overload and underload at different crack growth regions (adapted from [123])

Plastic replicas on the crack tip were taken after an applied overload. These replicas were examined using a scanning electron microscope [116]. These observations revealed that crack tip blunting

occurs after an overload and crack tip shape becomes similar to a notch. The required number of cycles to re-grow the crack from a notch is assumed to cause the retardation; however, the calculated number of cycles in order to initiate a crack from a notch is much lower than the measured one [75].

On the other hand, underloads are reported to sharpen the crack tip. This sharpening is reported to accelerate the crack growth of baseline cycles [110, 124]; however, a study reported that the crack tip was slightly blunted after an applied underload [116].

In some studies, specimens were strain hardened monotonically at a plastic strain equal to 3% in an 2024-T3 aluminum alloy [125]. Crack growth at  $R = 0.1$  in the strain-hardened specimen was higher than unstrained specimens [125-127]. It was concluded that two factors cause higher crack growth rates in strain hardened specimens. The first one is strain hardening at the crack tip, which reduces ductility. The second one is lower crack closure levels in strain hardened specimens as compared to unstrained ones [125]. The strain hardened specimen has higher yield stress, so the plastic zone size is smaller leading to a smaller plasticity-induced crack closure on the crack wake.

The case of periodic underloads and compressive underloads was investigated in literature [116, 120, 128, 129]. It was reported that as the distance between underloads decreases, the acceleration increases until a maximum is reached [116]. This maximum acceleration is attributed to the strain hardening ahead of the crack tip inducing a higher mean stress which leads to an increase in crack growth [116].

### **b) Near-threshold region**

Different test procedures are proposed to measure fatigue crack growth rates in the near-threshold region and reach the fatigue threshold. In some studies, after a conventional pre-cracking, crack growth rates under constant amplitude loading are decreased to reach the fatigue threshold of baseline cycles (ASTM or constant  $K_{max}$  procedure) [130]. An overload or underload is then applied to observe its effect on the fatigue threshold of baseline cycles [130, 131].

Other studies applied the decreasing gradient proposed by ASTM for baseline cycles and periodic overloads or underloads to reach the fatigue threshold. In other procedures, the  $K_{max}$  was kept constant, while the  $\Delta K_{BL}$  was decreased to reach the fatigue threshold under periodic overloads or underloads. These procedures are explained in detail in Chapter 7 for periodic underloads [132].

Here, the effects of overloads and underloads on crack growth rates in near-threshold region are reviewed.

An overload increases the fatigue threshold of baseline cycles. As the  $K_{\max,OL}$  increases, the fatigue threshold of baseline cycles also increases. This increase was higher for a nickel based alloy as compared to the titanium alloy 6Al-4V [120]; however, an applied overload with a  $K_{\max,OL}$  smaller than 10% of the  $K_{\max}$  of baseline cycles did not modify the fatigue threshold of baseline cycles for both aforementioned materials [113].

On the other hand, it has been shown that periodic overloads can increase the crack growth of baseline cycles at  $\Delta K$  that is lower than the fatigue threshold in low carbon steels [133]. This means that the fatigue threshold of baseline cycles is decreased. This decrease was ascribed to a change of dislocation configuration ahead of the crack tip caused by overloads [103, 133, 134].

In the case of underloads, three compressive underloads in the near threshold region showed that the crack reinitiated under baseline cycles in an 7150 aluminum alloy [128, 135, 136]; however, the crack growth rates gradually decreased until the crack stopped growing. It was concluded that compressive underloads crush surface asperities in the crack wake and cause the crack to be re-initiated [135].

On the other hand, periodic underloads and periodic compressive underloads ( $R_{UL} < 0$ ) increase the crack growth rate of the baseline cycles, which leads to a decrease in  $\Delta K_{th}$  of baseline cycles under constant amplitude loading decrease [114, 128, 135]. It was shown that as frequencies of applied periodic underloads and compressive underloads increase, the fatigue threshold of baseline cycles decreases to lower values for low carbon steels and aluminum alloys [120, 128]. It was also shown that underloads decrease the crack closure level of subsequent baseline cycles. As the crack grows, the crack closure gradually increases as it returns to its steady state of baseline cycles [120, 137, 138].

### 2.5.3 Crack growth prediction methods

One of the earliest methods to predict failure under variable amplitude loading was of Miner's linear cumulative damage method [139]. A similar method was employed using the Paris equation and has been referred to as linear damage summation (LDS) [116]. In this method, crack growth ( $\Delta a$ ) is calculated using the Paris equation for each cycle and is incremented to the previous crack length until it reaches a critical length ( $a_f$ ), as shown in Equation 2.25.

$$a_f = a_0 + \sum_{i=1} \Delta a, \quad \Delta a = C(\Delta K_i)^m \quad (2.24)$$

This method can be employed for periodic load blocks too, as shown in Equation 2.25. Crack length is incremented for each load block ( $\Delta a_{block,j}$ ) [10].

$$a_f = a_0 + \sum_{j=1} \Delta a_{block,j}, \quad \Delta a_{block,j} = C(\Delta K_j)^m N_j \quad (2.25)$$

The linear summation method is employed in engineering designs because of its simplicity [140]; however, the effect of interaction between different load cycles is not considered in this method. In particular the effect of overloads or underloads on the crack growth of subsequent baseline cycles is not considered. A load interaction factor is determined by comparing crack growth measured under variable amplitude loading ( $\Delta a_{measured}$ ) to the predicted growth by LDS ( $\Delta a_{LDS}$ ),

$$\text{load interaction} = \frac{\Delta a_{measured}}{\Delta a_{LDS}} \quad (2.26)$$

A measured crack growth that is lower than the linear damage summation means a crack growth retardation, otherwise it is acceleration [116].

In order to predict the crack growth of the baseline cycles after an applied overloads, Wheeler proposed a modified linear damage summation method [141]. As it was mentioned earlier, the crack length affected by the overload,  $\Delta a_{OL}$ , is again equal to the size of the overload monotonous plastic size. The Wheeler prediction inserts a load interaction factor  $C_y$  (lower than unity) in the linear damage summation which leads to a decrease in  $\Delta K$  and crack growth of baseline cycles within the monotonous plastic zone size, and is given by the following equations [141, 142]:

$$C_{y,i} = \left( \frac{r_{y,i}}{\lambda_i} \right)^z, \quad \lambda_i = r_{y,OL} - \Delta a_i \quad (2.27)$$

$$a_f = a_0 + \sum_{i=1}^n C_y \Delta a, \quad \Delta a = C(\Delta K_i)^m = C(\Delta S_i \sqrt{\pi a})^m \quad (2.28)$$

As it can be seen in Equation 2.27, the  $C_{y,i}$  is a load interaction factor for each cycle ( $i$ ). The  $r_{y,i}$  is the current baseline cycles monotonous plastic zone size and  $\lambda_i$  is the distance between the crack tip and overload monotonous plastic zone ( $r_{y,OL}$ ), as shown in Figure 2.17a. As the crack grows, the distance between the crack tip and overload monotonous plastic zone sizes decreases, so the  $C_y$

increases from a minimum value to a value of one. The  $z$  is a curve fitting parameter, which depends on the type of applied loads and the material. For this reason the Wheeler method has been criticized for being more of a curve fitting method than a prediction method [143].

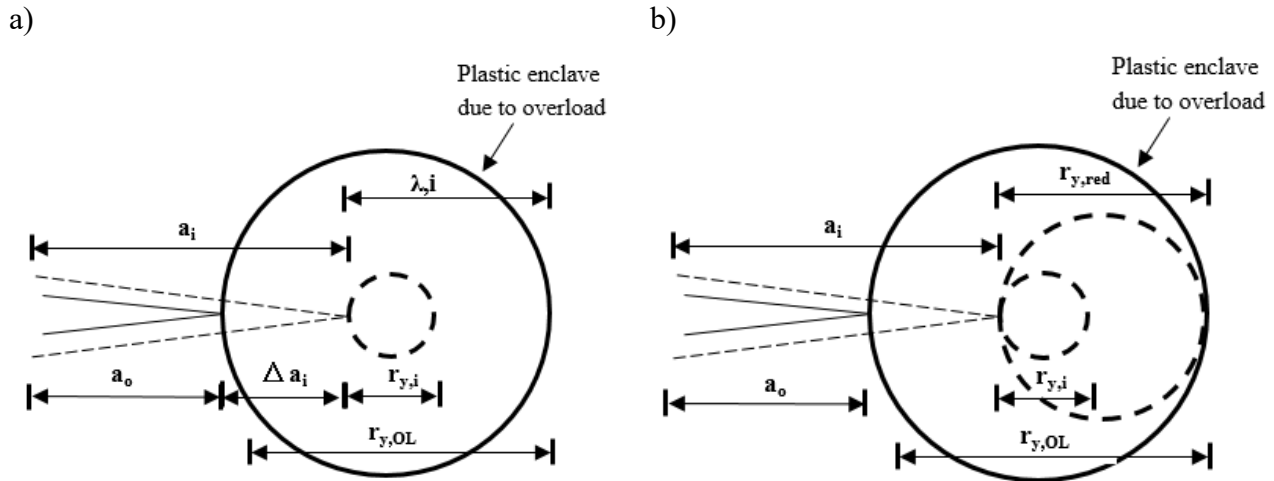


Figure 2.17 Two prediction models, a) Wheeler, and b) Willenborg (adapted from [144])

Later, a modified Wheeler method was proposed to replace the fitting curve parameter  $z$  with the following equation [143, 144]:

$$z = \frac{m}{2} \frac{\log\left(\frac{\Delta K}{\Delta K_{th}}\right)}{\log(K_r)} \quad (2.29)$$

The  $m$  value is the Paris equation exponent,  $\Delta K_{th}$  is the fatigue threshold of the material, and  $K_r$  is the  $K_{max,OL}/K_{max}$  [143].

Willenborg also proposed to use Equation 2.30 to predict crack growth after an applied overload (Figure 2.17b). The  $K_{max,OL}$  is reduced to  $K_{red}$  as given in Equation 2.31. This SIF reduction ( $K_{red}$ ) decreases with increasing crack length ( $a_i$ ) and reaches zero when the crack grows out of the monotonic plastic zone created by the overload,

$$K_{red} = K_{max,OL} \sqrt{1 - \frac{(a_i - a_{OL})}{(R_{p,OL})}} \quad (2.30)$$

Effective parameters,  $K_{max,eff,i}$ ,  $K_{min,eff,i}$ , and  $R_{eff,i}$  are calculated using Equation 2.33:

$$K_{\max,eff,i} = K_{\max,i} - K_{red} \quad K_{\min,eff,i} = K_{\min,i} - K_{red} \quad R_{eff,i} = \frac{K_{\min,eff,i}}{K_{\max,eff,i}} \quad (2.31)$$

The Walker equation is then used to predict crack growth for each cycle.

$$a_f = a_0 + \sum_{i=1}^n \Delta a, \quad \Delta a = C_{R0} \left( K_{\max,eff,i} (1 - R_{eff})^p \right)^m \quad (2.32)$$

In this method,  $\Delta K$  is constant, but a decrease in the  $K_{\min}$  and  $K_{\max}$  levels is applied to decrease crack growth. Several other methods were proposed to improve this method [145-147]. Chang et al. modified the Willenborg method by taking into account the effect of periodic overloads and compressive underloads [144, 146, 147].

As seen in Figure 2.18, the crack growth rates of baseline cycles measured experimentally after an overload are compared to those predicted by different methods [148]. This figure shows that the Wheeler method predicts in average higher growth rates as compared to measured crack growth rates. On the other hand, the Willenborg method predicts lower crack growth rates as compared to the measured ones. Both methods do not predict the initial acceleration of the crack growth rate.

Note that the Wheeler and Willenborg methods were developed based on results of an applied single overload on baseline cycles with a crack growth rate corresponding to the Paris region; however, the crack length retardation can be larger as baseline cycles approach the near-threshold region [110].

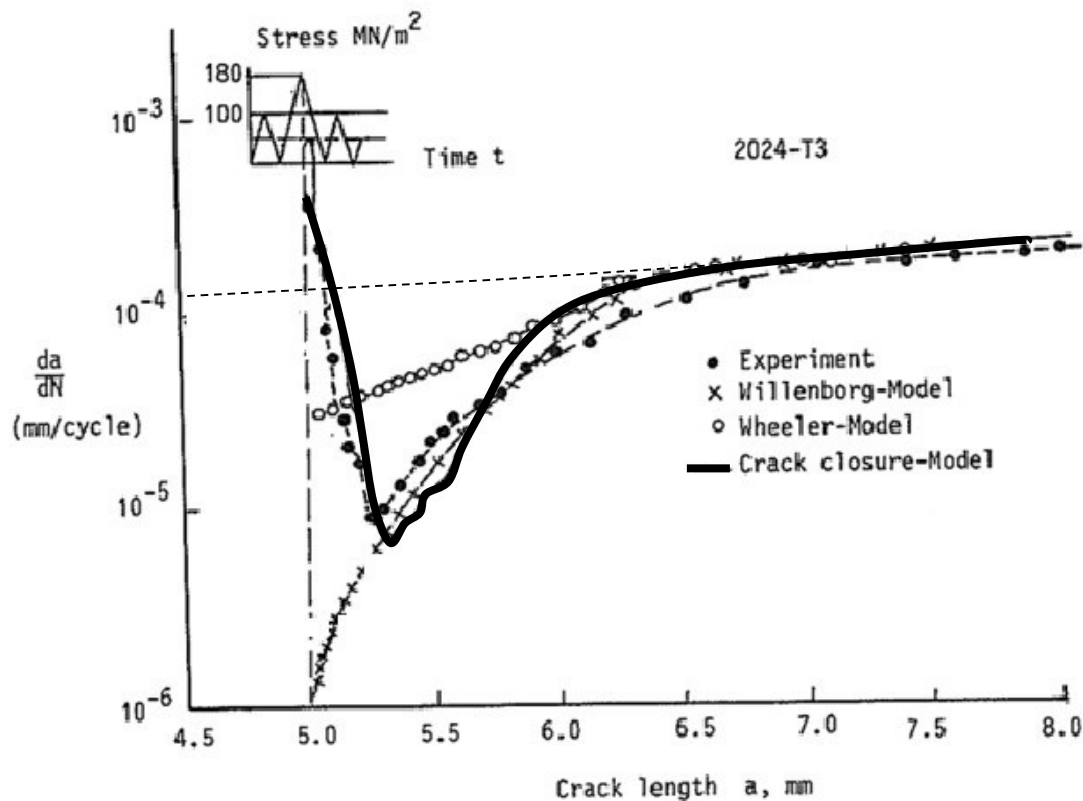


Figure 2.18 Prediction of the crack growth rate following a single overload [148]

Measured crack growth rates are also compared to the ones estimated using the measured crack closure. The estimated  $\Delta K_{\text{eff}}$  was used to predict crack growth rates of baseline cycles after an overload. This method gives results that are close to measured crack growth rates (Figure 2.18); it results in a slightly lower minimum crack growth rate as compared to the measured one followed by higher crack growth rates. In another study, crack growth rates of baseline cycles estimated by the  $\Delta K_{\text{eff}}$  were always lower than the ones measured for a structural steel BS 4360 50B [75]. It was concluded that a high estimated  $K_{\text{cl}}$  results in a lower  $\Delta K_{\text{eff}}$ , which leads to a lower crack growth rate. The  $K_{\text{cl}}$  is lower than the one estimated in the load-COD curve, so the real  $\Delta K_{\text{eff}}$  is higher than the estimated one. This behavior is known as discontinuous crack closure behavior [75].

On the other hand, different methods that use crack closure have been employed for complex and random stress spectra. These methods are called ONERA, CORPUS and PREFASS [144, 149-152]. As an example, in the CORPUS model, crack closure is estimated from the  $da/dN$ - $\Delta K_{\text{eff}}$  curve already measured. The  $K_{\text{op}}$  is then updated for each load cycle by considering the  $K_{\text{max}}$  and  $K_{\text{min}}$  of previous loads. The  $K_{\text{op}}$  in each load cycle is compared to previous ones and the maximum one is

chosen to estimate the  $\Delta K_{\text{eff}}$  of the current cycle. The estimated  $\Delta K_{\text{eff}}$  is used to predict crack growth for each cycle [151]. As shown in Figure 2.19, the  $S_{\text{op}}$  level decreases for the underload, however, this level is lower compared to the previous  $S_{\text{op}}$ , so there will be no change in the  $S_{\text{op}}$  level in this case [151, 153].

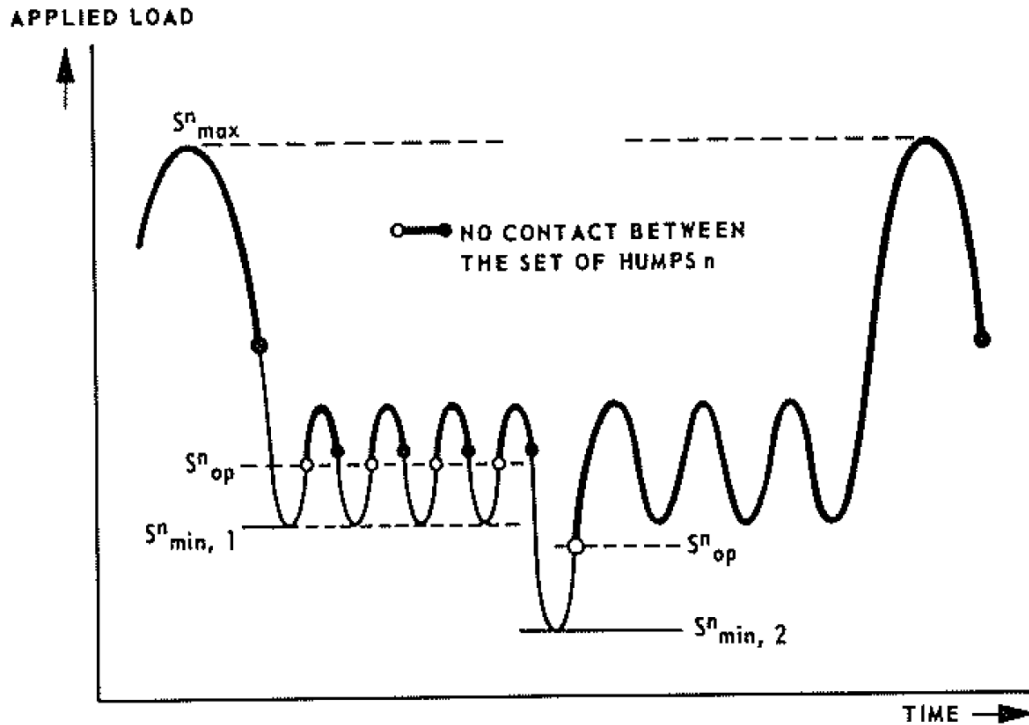


Figure 2.19 Example of CORPUS crack closure model in a simplified spectrum [151]

## 2.6 Conclusion of the literature

The difference in crack growth rate between materials are mainly explained by crack closure mechanisms in the literature, which are mainly plasticity-induced crack closure and roughness-induced crack closure. Therefore, those crack closure mechanisms will be investigated in the studied steels. They will aid to explain the difference in crack growth rates between each steel at different R ratios.

Different test procedures are proposed in the literature in order to measure crack growth rate under variable amplitude loading. After investigating the literature, the constant  $K_{\text{max}}$  procedure will be used in order to conduct the experimental fatigue tests. This procedure leads to a better interaction between load cycles and will minimize the crack closure while reaching the fatigue threshold. A

new test procedure in order to measure fatigue threshold under variable amplitude loading at very low crack growth rates will be proposed. However, these procedures should have a value that is close to the real load conditions otherwise these interactions and the fatigue threshold depends on the level of  $K_{max}$  values.

The acceleration factors in the studied steels are not estimated in the literature, therefore this study will give the acceleration factor for those steels. Moreover, the mechanisms that will lead to an increase in crack growth compared to the LDS prediction will be proposed by considering the mechanism proposed in the literature.

## CHAPTER 3 METHODOLOGY AND EXPERIMENTAL PROCEDURE

### 3.1 Methodology

#### 3.1.1 Stress spectra in turbine runners

The water hits the runner blade and induces tensile stresses that vary depending on the region of the blades. A finite element simulation is performed in order to estimate these stresses in different regions of the blade [154]. These regions are shown in Figure 3.1a. In region A, the stress is the highest on the blade, but a lower stress is applied on region B and C.

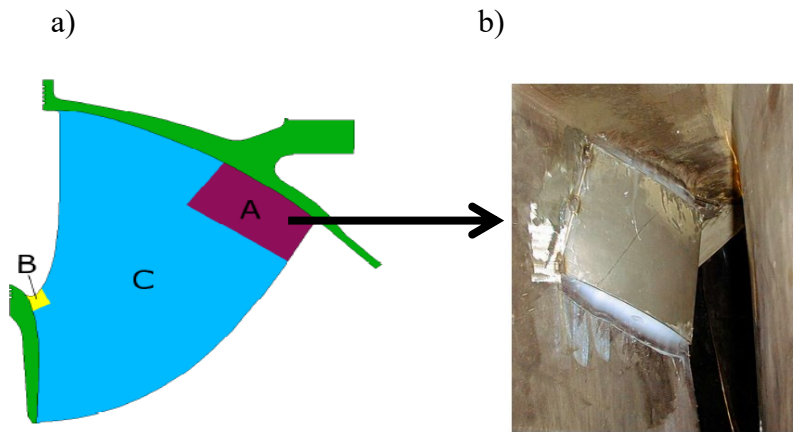


Figure 3.1 a) Different regions of a runner blade based on stress magnitude [154], and b) steel plate filled with epoxy and silicone to protect strain gauges installed on region A of a runner blade [4]

Strain gauges are installed to measure the strain applied on region A of the blade while the runner is operating. The results of two different measurements are shown in Figure 3.2. Measured strains are converted to stresses.

Small stress cycles of very high frequency are generated by a small amount of water flow that is directed by partially opened wicket gates to blades at the beginning of the runner operation. These cycles generate startup and spin-no-load (SNL). A maximum opening of wicket gates then directs a maximum flow to runner blades. As a result, the tensile static stress rises to its highest level. As seen in Figure 3.2a, the stress amplitude of small cycles is low and reaches a few MPa. Figure 3.2b shows that the stress amplitude of small cycles is high and reaches tens of MPa.

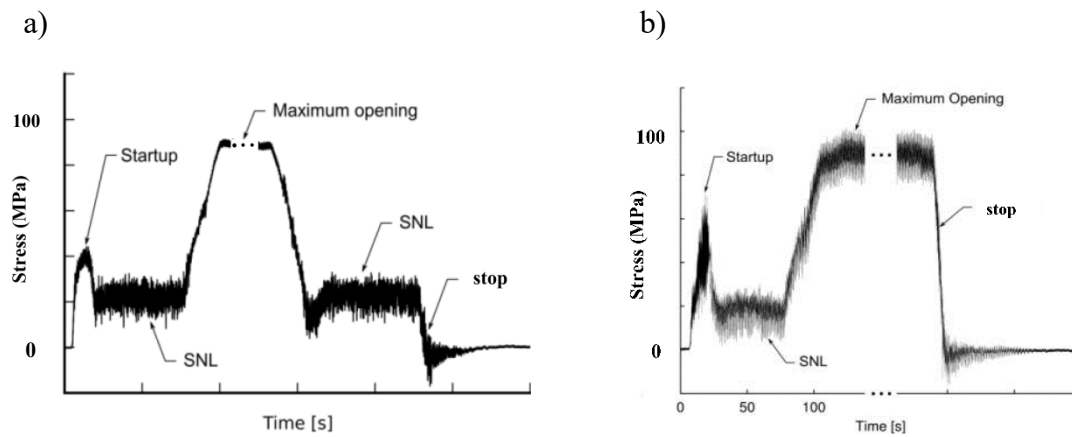


Figure 3.2 Typical stress spectrum imposed on turbine runners with small cycles superimposed to the highest tensile static stress, a) small cycles with low stress amplitudes, and b) small cycles with high stress amplitudes (adapted from [155, 156])

On the other hand, large stress amplitude cycles of low frequency are generated by changing the working conditions of the power station, i.e. start/stop (SS) sequences, power output variations (POVs) and load rejection (overspeed).

Defects and residual stresses are generated in runners during the fabrication process. The above-mentioned small and large stress amplitude cycles during the operation make defects to grow in turbine runners. This growth should not lead to a failure during the design life of the runner i.e. 70 years.

Therefore, it is important to use an accurate method to predict the crack or defect growth in runners. To do so, initial semi-elliptical defect dimensions are chosen ( $a \times c$ ) and the stress range in each region of the blade is estimated, so that the corresponding stress intensity factor range can be calculated [154]. The defect or crack growth due to each load cycle is then calculated using crack growth rates versus  $\Delta K$  data under constant amplitude loading. This growth is linearly summed for all cycles during 1 year to predict crack growth. This method is known as the linear damage summation (LDS) prediction method.

Next, this growth is incremented for each year until the end of the design life, which is 70 years. Incremented defect dimensions after 70 years should not exceed critical defect dimensions ( $a_{cr} \times c_{cr}$ ). Otherwise, the procedure is repeated with smaller defect dimensions. Therefore, a trial and error procedure is conducted to estimate initial defect dimensions that will not exceed critical defect dimensions during the runner's lifetime, as shown in Figure 3.3a. Dimensions of the initial semi-

elliptical defect in different regions of the blade that will not cause a failure after 70 years are shown in Figure 3.3b; estimated dimensions for 20 years of design life are also given.

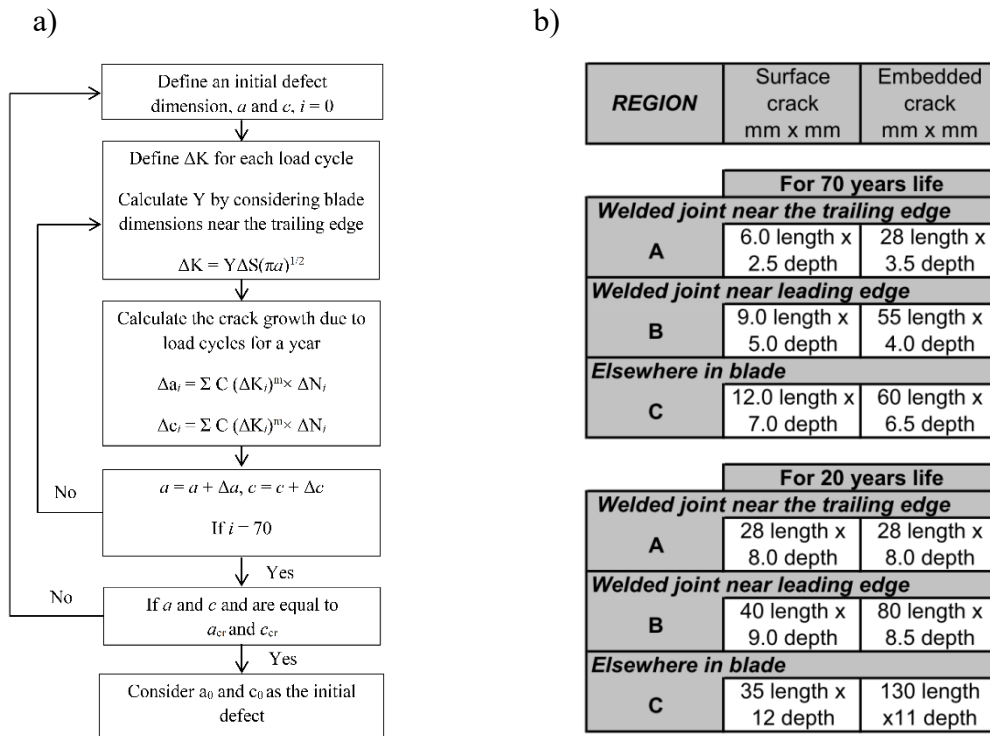


Figure 3.3 a) Linear damage summation employed to predict initial defect dimensions that will not cause rupture for 70 years, b) initial allowable semi-elliptical defect dimensions in different regions of a blade runner

Critical defect dimensions are reached when their corresponding  $K_{max}$  exceeds  $K_{IC}$  or the fatigue threshold of small cycles. Therefore, the fatigue threshold of small cycles should be measured; however, this fatigue threshold can decrease due to periodic large cycles. Therefore, the fatigue threshold of small cycles subjected to intermittent large cycles should be measured to estimate the critical defect dimensions.

### 3.1.2 Stress spectra simplifications

The real stress spectrum has many different types of small and large stress amplitude cycles i.e., start/stop (SS) sequences, power output variations (POVs) and load rejection (overspeed). Studying the effect of all these stress cycles on crack growth can be complicated and is not appropriate for an initial study on the subject. A better approach is to investigate and analyze the effect of interaction between two stress cycles on crack growth. The real stress spectrum is thus simplified and reduced only two stress cycles. Thus, the stress cycles that do not contribute to a significant crack growth are neglected in the simplified stress spectrum.

In the stress spectrum, the startup and SNL last for few cycles at the beginning or end of each sequence and have a low  $S_{max}$ , as shown in Figure 3.2. Thus, they only account for few cycles with low stress amplitudes in the stress spectrum, which do not contribute to a large crack growth, so they are neglected. Load rejections due to sudden uncoupling between the rotor and turbine runner rarely occur in the load spectrum and so they are also neglected in the stress spectrum.

Consequently, only three stress cycles remain in the simplified load spectrum: small cycles, POVs and SS sequences. The stress amplitude of small stress cycles and generation of POVs depends on the type of power stations [154, 157].

In power stations that generate POVs, small cycles have low amplitudes, as shown in Figure 3.2a. They induce a  $\Delta K$  that is much lower than the fatigue threshold and so they can be neglected. On the other hand, in power stations that do not generate POVs, the small cycles have high amplitudes, as shown in Figure 3.2b. They induce a  $\Delta K$  that is close to the fatigue threshold and may induce a crack growth, so they are considered in the load spectrum.

Therefore, POVs and SS sequence remain in the stress spectrum in the first case and small cycles and SS sequences in the second. As a result, two studies are defined to investigate the effect of these two stress cycles on crack growth in each case. There are variations in the stress amplitude of small cycles. For simplicity, the highest stress amplitude is considered to be constant for all cycles.

#### a) First study

In a first study, crack growth is measured under POVs and SS sequences. This growth is compared to the one predicted by LDS using crack growth rates versus  $\Delta K$  data of large cycles under constant amplitude loading. Fatigue tests are conducted on the 415, ASTM A516 and 304L steels.

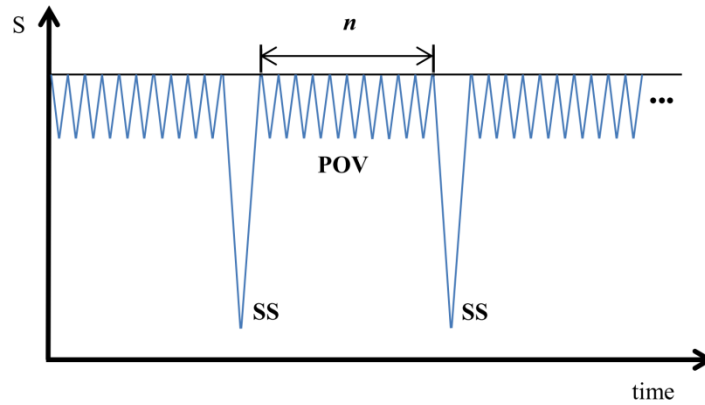


Figure 3.4 Simplified load spectrum with POVs and SS sequences

Crack growth is measured at  $K_{\max} = 19.43$  and  $40.77 \text{ MPa}\cdot\text{m}^{1/2}$ . These  $K_{\max}$  levels are estimated from stress levels and initial defect dimensions in region A of runner blades [154]. The ratio of POV cycles over SS sequences during 70 years of turbine runner lifetime is calculated according to [154] and is shown as  $n$  in Figure 3.4. The  $n$  values range from a minimum of 3 to a maximum of 10. Measured crack growths induced by POVs and SS sequences are compared to the ones predicted by LDS, and results are reported in Chapter 6. This study verifies if LDS can be employed to predict defect growth in turbine runners.

#### b) Second study

In the second study, the effect of SS sequences on the fatigue threshold of small cycles is investigated. A large number of small cycles with high amplitude are generated during the operation, which can propagate defects. Therefore, it is important to measure a  $\Delta K_{\text{th}}$  corresponding to small cycles that will not propagate defects. SS sequences can further decrease the  $\Delta K_{\text{th}}$  of small cycles. Thus, it is important to estimate the decrease in  $\Delta K_{\text{th}}$  due to SS sequences.

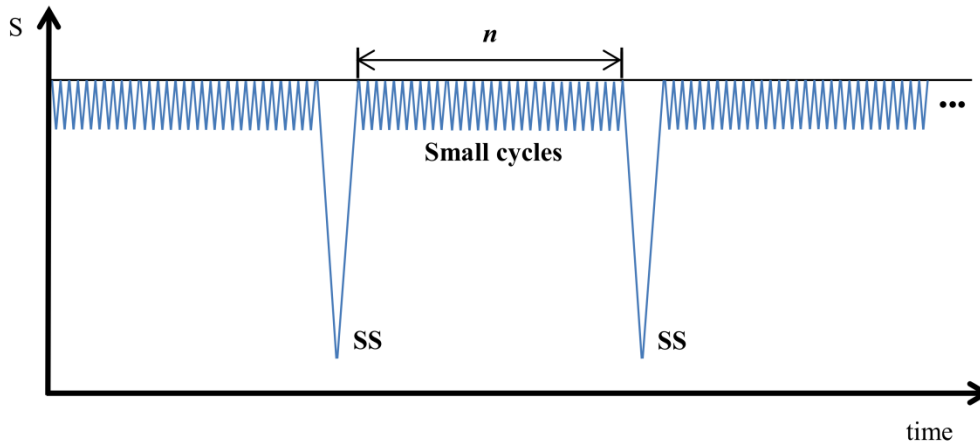


Figure 3.5 Simplified load spectrum with small cycles and SS sequences

Fatigue tests are conducted in the near-threshold region to reach the fatigue threshold. Given that these tests are time consuming, so we decided to reduce the number of studied steels. As a result, we decided to carry on the remaining fatigue tests only on the steels with the lowest and highest strain hardening exponent (see Chapter 6, Table 6.4), which are the 415 and 304L steels, respectively.

The fatigue threshold at a constant  $K_{\max} = 11.11 \text{ MPa}\cdot\text{m}^{1/2}$  is measured using the constant  $K_{\max}$  procedure for the 415 and 304L steels. The ratio of small cycles over SS sequences during 70 years of life design is considered as  $n$ , as shown in Figure 3.5. As a result, periodic underloads are conducted at different  $n$  values ranging from  $10^2$  to  $10^6$ , in the same specimen. Therefore, it is important to investigate the effect of periodic SS sequences on the fatigue threshold of small cycles.

Tensile residual stress due to welding is induced in runners during the fabrication and repair. As the crack propagates in the runner, it can be subjected to this tensile residual stress. This increase in tensile residual stress will increase the  $K_{\max}$  at the defect tip. In the general discussion in Chapter 8, the effect of the  $K_{\max}$  on the fatigue threshold under constant amplitude loading and periodic underloads is investigated. Fatigue tests under periodic underloads were conducted similarly to the one in the second study but at  $K_{\max} = 19.44 \text{ MPa}\cdot\text{m}^{1/2}$ , and the results are compared to the ones at  $11.11 \text{ MPa}\cdot\text{m}^{1/2}$ .

## 3.2 Experimental procedure

### 3.2.1 Material characterization

Material characterization, tensile and fatigue tests were conducted on three different steels, namely the AISI 415, ASTM A516 and AISI 304L. The heat treatment and chemical composition of these steels is given in Chapter 6.

Plates of each steel were received; they were 1000 mm long, 400 mm wide, and 50 mm thick. These plates were cut into smaller pieces with a band saw and then further cut with a precision saw to a size of 50 mm long, 50 mm wide, and 50 mm thick, in three orthogonal planes (LT, LS, and TS). Each plane section was placed in a hot mounting machine, and the resin was added on top of the specimen. The resin was heated up to 170°C and cooled down to room temperature to mount the specimen.

Specimens were then polished using silicon carbide abrasive papers. This process was carried out by increasing the grit numbers at each step from 240 up to 800 grits. The polishing was then continued using diamond suspensions from 6 microns down to 1 micron. Etchants were used to reveal the microstructure of each type of steel, as shown in Chapter 6. Grain size measurements were carried out with an optical microscope equipped with an image analysis software. All measurements were carried out with a magnification of 200 X. The grain size was estimated visually by considering the grain boundaries of each grain. The spherical diameter was defined as the grain diameter size. At least 100 measurements were taken in each plane.

After conducting grain size measurements, specimens were polished with the diamond suspension of 1 micron to conduct microhardness measurements. Vickers microhardness measurements on the three orthogonal planes (10 measurements per plane) were carried out with a force of 100 gf and 15 second dwell time for all steels according to ASTM E384.

In order to conduct an X-ray diffraction analysis, the above-mentioned samples were polished with the diamond suspension of 1 micron and subsequently thinned with acid (75 ml HCl, 75 ml HNO<sub>3</sub> and 100 ml H<sub>2</sub>O) to remove the deformation induced during polishing. The X-ray diffraction analysis was then conducted using a Cu K<sub>α</sub> source radiation with 0.05 degree per 4 seconds for angles 2θ from 40° to 140° using the Rietveld method with an accuracy of ± 1.5%.

### 3.2.2 Tensile testing

The tensile test was conducted for each steel in longitudinal (L) and transverse (T) directions with respect to the rolling direction. Three tests were conducted in each direction on standard specimens, with reduced cross section of dimensions of 30 mm long and 5 mm diameter [158]. An extensometer of 25 mm was attached on the reduced section of the specimen surface in order to measure the strain. Tests were conducted using a servo-electronic machine with a 100 kN dynamic load cell. The displacement was increased with a relative ramp equal to 0.45 mm/min, according to the ASTM E8 standard [158]. Tests were stopped when specimens were fractured.

Young's modulus, the 0.2% yield stress ( $\sigma_{0.2\%}$ ), ultimate tensile strength ( $\sigma_{UTS}$ ), elongation at the rupture ( $\epsilon_r$ ) and strain hardening exponents are given as results in order to compare the three different steels. These parameters are also used as input parameters in da/dN Instron software for fatigue tests.

### 3.2.3 Fatigue testing

#### a) Choice of the specimen

Defects in critical regions of the runner blade are subjected to a combination of tensile and bending loading [1, 4]. The compact tension, CT, specimen induces a tension load and high bending load at the crack tip. Thus, the CT specimen represents the aforementioned loading condition in the runner blade [159]. CT specimens were fabricated with dimensions of 50.8 mm wide and 12.7 mm thick according to the ASTM E647 standard. This specimen is much smaller than the runner blade geometry; however, the fabricated specimen has a lower cost as compared to the real geometry to investigate crack growth under constant amplitude loading and periodic underloads.

#### b) Specimen installation and precracking

Compact tension specimens were tested in the LT orientation. Dimensions in each specimen were verified using a caliper before conducting each test. Tests were conducted using a closed loop servo-hydraulic machine equipped with a 100 kN dynamic load cell for fatigue tests at high  $\Delta K$  values. On the other hand, fatigue tests at low  $\Delta K$  values in the near-threshold region require higher load precision. Thus, they were carried out with a smaller 20 kN dynamic load cell (Figure 3.6), with higher load precision as compared to the 100 kN load cell. The CT specimen was installed on the grips of the hydraulic machine. Optical microscopes were then installed on both sides of the

specimen to observe and measure crack length on its surface. The clip gauge was installed at the mouth of the specimen.

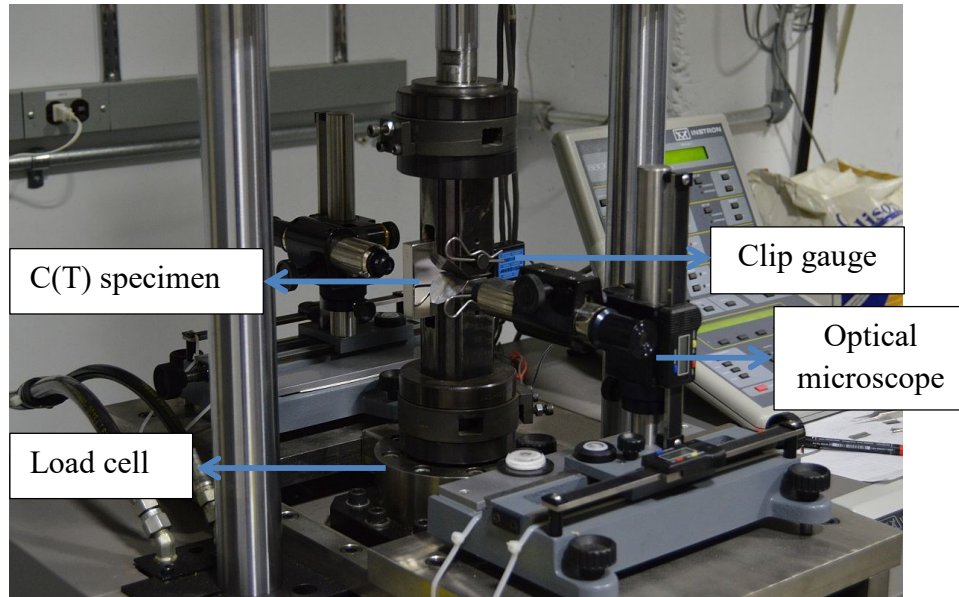


Figure 3.6 Compact tension specimen installed in an Instron servo-hydraulic machine

Atmospheric conditions were periodically recorded with a thermo-hygrometer. The test temperature was 23°C with a relative humidity of 40 % to 45 %. All tests were conducted at 1 Hz for high crack growth rates (first study) and at 15 Hz for low crack growth rates (second study). Crack growth was measured using the optical microscope which has an average resolution equal to  $5 \times 10^{-3}$  mm.

The notch length was measured on both sides of the specimen using the optical microscope. Precracking is required to provide a sharpened fatigue crack with adequate straightness. The precracking procedure was conducted using da/dN Instron software. The crack then grows out of the notch completely and appears on the surface of the specimen. The crack should grow for 2 mm in our specimen, according to ASTM E647 [160, 161].

### c) Detail on da/dN Instron software

The crack growth rate under constant amplitude loading was conducted using da/dN Instron software. In this software, the crack length,  $a$ , was calculated using the following equation:

$$a = (C_1 + C_2u + C_3u^2 + C_4u^3 + C_5u^4 + C_6u^5)W \quad (3.1)$$

the  $u$  value is calculated using the following equation in da/dN software [160, 162].

$$u = \frac{1}{\left(\frac{BE\Delta V}{\Delta P}\right)^{1/2} + 1} \quad (3.2)$$

where  $\Delta V$  is the crack opening displacement measured using strain gauges installed at the mouth of the specimen;  $\Delta P$  is the load range measured using strain gauges in the load cell;  $B$  is the thickness of the specimen, and  $E$  is Young's modulus of the steel.

The values of coefficients  $C_1$  to  $C_6$  in Equation 3.1 are given below and correspond to measurements carried out at the mouth of the specimen,

$$C_1 = 1.001, C_2 = -4.669, C_3 = 18.46, C_4 = -236.82, C_5 = 1214.9, C_6 = -2143.6$$

however, the strain gauge was installed with a knife edge with a width of 1.9 mm from the mouth of the specimen. As a consequence,  $C_1$  to  $C_6$  coefficients in Equation 3.1 were calculated and modified in da/dN software. Corresponding coefficients were calculated according to [162], and using the following equation,

$$C_1 = 1.001, C_2 = -4.752, C_3 = 19.453, C_4 = -257.16, C_5 = 1351.3, C_6 = -2466 \quad (3.3)$$

The estimated crack length from da/dN software should be equal to the one measured with the optical microscope on the surface of the specimen. If there is a difference, the crack length calculated should be adjusted to the one measured by slightly modifying Young's modulus in Equation 3.2.

The  $\Delta K$  in da/dN software is calculated from the crack length estimated using the following equation ( $\alpha \geq 0.2$ ) [163, 164]:

$$\Delta K = \frac{\Delta P}{B\sqrt{W}} \frac{2+a}{(1-a)^{3/2}} (0.886 + 4.64a - 13.32a^2 + 14.72a^3 - 5.6a^4) \quad (3.4)$$

#### d) Software choice to conduct fatigue tests

Tests under constant amplitude loading were conducted using da/dN Instron software; however, in the case of periodic underloads, a periodic and sudden decrease from the  $P_{\max}$  of baseline cycles followed by an increase to the same level is necessary to generate periodic underloads. That said, da/dN Instron software only induces a gradual decrease in the  $P_{\max}$  of baseline cycles followed by a gradual increase until it reaches the  $P_{\max}$ .

This software could not be used to represent periodic underloads loading. So finally, periodic underloads were generated using Wavemaker Instron software. The crack length was measured with the microscope installed on both sides of the specimen. After measuring an average crack length, the load was manually adjusted to have a constant  $K_{\max}$  during the tests.

#### **e) Fractography analysis**

Once the fatigue tests were completed, specimens were fractured into two pieces to observe and analyze fatigued surfaces. These observations were performed using a scanning electron microscope (SEM). Specimens were cleaned by soaking them in ethanol and putting them in the ultrasonic bath. They were then stuck in the specimen holder to be entered into the SEM chamber. The pressure in the vacuum chamber was set at 60 Pa. Observations were generally conducted with a voltage equal to 15 kV. Specimens were at a maximum distance of 7 mm from the beam. Fractography observations were carried out to observe the striation spacing on the fracture surface of each steel. At least four pictures were taken to measure striation spacings, the taken pictures were then analyzed with image analysis software.

## CHAPTER 4 ORGANIZATION OF THE FOLLOWING SECTIONS

In Chapter 5, the ASTM E647 load procedure is used to measure crack growth rates under constant amplitude loading at  $R = 0.1$  and  $R = 0.7$  by reaching the fatigue threshold in the 415 and 304L steels. Measured crack growth rates versus  $\Delta K$  will be compared in both steels at both  $R$  ratios. Crack closure at  $R = 0.1$  will be compared with the one at  $R = 0.7$ . The mechanisms that induce crack closure such as roughness-induced and plasticity-induced crack closure will be analyzed in both steels.

A first published article in Chapter 6 is written in order to investigate the first study by determining the effect of large cycles on crack growth rates in turbine runners. In this article, the microstructure and tensile properties of three wrought steels, AISI 415, ASTM A516, and AISI 304L, used to fabricate the runners will be compared. The experimental procedure will be defined to be similar to the load conditions in the load spectrum. A test procedure at constant  $K_{\max}$  will be defined in order to have a better estimation of the interaction between baseline cycles and periodic underloads.

The crack growth rate under constant amplitude loading will be measured at different  $R$  ratios at two constant  $K_{\max}$  values in those three steels. These measured crack growth rates will be employed to calculate the LDS prediction which is used to predict the crack growth rates under periodic underloads.

Afterwards, the real crack growth rates under periodic underloads will be measured at two constant  $K_{\max}$  values and compared to the LDS prediction in each steel. The accelerations factors in each steel will be specified at each  $K_{\max}$ . The mechanisms that may cause the crack to grow faster under periodic underloads than the one predicted by LDS in each steel will be investigated.

A second published article in Chapter 7 is written in order to investigate the second study by determining the effect of turbine start/stop sequences (periodic underloads) on the fatigue threshold of small cycles at high stress ratio (baseline cycles) in two steels used in turbine runners, i.e. AISI 415 and 304L steels.

In this article, a review of different load procedures to reach the fatigue threshold under constant amplitude loading and periodic underloads will be presented. The procedure, that will give a better estimation of the effect of periodic underloads on the fatigue threshold, will be used to conduct the experiments. Moreover, a new test procedure to measure fatigue threshold at very low crack growth rates under periodic underloads will be proposed.

Keeping  $K_{\max}$  constant, a first load procedure is conducted with decreasing  $\Delta K$  to measure fatigue thresholds at  $2 \times 10^{-7}$  mm/cycle under both constant amplitude loading and periodic underloads at various frequencies. We will be able to specify that after a certain frequency of periodic underloads the fatigue threshold will start to decrease. Therefore, in the load spectrum periodic underloads or start/stop sequences should not exceed this frequency during the 70 years of life design.

Then a second load procedure is conducted to measure fatigue thresholds under periodic underloads at one frequency with increasing  $\Delta K$  of baseline cycles from zero. Therefore, the effect of periodic underloads at very low  $\Delta K$  and low crack growth rate of baseline cycles will be investigated and compared to the ones at higher crack growth rates as well.

In Chapter 8, the results of the last four chapters are summarized and discussed and some additional results will be presented and discussed. The procedures in order to measure crack growth rate under constant amplitude loading in the Paris and in the near-threshold regions will be summarized. The effect of  $K_{\max}$  on crack growth rate under constant amplitude loading and periodic underloads is investigated and the results will be discussed.

In Chapter 9, the conclusion will be given, the load conditions in order to avoid crack propagation due to small cycles will be specified. The acceleration factors that should be considered in order to be able to predict the crack growth rate due to large cycles will be specified. Some recommendations are given for further studies in order to have a better estimation of the interaction between different load cycles based on the non-simplified load spectrum is presented.

## CHAPTER 5 CRACK GROWTH UNDER CONSTANT AMPLITUDE LOADING

### 5.1 ASTM load procedure

The ASTM load procedure is a classical one that is often used to reach the fatigue threshold at low and high R ratios. This procedure is employed to measure crack growth rates under constant amplitude loading at  $R = 0.1$  and  $R = 0.7$  while reaching the fatigue threshold. Crack closure at  $R = 0.1$  and  $0.7$  can be estimated in both steels. Measured crack growth rates versus  $\Delta K$  at  $R = 0.1$  can then be compared with the ones versus  $\Delta K_{\text{eff}}$  at  $R = 0.7$ . Measured crack growth rates in this chapter will be employed in Chapter 6 for the LDS calculation.

### 5.2 Materials and experimental procedures

#### 5.2.1 Materials

The studied materials are the AISI 415, ASTM A516 and AISI 304L steels. Crack growth rate measurements in the near-threshold are time consuming. So, we decided to conduct fatigue tests only on the steels with the lowest and highest strain hardening exponent (see Chapter 6, Table 6.4), which are the AISI 415 and 304L steels.

This study investigates fatigue crack propagation in two wrought steels, namely the AISI 415 and 304L steels. For simplicity, these two steels will be called 415 and 304L, hereafter. The chemical composition and heat treatment of both steels are given in Chapter 6.

#### 5.2.2 Fatigue testing

Fatigue tests are performed using a closed loop servo-hydraulic machine equipped with a 20 kN dynamic load cell. Compact tension specimens are tested with dimensions of 50.8 mm wide and 12.7 mm thick, according to ASTM E647 in LT orientation. Atmospheric conditions were periodically recorded with a thermo-hygrometer. The test temperature was 23°C with a relative humidity of 40% to 45%. All tests are conducted with a frequency equal to 15 Hz. Crack growth rates are measured optically using the secant method.

The compact tension specimen is pre-cracked at a constant  $K_{\text{max}} = 11.1 \text{ MPa}\cdot\text{m}^{1/2}$  and  $R = 0.1$ . This value corresponds to an  $S_{\text{max}} = 170 \text{ MPa}$  applied to a semi-elliptical defect with dimensions of  $2.5 \times 6 \text{ mm}$  at the surface of a turbine runner [154]. After the pre-cracking, the initial  $\Delta K$  and  $K_{\text{max}}$  are

decreased for each step ( $i$ ) with  $C = -0.20 \text{ mm}^{-1}$  (see Equation 4.1) until the crack reaches a growth rate equal to  $2 \times 10^{-7} \text{ mm/cycle}$ .

$$\Delta K_{i+1} = \Delta K_i e^{C(\Delta a)}, \quad K_{\max,i+1} = K_{\max,i} e^{C(\Delta a)} \quad (5.1)$$

Many fatigue tests in literature are conventionally conducted using the ASTM test procedure to reach a  $\Delta K_{\text{th}}$  that corresponds to a crack growth rate equal to  $10^{-7} \text{ mm/cycle}$  [63, 165]. Therefore, this fatigue threshold measured at  $2 \times 10^{-7} \text{ mm/cycle}$  will be referred to as the conventional fatigue threshold,  $\Delta K_{\text{th,conv}}$ , in this test study.

After reaching the SIF range and maximum SIF at the conventional fatigue threshold ( $\Delta K_{\text{th,conv}}$  and  $K_{\max,\text{th,conv}}$ ), these values are increased at  $R = 0.1$  following Equation 3.5 for each step ( $i$ ) with  $C = 0.20 \text{ mm}^{-1}$  until they reach a value equal to 36.7 and 40.77  $\text{MPa.m}^{1/2}$ , respectively.

The crack growth rates at  $R = 0.7$  are also measured using the ASTM procedure. The  $\Delta K$  is decreased from 5.83  $\text{MPa.m}^{1/2}$  (that corresponds to  $K_{\max}$  equal to 19.44  $\text{MPa.m}^{1/2}$ ) with a similar  $C$  value to reach  $\Delta K_{\text{th,conv}}$ .

The crack closure is estimated using the ASTM method from the unloading load-COD curve recorded during the test. The crack closure in this study is estimated at a 4% deviation from the linear load-COD curve. There are different ways to quantify crack closure levels in the crack wake. Here, the effective stress intensity factor over the stress intensity factor is chosen to show crack closure levels and is defined as:

$$U = \left( \frac{K_{\max} - K_{cl}}{K_{\max} - K_{\min}} \right) = \left( \frac{\Delta K_{\text{eff}}}{\Delta K} \right) \quad (5.2)$$

### 5.3 Results

Crack growth rates at  $R = 0.1$  in the 415 and 304L steels are shown in Figure 5.1. At high  $\Delta K$  values, crack growth rates in the 415 steel are lower as compared to the ones in the 304L steel (Figure 5.1); however, as  $\Delta K$  values decrease, crack growth rates in two steels become closer to each other. At a  $\Delta K$  equal to 7.76  $\text{MPa.m}^{1/2}$ , the crack growth rate in both steels becomes equal to  $1.7 \times 10^{-6} \text{ mm/cycle}$ . As the  $\Delta K$  continues to decrease, the crack growth rates in the 415 steel become higher than the 304L steel. Finally, the conventional fatigue threshold,  $\Delta K_{\text{th,conv}}$  corresponding to  $2 \times 10^{-7} \text{ mm/cycle}$  in the 415 steel is lower than the 304L steel, which is 5.2  $\text{MPa.m}^{1/2}$  versus 5.8  $\text{MPa.m}^{1/2}$ , respectively.

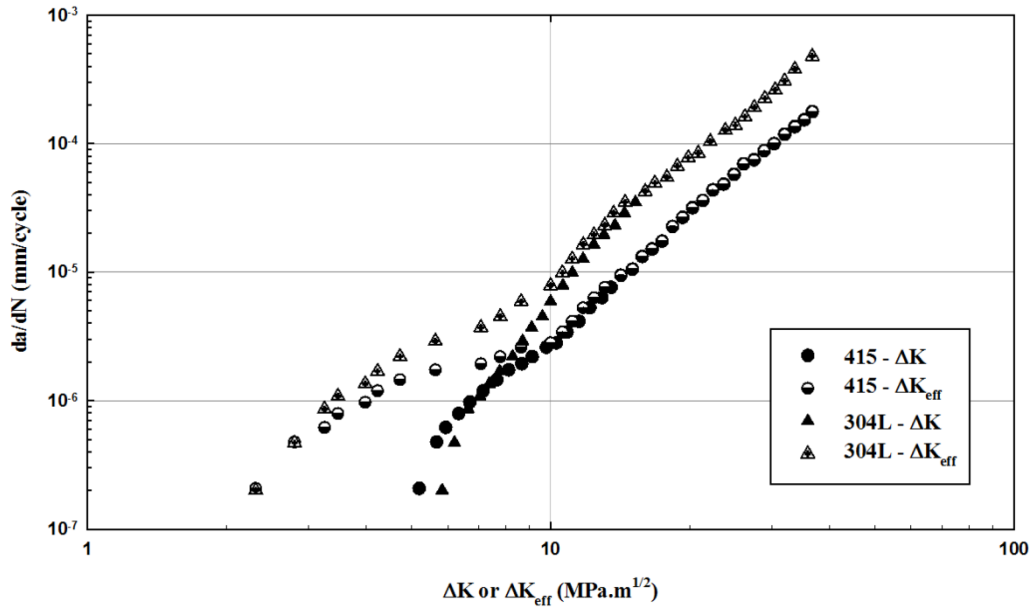


Figure 5.1 Crack growth rates versus  $\Delta K$  and  $\Delta K_{\text{eff}}$  at  $R = 0.1$  in the 415 and 304L steels

Recorded curves show no crack closure at  $\Delta K$  values above  $14.03 \text{ MPa.m}^{1/2}$  in the 415 steel and  $16 \text{ MPa.m}^{1/2}$  in the 304L steel; however, below the aforementioned  $\Delta K$  values, and as the  $\Delta K$  approaches the near-threshold region, the estimated crack closure level increases.

Crack growth rates as a function of  $\Delta K_{\text{eff}}$  are lower in the 415 steel as compared to the ones in the 304L steel. However, as  $\Delta K_{\text{eff}}$  decreases to lower values, the crack growth rates in two steels become closer to each other (Figure 5.1). The estimated crack closure level at the conventional fatigue threshold in both steels is equal to 0.39. As a result, the estimated effective  $\Delta K_{\text{th,conv}}$  corresponding to  $2 \times 10^{-7} \text{ mm/cycle}$  at  $R = 0.1$  in the 415 and 304L steel are equal to  $2.05$  and  $2.30 \text{ MPa.m}^{1/2}$ , respectively. On the other hand,  $\Delta K_{\text{th,conv}}$  at  $R = 0.7$  is equal to  $3.35 \text{ MPa.m}^{1/2}$  and  $3.38 \text{ MPa.m}^{1/2}$  in the 415 and 304L steels, respectively. No crack closure was detected at  $R = 0.7$  in both steels.

As shown in Figure 5.2 and Figure 5.3, the  $\Delta K_{\text{eff}}$  values estimated from the linear load-COD curve at  $R = 0.1$  are compared to the ones at  $R = 0.7$ . Crack growth rates versus  $\Delta K_{\text{eff}}$  at  $R = 0.1$  are higher than the ones at  $R = 0.7$ . The difference increases as crack growth rates decrease towards  $2 \times 10^{-7} \text{ mm/cycle}$ . The effective  $\Delta K_{\text{th,conv}}$  at the fatigue threshold at  $R = 0.1$  is 39% and 32% lower than the one at  $R = 0.7$  in the 415 and 304L steels, respectively.

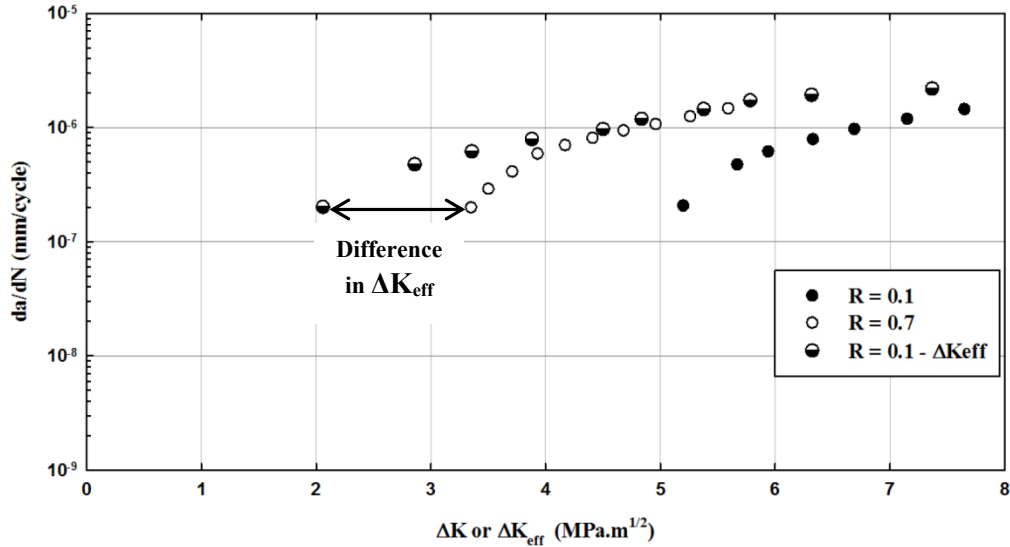


Figure 5.2 Comparison of crack growth rates at  $R = 0.1$  and  $0.7$  in the 415 steel

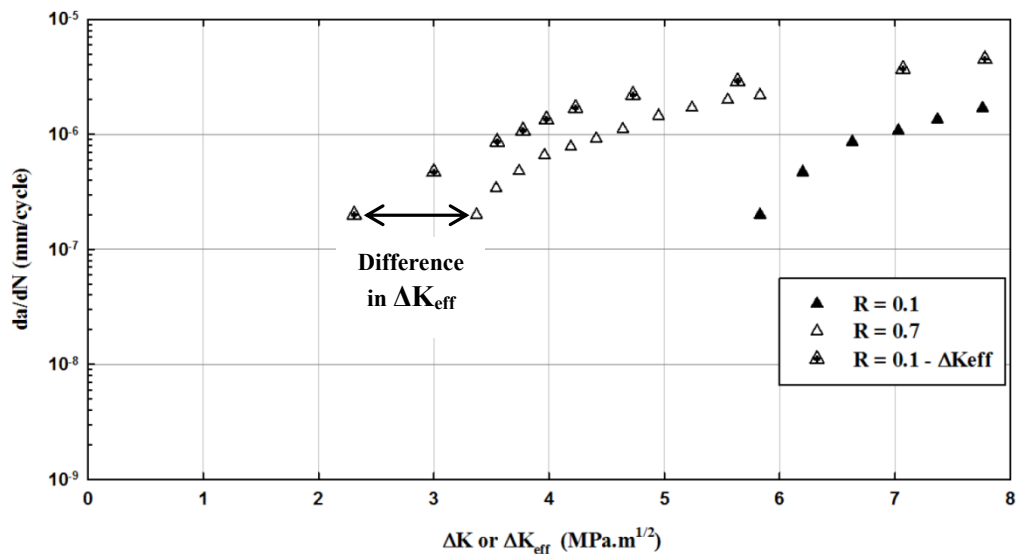


Figure 5.3 Comparison of crack growth rates at  $R = 0.1$  and  $0.7$  in the 304L steel

## 5.4 Discussion

### 5.4.1 Plastic zone size and phase transformation

Sufficient applied deformation transforms the austenite phase to the martensitic phase. This transformation can affect crack growth rates in both steels [55]. In order to quantify this transformation, an X-ray diffraction using Rietveld method was conducted on both steels. The

average volume fraction of reformed austenite in the 415 steel is 17.7% with a standard deviation of  $\pm 2.9$  %. The austenite phase in the 304L steel has a volume fraction equal to  $98 \pm 0.1$  %.

The plastic strain is high within the crack tip and cyclic plastic zone size. Therefore, it was reported that the austenite phase is completely transformed to the martensite phase within this zone [166]; however, the strain further away from the cyclic plastic zone is lower; thus, the austenite is partially transformed to the martensite [51]. The monotonous plastic zone around the crack tip corresponds to the monotonic behavior of the steel during the tensile test.

The 415 and 304L tensile specimens in L and T directions were cut close to the necking section, and subsequently polished and etched. X-ray diffraction analysis revealed that 82% of the existing austenite was transformed to martensite in the 415 steel, this was 63% in the case of 304L steel. The transformation of the austenite to the martensite is only visible with the optical microscope in the 304L steel. It can be seen that the existent austenite in the LS orientation (Figure 5.4a) is partially transformed to a microstructure similar to the martensite (Figure 5.4b).

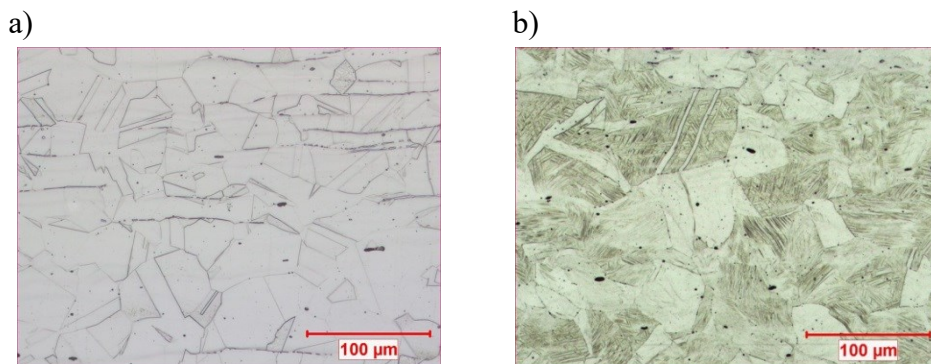


Figure 5.4 Microstructure of the 304L in the LS orientation, a) as received, b) close to the necking of the tensile specimen (L direction)

Cyclic and monotonous plastic zone sizes are much smaller in the 415 steel as compared to the 304L steel. Therefore, there are smaller plastic zone sizes with smaller austenite transformation in the 415 steel. As a result, the crack closure induced by plasticity and phase transformation (plasticity-induced crack closure) in this steel is much lower than the 304L steel. The lower crack growth rate under constant amplitude loading in the 415 steel as compared to the 304L steel may be due to lower plastic zone sizes and lower amount of the austenite transformation of 415 in the Paris region.

### 5.4.2 Crack path irregularities

The crack angle and length deflection are much higher in the 415 steel (Figure 5.6) as compared to the 304L steel (Figure 5.6). Therefore, crack closure is mainly induced by surface asperities in the 415 (roughness-induced crack closure) steel and is higher than the one in the 304L steel.

In the 415 steel, analysis of the recorded P-COD curves at both R ratios shows crack closure at  $R = 0.1$  but not at  $R = 0.7$ ; however, the crack angle and length deflection at  $\Delta K_{th,conv}$  at  $R = 0.1$  and  $0.7$  are similar in the 415 steel (Figure 5.5a and b).

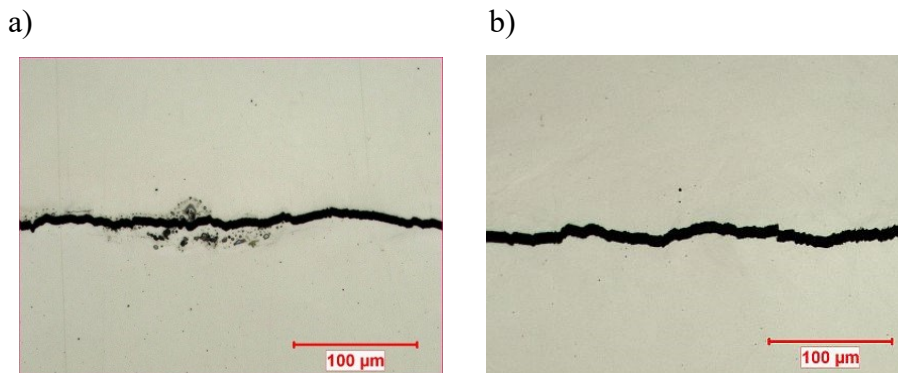


Figure 5.5 Crack path on the surface of the specimen at  $\Delta K_{th,conv}$  in the 415 steel at, a)  $R = 0.1$ , and b)  $R = 0.7$

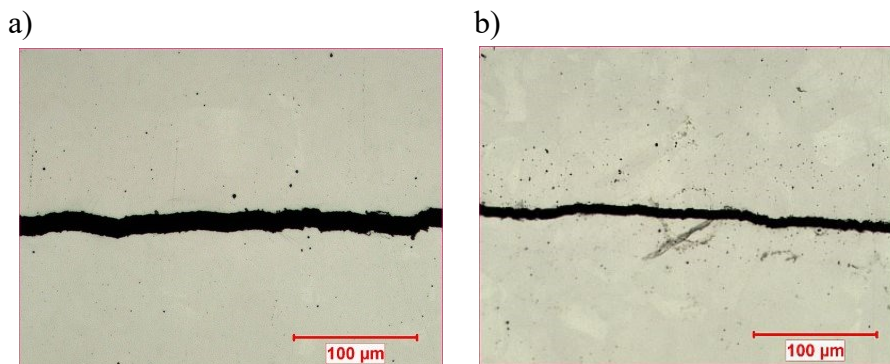


Figure 5.6 Crack path on the surface of the specimen at  $\Delta K_{th,conv}$  in the 304L steel at, a)  $R = 0.1$ , and b)  $R = 0.7$

In order to correlate the effective  $\Delta K_{th,conv}$  at  $R = 0.1$  to the one at  $R = 0.7$ , crack closure is estimated with a higher percentage deviation from the recorded P-COD curve. This method has also been employed in [82, 167]. In this study, a deviation equal to 15% leads to an estimated effective

$\Delta K_{th,conv}$  at  $R = 0.1$  equal to 2.89 and 3.25 MPa.m<sup>1/2</sup> in the 415 and 304L steels, respectively. These values are 13% and 4% lower than the ones at  $R = 0.7$ , respectively.

# CHAPTER 6 ARTICLE 1: EFFECT OF PERIODIC UNDERLOADS ON FATIGUE CRACK GROWTH IN THREE STEELS USED IN HYDRAULIC TURBINE RUNNERS

Published in *International Journal of Fatigue*, Vol. 85, 2016, pp. 40-48

M. Hassanipour<sup>a</sup>, Y. Verreman<sup>a</sup>, J. Lanteigne<sup>b</sup>, J. Q. Chen<sup>a</sup>

<sup>a</sup>Department of Mechanical Engineering, École Polytechnique de Montréal, Montréal, Québec, Canada, H3T 1J4

<sup>b</sup>Institut de Recherche d'Hydro-Québec, Varennes, Québec, Canada, J3X 1S1

## Abstract

The aim of the present work is to study the interaction between two loading cycles in hydraulic turbine runners, i.e. baseline cycles which are the result of power output variations and periodic underloads which correspond to runner start/stop sequences. In order to make better evaluations of fatigue lives, there is a need to determine the real crack growth as compared to those predicted by linear damage summation. This comparison is made for three wrought steels, AISI 415, ASTM A516, and AISI 304L. Fatigue tests were run under both constant amplitude loading and periodic underloads at two constant values of maximum stress intensity factor,  $K_{max}$ . The crack growth under periodic underloads was faster than that predicted by linear damage summation for the A516 and 304L steels, while almost no acceleration was found for the 415 steel. The acceleration factors reached the highest values under low  $K_{max}$  and high load ratio of baseline cycles. High tensile residual stresses and strain hardening at the crack tip caused by underloads contribute to crack growth acceleration during the subsequent baseline cycles.

**Keywords:** Fatigue crack growth; Periodic underloads; Turbine runners steels; Linear damage summation; Interaction factor

Corresponding author. Tel.: (+1) 514 - 9614990.

E-mail address: [meysam.hassanipour@polymtl.ca](mailto:meysam.hassanipour@polymtl.ca)

## Nomenclature

$a$ and $c$	length and width of semi-elliptical defect
$a_{20}$	maximum initial crack length allowed for 20 years design life
$a_{70}$	maximum initial crack length allowed for 70 years design life
$b$ and $t$	runner blade length and thickness
$C_{R0}$ and $p$	Walker equation parameters
$F$ and $Q$	geometric functions for calculating stress intensity factor
$H$	strength coefficient
$\Delta K$	stress intensity factor range
$\Delta K_{BL}$	stress intensity factor range of baseline cycles
$K_{max,OL}$	maximum stress intensity factor of an overload
$\Delta K_{UL}$	stress intensity factor range of an underload
$l$	crack length deflection
$m$	Paris equation exponent
$\Delta N_{BL}$	number of baseline cycles
$\Delta N_{UL}$	number of underload cycles
$q$	number of underload cycles in one block
$n$	frequency of baseline cycles over underload cycles, $\Delta N_{BL}/\Delta N_{UL}$
$R_{BL}$	load ratio of baseline cycles
$R_{UL}$	load ratio of underload cycles
$s$	strain hardening exponent
$W$	compact tension specimen width
$\delta_{UL}$	underload cycle striation width
$\delta_{BL}$	baseline cycle striation width
$\varepsilon$	true strain
$\varepsilon_f$	elongation at fracture
$\theta$	crack deflection angle
$\sigma$	true stress
$\varphi$	angle of a specific point at the front of a semi-elliptical defect
$\Psi$	ratio of stress intensity factor ranges, $\Delta K_{BL}/\Delta K_{UL}$

**Abbreviations**

BL	baseline cycles
C(T)	compact tension specimen
L	longitudinal (rolling) direction of the plate
LT	long transverse orientation
LS	long-short transverse orientation
LDS	linear damage summation
OL	single overload
POV	power output variations
S	short-transverse direction of the plate
SS	start/stop sequences
SIF	stress intensity factor
T	transverse direction of the plate
TS	transverse-short transverse orientation
UL	single underload

## 6.1 Introduction

Critical regions of turbine runners are subjected to a maximum static load followed by small and large amplitude load cycles. On one hand, small amplitude load cycles of very high frequency are generated by blade/wicket gates and rotor/stator interactions. On the other hand, large amplitude load cycles of low frequency are generated by changing the working conditions of the power station, i.e. by start/stop (SS) sequences and power output variations (POV). Additionally, unexpected events can occur and cause runner overspeed (runaway). The load pattern is dependent on both the type of power station and the working conditions [4, 154].

Table 6.1 Typical load pattern for a Francis turbine runner [1]

<b>Cyclic loads</b>	<b>Frequency</b>	<b>Number of cycles (70 years lifetime)</b>	<b>S<sub>max</sub> (MPa)</b>	<b>S<sub>min</sub> (MPa)</b>
<b>Blade/wicket gates interaction</b>	20 per rotation	$6.97 \times 10^{10}$		196
<b>Power output variation (POV)</b>	3 to 5 per day	76 650 to 127 750	200	140 to 100
<b>Start / Stop (SS)</b>	0.5 to 1 per day	12 775 to 25 550		-75
<b>Overspeed (Runaway)</b>	5 per year	350		-200

Defects form in the runners during their fabrication (casting and welding). Throughout the runner operation, when these defects are located at high stress regions, they can propagate, leading to runner failure. To avoid this, elastic finite element models are used to limit maximum local stresses with respect to the material's yield stress by means of a safety factor [4]. Furthermore, linear elastic fracture mechanics with a conservative Paris equation is employed to predict the defect growth. One objective is to determine the maximum allowable initial defect sizes for a given design life, e.g. 70 years. Further information and details can be found in [4, 21, 168-170].

In engineering practice, the crack growth increments produced by different load cycles under constant amplitude loading are linearly summated to predict the crack growth under variable amplitude loading. This prediction method will be termed hereafter as linear damage summation (LDS). However, different studies reported that crack can grow faster or slower than predicted by

linear damage summation [105, 108]. For instance, a single overload (OL) can notably decrease the crack growth rates of the subsequent baseline cycles. A crack can even become non-growing for a certain number of cycles that depends on load parameters such as  $K_{\max,OL}$ ,  $\Delta K_{BL}$  and  $R_{BL}$  (see nomenclature and Figure 6. 1) [115, 171]. Thus, the LDS prediction overestimates crack growth in the case of an overload followed by baseline cycles [172]. The crack growth delay or arrest was mainly ascribed to larger plastic deformation and surface roughness left in the crack wake [45, 59].

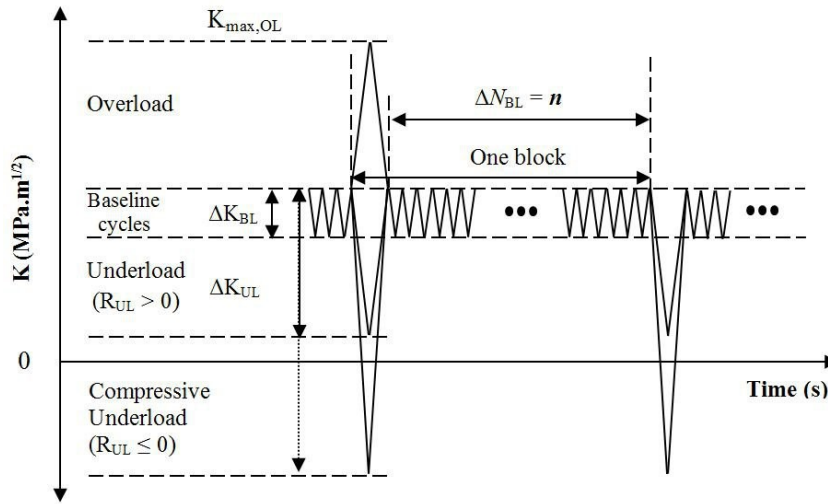


Figure 6. 1 Different load cycles under variable amplitude loading

On the other hand, LDS underestimates the effect of compressive underloads ( $R_{UL} \leq 0$ ) and underloads ( $R_{UL} > 0$ ) [106, 117]. Compressive underloads flatten the crack wake asperities, which propagates a non-growing crack or leads to crack growth acceleration of the baseline cycles. This acceleration depends on  $\Delta K_{UL}$ ,  $\Delta K_{BL}$  and  $R_{BL}$  parameters. However, as the crack grows, the asperities are rebuilt in the crack wake, so progressive deceleration and crack arrest can occur again [135]. The simple underload or the compressive underload must be applied periodically in order to reduce the fatigue threshold [120, 128].

For simplicity, baseline cycles intercut with periodic underload cycles will be termed hereafter as periodic underloads. The predicted crack growth in one block using LDS for a certain number of underload cycles ( $\Delta N_{UL}$ ) and for baseline cycles ( $\Delta N_{BL}$ ) is given by the following equation [173]:

$$(\Delta a)_{LDS} = (\Delta a)_{UL} \Delta N_{UL} + (\Delta a)_{BL} \Delta N_{BL} \quad (6.1)$$

The frequency of baseline cycles over underload cycles  $\Delta N_{BL}/\Delta N_{UL}$  ratio is defined as  $n$ , hereafter. As shown in Figure 6. 1, in the case of  $\Delta N_{UL} = 1$ ,  $\Delta N_{BL}$  becomes equal to  $n$ . The measured crack

growth per block  $(\Delta a)_{\text{measured}}$  is compared to the predicted one  $(\Delta a)_{\text{LDS}}$ . An interaction factor is defined as the  $(\Delta a)_{\text{measured}} / (\Delta a)_{\text{LDS}}$  ratio. When the ratio is higher than unity, it is an acceleration factor; otherwise it is a retardation factor.

No interaction was found in a titanium alloy between periodic underloads ( $R_{\text{UL}} = 0.1$ ) and baseline cycles ( $R_{\text{BL}} = 0.75$  to  $0.90$ ) for  $n = 10^3$  to  $10^5$  [174]. However, it was shown that as the underloads are applied more frequently, the acceleration factor increases [95, 117]. These factors reached values up to two in the Paris region [116, 117]. As high R ratios were employed ( $R_{\text{UL}} = 0.5$  and  $R_{\text{BL}} = 0.75$  to  $0.85$ ) the maximum acceleration factor of a given material is obtained for a particular combination of  $\Delta K_{\text{BL}}/\Delta K_{\text{UL}}$  ( $\psi$ ) and  $\Delta N_{\text{BL}}/\Delta N_{\text{UL}}$  ( $n$ ) [116]. The effect was higher for a structural steel as compared to an aluminum alloy.

Little information is available about physical mechanisms responsible for the crack growth acceleration. In one study, after applying compressive underloads, a local measurement ahead of the crack tip revealed a negative strain [120]. It was argued that this negative local strain favors the crack tip to open at lower stress levels and leads to higher crack growth rate during of subsequent baseline cycles. These lower stress opening levels are associated with tensile residual stress at the crack tip. In the case of periodic underloads, it was also argued that the crack tip is periodically squeezed and subjected to a tensile residual stress [175]. This stress decreases during the subsequent baseline cycles until it reaches a steady state

Strain hardening can also explain the crack growth accelerations. Monotonically pre-strained specimens ( $\epsilon = +3\%$ ) made of aluminum alloy 2024-T351 and tested at  $R = 0.1$  showed 50% crack growth acceleration with respect to unstrained specimens made of the same material [125]. Crack growth acceleration was also observed for the titanium alloy 6Al-4V in similar circumstances [126]. It was concluded that the strain hardening tends to decrease the ductility at the crack tip, leading to an increase in crack growth rates.

Fractography analyses in the literature have shown that overloads and irregular loadings can modify the striation spacings of the subsequent baseline cycles [176, 177]. In the case of periodic underloads, baseline cycles striation spacings were not modified and it was concluded that the acceleration effect occurs during the underloads [117]. However, other studies concluded that the acceleration occurs during the crack growth of baseline cycles [116, 178].

A limited number of studies have been performed on fatigue of turbine runners under variable amplitude loading [155, 179]. The critical crack dimensions in turbine runners are reached when the small cycles SIF range becomes equal to the fatigue threshold [155, 179, 180]. However, during most of the fatigue life, the stress range of the small cycles (4 MPa; Table 6.1) induces a much lower stress intensity factor range as compared to the fatigue threshold. Small cycles can be neglected in the case of recently built runners where their amplitude does not exceed a few MPa.

In the present experimental work, we investigate the interaction effect between two large load cycles, i.e. POV and SS sequences at constant  $K_{\max}$  values. The same load spectrum was imposed on three steels of different microstructures (AISI 415, ASTM A516, and AISI 304L). The experimentally measured crack growths are compared to the ones predicted by LDS. The factors leading to the differences between measured and predicted crack growths are discussed.

## 6.2 Materials

### 6.2.1 Chemical compositions and heat treatments

The contents of carbon (C), phosphorus (P) and nitrogen (N) were measured by the combustion and fusion technics [159]. The contents of other elements including chrome (Cr) were measured using the inductively coupled plasma mass spectrometry [181]. The chemical compositions for each steel are given in Table 6.2. AISI 415 is a martensitic stainless steel, which is solution annealed at 1000 °C, then water quenched and tempered at 600°C. ASTM A516 is a ferritic-pearlitic steel, which is hot rolled and slowly cooled at room temperature. AISI 304L is an austenitic stainless steel, which is hot rolled and annealed. The cast versions of the three steels (CA6NM, A27, and CF3, respectively) are often used in runner fabrication. The wrought versions of these steels were chosen in order to have less dispersion in the results. In the following sections, the wrought steels are referred as 415, A516 and 304L, respectively.

Table 6.2 Chemical compositions of studied materials (wt. %)

Steels	C	Cr	Ni	Mn	P	S	Si	Mo	N	Cu
<b>415</b>	0.026	13.02	3.910	0.740	0.021	0.001	0.345	0.560	0.031	-
<b>A516</b>	0.200	0.060	0.020	0.770	-	0.014	0.025	<0.010	-	0.060
<b>304L</b>	0.027	17.80	8.330	2.000	0.026	0.011	0.300	0.296	0.080	0.360

### 6.2.2 Microstructural characterization and tensile properties

After standard polishing down to 1  $\mu\text{m}$  diamond paste, the microstructures of three steels were revealed by different etching techniques. The 415 steel was etched using modified Fry's (0.5 g  $\text{CuCl}_2$ , 25 ml  $\text{HCl}$ , 25 ml  $\text{HNO}_3$ , 75 ml  $\text{H}_2\text{O}$ ) followed by Villela's reagents to reveal the prior austenitic grain boundaries and the martensitic laths, respectively, as shown in Figure 6.2a. The second phase in this steel is reformed austenite, which was formed during tempering. In order to measure the volume fraction of this phase, the samples were acid thinned (75 ml  $\text{HCl}$ , 75 ml  $\text{HNO}_3$  and 100 ml  $\text{H}_2\text{O}$ ) to remove the induced deformation during the polishing. Afterwards, an X-ray diffraction analysis was conducted using  $\text{Cu K}_\alpha$  source radiation with 0.05 degree per 4 seconds for angles  $2\theta$  from  $40^\circ$  to  $140^\circ$  using the Rietveld method [182] with an accuracy of  $\pm 1.5\%$ . It revealed that the average volume fraction of reformed austenite on the three orthogonal planes is 17.7% with a standard deviation of  $\pm 2.9\%$ .

The A516 steel was etched using Nital 3% to reveal the ferritic-pearlitic microstructure (Figure 6.2b). The pearlite fraction was estimated on the three orthogonal planes using an optical microscope and image analysis software. The average value is  $24.4\% \pm 0.4\%$ , which is close to the fraction estimated by the Iron-Carbon phase diagram for this steel [183]. As seen in Figure 6.2b, the pearlite bands appear on the LS and TS planes, but pearlite is dispersed on the LT planes.

The 304L steel was electro-etched at 6 V direct current using aqueous oxalic acid 10% to reveal austenitic grain boundaries (see Figure 6.2c). A low volume fraction of delta ferrite (around 2%) was measured using a ferrite detector.

Ten Vickers microhardness measurements were carried out on the three orthogonal planes of each steel with a force of 100 gf and a 15 s dwell time according to ASTM E384 [184]. The microhardness of the 415 steel is the highest with an average of  $298 \pm 6$  HV. The 304L and A516 steels have lower values of  $176 \pm 8$  HV and  $146 \pm 13$  HV, respectively.

The prior austenite grain sizes on each plane were measured using an optical microscope and an image analysis software according to ASTM E1382 [185]. The results with their standard deviations are given in Table 6.3.

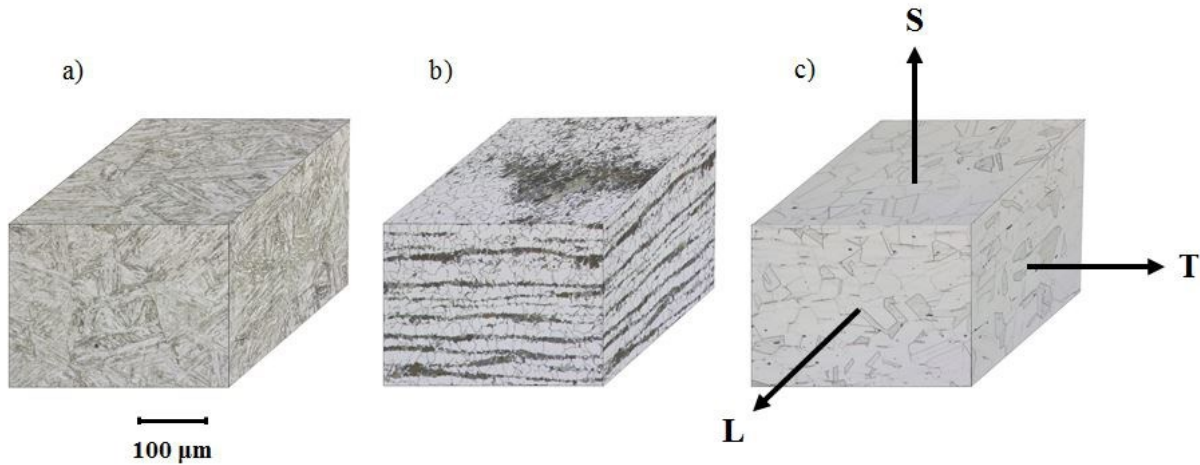


Figure 6.2 Microstructure of the three wrought steels, a) 415, b) A516, and c) 304L

Table 6.3 Average prior austenite grain size on the three orthogonal planes of each steel ( $\mu\text{m}$ )

Steels	LT	LS	TS
<b>415</b>	105 $\pm$ 44	95 $\pm$ 46	96 $\pm$ 45
<b>A516</b>	20 $\pm$ 10	16 $\pm$ 7	16 $\pm$ 7
<b>304L</b>	58 $\pm$ 17	52 $\pm$ 18	52 $\pm$ 15

Three tensile tests in L and T directions were performed at a nominal strain rate of  $2.5 \times 10^{-4} \text{ s}^{-1}$  at room temperature according to ASTM E8M (25 mm gauge length and 5 mm specimen diameter) [158]. The tensile properties for each steel and orientation are given in Table 6.4. The strain hardening exponents ( $s$ ) are those of the Hollomon's equation ( $\sigma = H\varepsilon^s$ ), where  $\sigma$  and  $\varepsilon$  are the true stress and strain, and  $H$  is the strength coefficient [97].

All steels show a quasi-isotropic behavior in L and T directions. A low dispersion in each direction is obtained for the 415 and A516 steels. The 304L steel shows more dispersion for the yield stress in T direction as compared to L direction. The 415 steel has an almost perfectly plastic behavior with a low strain hardening exponent. The A516 steel has higher strain hardening capacity as compared to the 415 steel. On the other hand, the 304L steel has the highest strain hardening.

Table 6.4 Tensile properties of the three wrought steels in L and T directions at room temperature

Steels	0.2% yield strength (MPa)	Ultimate tensile strength (MPa)	Elongation at rupture ( $\epsilon_r$ )	Strain hardening exponent ( $s$ )
415 (L)	725 $\pm$ 0	843 $\pm$ 4	0.21 $\pm$ 0.01	0.09
415 (T)	705 $\pm$ 9	835 $\pm$ 6	0.19 $\pm$ 0.01	0.09
A516 (L)	300 $\pm$ 3	476 $\pm$ 5	0.37 $\pm$ 0.02	0.29
A516 (T)	301 $\pm$ 3	480 $\pm$ 5	0.36 $\pm$ 0.01	0.29
304L (L)	261 $\pm$ 0	704 $\pm$ 9	0.65 $\pm$ 0.04	0.60
304L (T)	283 $\pm$ 24	702 $\pm$ 10	0.69 $\pm$ 0.08	0.59

## 6.3 Experimental procedures

### 6.3.1 Loading parameters

The initial semi-elliptical defect dimensions ( $a \times 2c$ ) that correspond to final fatigue fracture of a blade runner after 20 and 70 years were estimated [154]. They are given in Table 6.5. The selected values for the runner blade thickness and length ( $t \times b$ ) are 50 and 2000 mm, respectively. Considering the maximum static stress of 200 MPa (Table 6.1) plus a typical tensile residual stress of 100 MPa after tempering [186, 187], the maximum stress intensity factors are calculated based on the following equation [188]:

$$K_{\max} = S_{\max} \sqrt{\frac{\pi a}{Q}} F\left(\frac{a}{t}, \frac{a}{c}, \frac{c}{b}, \phi\right) \quad Q = 1 + 1.464 \left(\frac{a}{c}\right)^{1.65} \quad (6.2)$$

where  $\phi$  is the angle of a point on the front of the semi-elliptical defect, and  $F$  and  $Q$  are geometric functions that are given in [188]. The defect dimensions, the maximum nominal stress, and the corresponding  $K_{\max}$  values are given in Table 6.5. The two  $K_{\max}$  values will be named hereafter as  $K_{\max,20}$  and  $K_{\max,70}$ .

Table 6.5 Maximum SIF at the tip of initial defects corresponding to runner lifetimes of 20 and 70 years

Lifetime	Defect dimensions ( $a \times 2c$ ) (mm)	$S_{\max}$ (MPa)	$K_{\max}$ (MPa.m <sup>1/2</sup> )
20 years	8 × 28	300	40.77
70 years	2.5 × 6		19.43

The R ratios chosen for baseline cycles (POV) and underloads sequences (SS), and the corresponding ratios of SIF ranges,  $\Psi$  are given in Table 6.6. The selected frequency ratios,  $n$ , correspond to the minimum and maximum ratios of POV and SS sequences. These selected values are typical of the working conditions of a power station [4, 154].

Table 6.6 Loading parameters for POV and SS sequences

	Load cycles	Frequency	$\Delta N_{BL}/\Delta N_{UL}$ ( $n$ )	R	$\Delta K_{BL}/\Delta K_{UL}$ ( $\Psi$ )
POV	Baseline	3 to 5 per day	3 and 10	0.3, 0.5, 0.7	0.78, 0.55, 0.33
	cycles				
SS	Underloads	0.5 to 1 per day		0.1	

As a summary, for each steel, crack growth rates will be measured at two  $K_{\max}$  values, two frequency ratios,  $n$ , and three  $\Psi$  ratios ( $\Delta K_{UL}$  corresponds to 0.9  $K_{\max}$  in all cases).

### 6.3.2 Fatigue testing

Fatigue crack growth tests were performed using a closed loop Instron servo-hydraulic machine equipped with a 100 kN dynamic load cell. Compact tension, C(T), specimens were tested in LT orientation according to ASTM E647 [160]. The width and thickness of the specimens are 50.8 mm and 12.7 mm, respectively. Atmospheric conditions were periodically recorded with a thermo-hygrometer. The test temperature was stable at 23°C while relative humidity varied between 40 % and 45 %.

The three steels were tested at  $K_{\max,20}$  and  $K_{\max,70}$  under constant amplitude loading and under periodic underloads. In order to minimize the results scatter from one specimen to another, the same specimen was used to generate all the data at each  $K_{\max}$ . Tests at constant  $K_{\max}$  give a direct evaluation of load interactions under periodic underloads as compared to constant load tests [107].

As shown in Figure 6.3, tests were conducted on each specimen under constant amplitude loading between 0.25 and 0.45  $a/W$  then under periodic underloads between 0.45 and 0.65  $a/W$  ( $W$  is the specimen width).

The crack growth rates under constant amplitude loading were measured at four different  $R$  ratios ( $R = 0.1, 0.3, 0.5,$  and  $0.7$ ) by varying the SIF range. A large number of cycles can be elapsed at  $R = 0.1$  to reach a stable crack growth rate at  $R = 0.7$  and vice versa. In order to minimize these transitory cycles, the  $R$  ratios were varied step by step in the load sequence. In order to verify the crack length effect on crack growth rates, the load sequence is carried out in decreasing steps followed by increasing ones as shown in Figure 6.3a. The crack growth rates were measured optically using the secant method at both 1 Hz and 10 Hz. Three stable values of crack growth rate were recorded.

Periodic underloads tests were performed at constant  $K_{\max}$  for six different loading blocks (two  $n$  values at three  $\Psi$  ratios) as shown in Figure 6.3b. All tests were conducted at 1 Hz in order not to have any overshoot in the load signal response. For each load block, three stable crack growth rates were measured optically using the secant method.

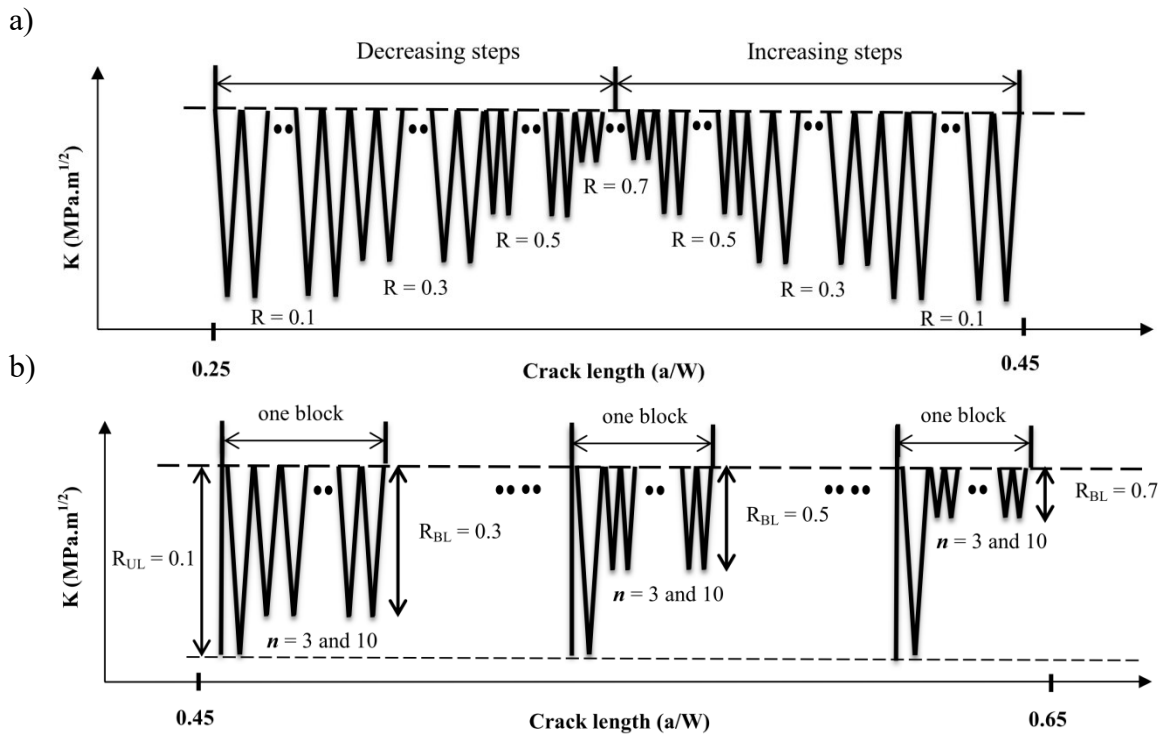


Figure 6.3 Applied loading sequence on the three steels at constant  $K_{\max}$ ,

a) under constant amplitude loading, b) under periodic underloads

## 6.4 Results

### 6.4.1 Constant amplitude loading

Crack length effects are small for all steels. The most important one occurs at  $R = 0.1$  and  $K_{\max,20}$ . In the 415 steel the crack growth rate is only 1% higher at the beginning of the loading sequence ( $a/W = 0.25$ ) than at the end of the sequence ( $a/W = 0.45$ ; Figure 6.3a). Similar trends are observed for A516 and 304L steels but the relative differences are larger, about 4% and 7% respectively.

Frequency effects (1 Hz versus 10 Hz) on crack growth rates are very small in the 415 and 304L steels. On the other hand, at  $R = 0.1$ , the A516 steel shows 5% higher crack growth rates at 1 Hz as compared to 10 Hz. More important chemical activities such as oxidation at the crack tip may increase the crack growth rates in the Paris region.

The 415 steel shows the lowest crack growth rates at all  $R$  ratios and both  $K_{\max}$  (Figures 6.6 and 5.7). On the other hand, the 304L steel has the highest rates. Intermediate values are obtained for the A516 steel.

The crack opening displacement was measured using a clip gauge installed at the mouth of the specimen. The load-displacement loops were analyzed after the test in order to evaluate the crack closure levels using a 2% compliance offset criterion according to ASTM E647-11 [160]. At the applied  $K_{\max}$  levels in this study, the crack closure was negligible for all steels at all  $R$  ratios.

In order to put into evidence the local crack path irregularities in the three steels, fracture surfaces were cut in the middle of the specimen, then polished down to 1  $\mu\text{m}$  diamond and etched as explained in section 2.2. The crack deflection angles ( $\theta$ ) and crack deflection lengths ( $l$ ) were measured as shown in Figure 6.4.

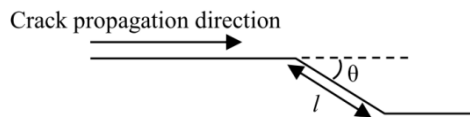


Figure 6.4 Schematic of crack deflection angle ( $\theta$ ) and crack deflection length ( $l$ )

As shown in Figure 6.5a, the 415 steel shows the largest angles and lengths of crack deflections, i.e.  $22.8^\circ \pm 6.0^\circ$  and  $81.6 \mu\text{m} \pm 30.1 \mu\text{m}$ , respectively. Lower values were measured in the A516 steel with  $18.0^\circ \pm 6.1^\circ$  and  $26.7 \mu\text{m} \pm 9.5 \mu\text{m}$ , and some crack branching were observed (see Figure

6.5b). However, the 304L steel shows a quasi-straight crack path (Figure 6.5c). The crack deflection angle is equal to  $7.3^\circ \pm 0.8^\circ$  and the crack deflection length is equal to  $35.2 \mu\text{m} \pm 6.6 \mu\text{m}$ .

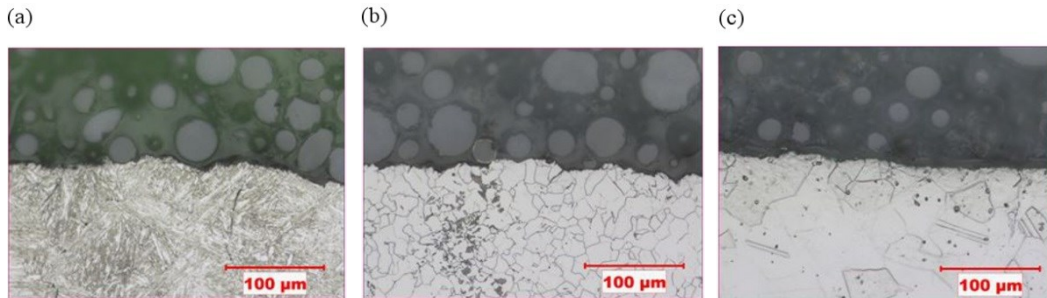


Figure 6.5 Crack path deflection under constant amplitude loading at  $K_{\max,70}$  and  $R = 0.1$  in the a) 415 steel, b) A516 steel, and c) 304L steel (crack propagates from left to right in the three cases)

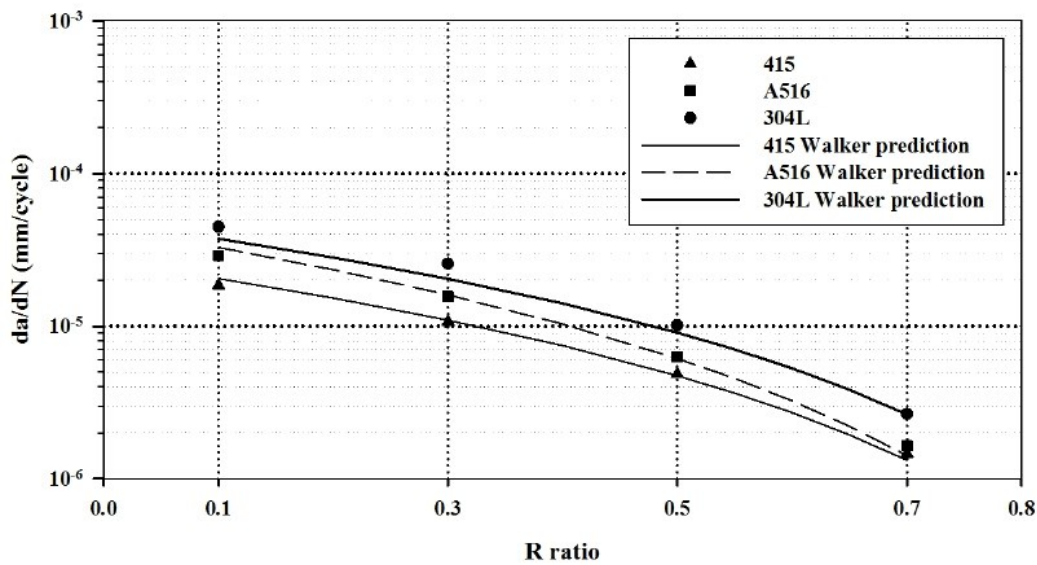


Figure 6.6 Crack growth rates versus load ratio and corresponding Walker predictions at  $K_{max,70}$

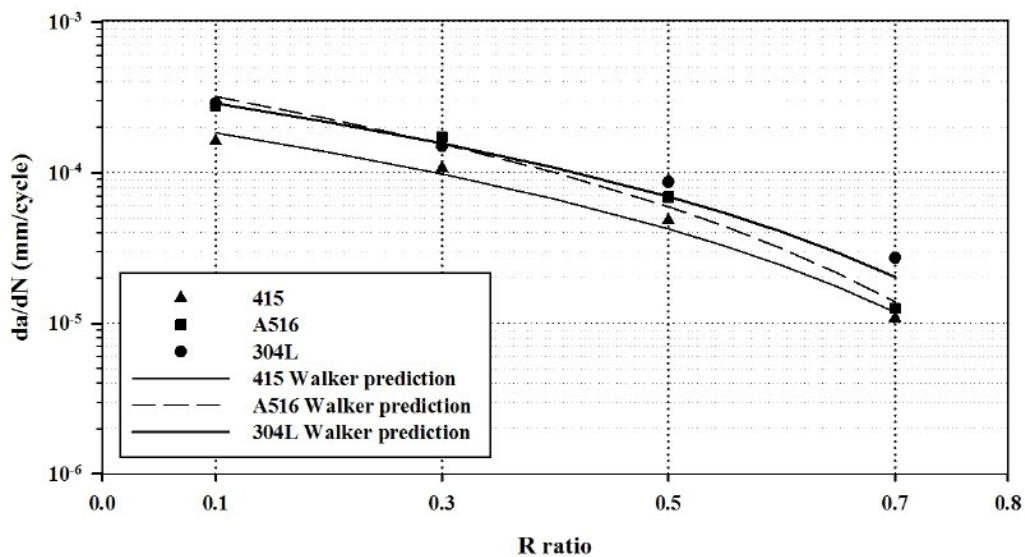


Figure 6.7 Crack growth rates versus load ratio and corresponding Walker predictions at  $K_{max,20}$

For each steel and each R ratio, a straight line can be drawn in a  $da/dN$ - $\Delta K$  log-log plot knowing the crack growth rates at  $K_{max,20}$  and  $K_{max,70}$ . This gives the  $C_R$  and  $m_R$  values of the Paris equation ( $da/dN = C_R (\Delta K)^{m_R}$ ) corresponding to each load ratio. In order to take the R ratio effect into account, the Walker equation is employed,

$$\frac{da}{dN} = C_{R0} \frac{\Delta K^m}{(1-R)^p} \quad (6.3)$$

where the exponent  $m$  is the arithmetic average of the four  $m_R$  values. The  $C_{R0}$  and  $p$  parameters are derived from a linear regression of data points in a  $\log C_R - \log (1-R)$  plot [22]. The three parameters of the Walker equation are given in Table 6.7 for each steel. The crack growth rates predicted by the Walker equation are compared to the measured ones at both  $K_{\max}$  in Figures 6.6 and 5.7. The root mean square of the relative errors is calculated at both  $K_{\max}$ . The mean error is higher at  $K_{\max,20}$ ; it is equal to 11%, 12% and 16% for the 415, the A516 and the 304L steels, respectively.

Table 6.7 Parameters of Walker equation for each steel

Steels	$m$	$C_{R0}$	$p$
<b>415</b>	2.96	$4.08 \times 10^{-9}$	0.46
<b>A516</b>	3.07	$4.92 \times 10^{-9}$	0.21
<b>304L</b>	2.75	$1.38 \times 10^{-8}$	0.34

The fatigue striations under constant amplitude loading are not clearly visible for any steel at  $K_{\max,70}$  even at  $R = 0.1$ . However, they are visible at  $K_{\max,20}$  and  $R = 0.1$  on the fatigue surfaces of the 415 and A516 steels (Figure 6.8a and b) and well defined on those of the 304L steel (Figure 6.8c). The striation spacing for the 415 steel is equal to  $0.510 \pm 0.03 \mu\text{m/striation}$  and is larger than the macroscopic crack growth rate, equal to  $0.161 \pm 0.02 \mu\text{m/cycle}$  (see Figure 6.8). The striation spacings for the A516 and 304L steels are equal to  $0.405 \pm 0.07$  and  $0.497 \pm 0.05 \mu\text{m/striation}$ , respectively, and are closer to the macroscopic growth rates, equal to  $0.277 \pm 0.02$  and  $0.285 \pm 0.03 \mu\text{m/cycle}$ , respectively. As the load ratio increases towards 0.7, striations become no more visible for the 415 and A516 steels but are still visible for the 304L steel (Figure 6.8d).

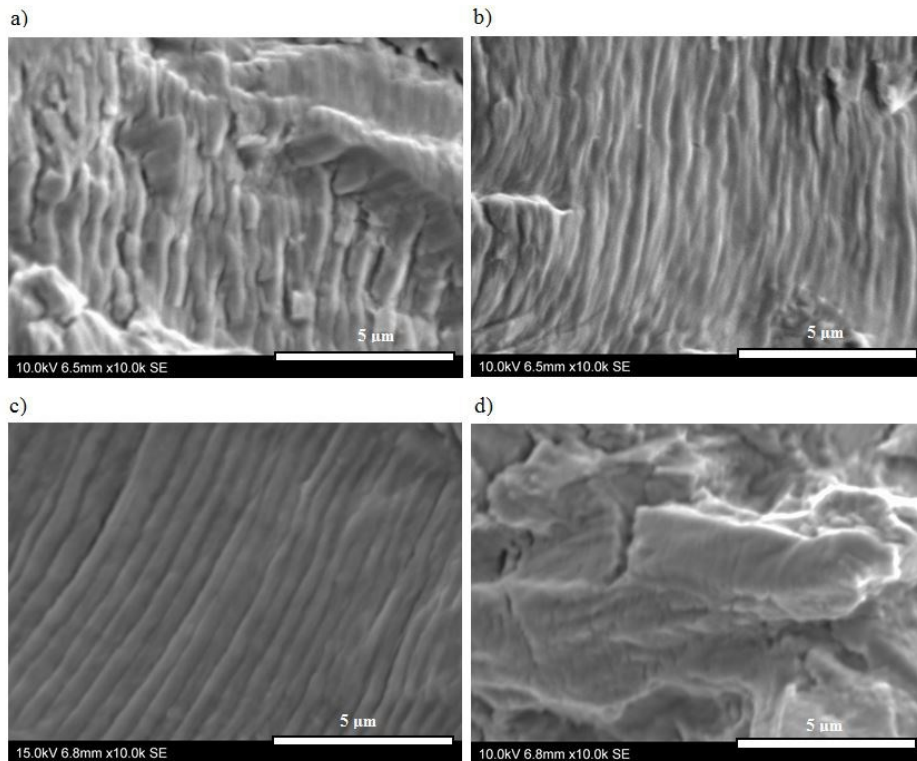


Figure 6.8 Fatigue striations on fatigue surfaces under constant amplitude loading at  $K_{\max,20}$ , (a) 415 steel at  $R = 0.1$ , (b) A516 steel at  $R = 0.1$ , (c) 304L steel at  $R = 0.1$ , and (d) 304L steel at  $R = 0.7$  (crack propagates from left to right in all cases)

### 6.4.2 Periodic underloads

As described in Figure 6.3(b), after constant amplitude load sequences, underloads were periodically applied after 3 and 10 baseline cycles at three  $R$  ratios ( $R_{BL} = 0.3, 0.5$  and  $0.7$ ). Crack growth rates were measured for each loading block at  $K_{\max,20}$  and  $K_{\max,70}$ . They were always larger than those predicted using the LDS method (equation 1). The maximum acceleration factors generally occur when  $R_{BL} = 0.7$ . They are listed in Table 6.8 for both  $K_{\max}$  and  $n$ . The highest acceleration factors were obtained for the 304L steel (up to 2.53) and the lowest for the 415 steel (close to unity).

For all steels the acceleration factors are lower at  $K_{\max,20}$  as compared to  $K_{\max,70}$ . This is in agreement with other results which showed higher acceleration factors at lower  $K_{\max}$  [116]. Further, the acceleration factors obtained at  $n = 3$  are lower than at  $n = 10$  for all steels (e.g., 2.28 versus 2.53 for the 304L steel).

Table 6.8 Maximum acceleration factors for the three steels at both  $K_{\max}$  and  $n$ 

Steels	$K_{\max,70}$		$K_{\max,20}$	
	$n = 3$	$n = 10$	$n = 3$	$n = 10$
<b>415</b>	1.11	1.35	1	1.14
<b>A516</b>	1.39	1.71	1.25	1.46
<b>304L</b>	2.28	2.53	1.73	1.79

LDS exactly predicts crack growth when  $\Delta K_{BL}$  tends to the  $\Delta K_{UL}$ , i.e. the acceleration factor is equal to 1 when  $\Psi = \Delta K_{BL}/\Delta K_{UL} = 1$  ( $R_{BL} = 0.1$ ). However, as the  $\Delta K_{BL}$  and  $\Psi$  decreases ( $R_{BL}$  increases), the acceleration factors increase (Figures 6.9 and 6.10). At both  $K_{\max}$ , the maximum value is reached at  $\Psi = 0.33$  ( $R_{BL} = 0.7$ ) for 415 and A516 steels. However, this is not the case for the 304L steel. The maximum is at  $\Psi = 0.55$  ( $R_{BL} = 0.5$ ) at  $K_{\max,70}$  (Figure 6.9) and there is nearly the same acceleration factor for all  $\Psi$  values at  $K_{\max,20}$  (Figure 6.10).

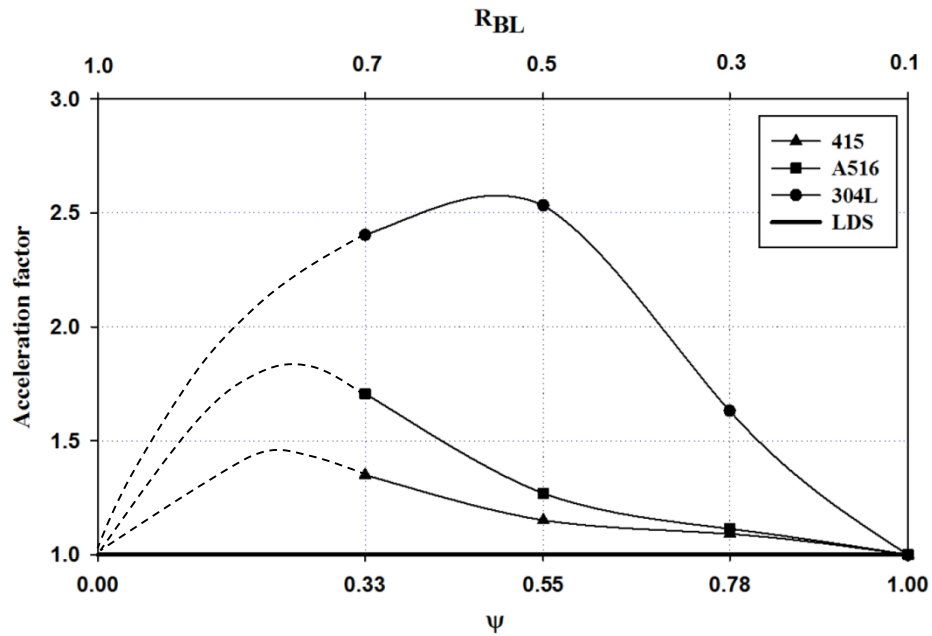


Figure 6.9 Acceleration factors for the three steels at  $K_{\max,70}$  and  $n = 10$  (curves are obtained from a third order polynomial regression of the data)

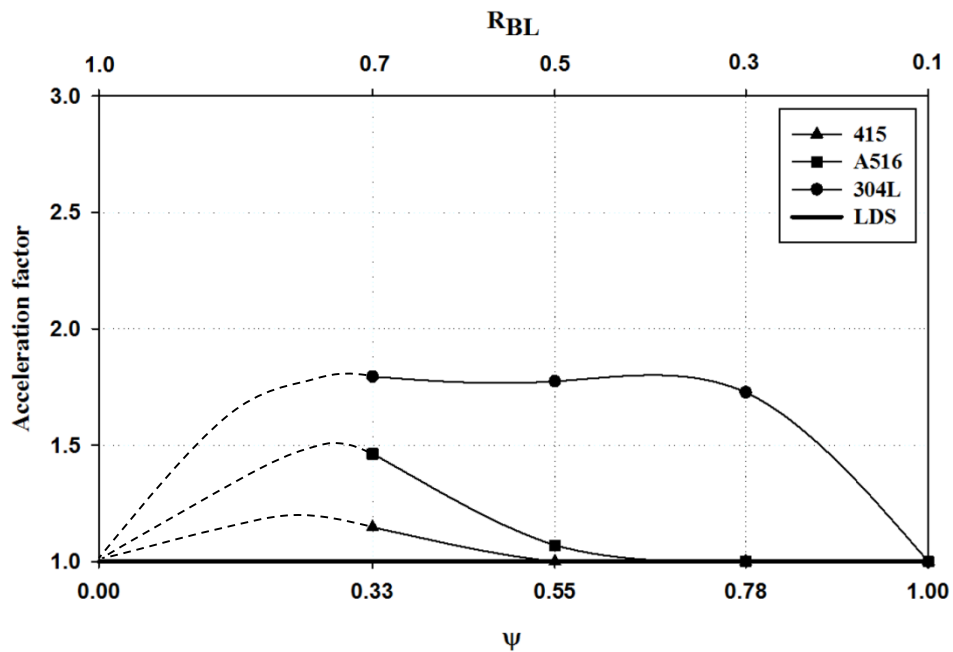


Figure 6.10 Acceleration factors for the three steels at  $K_{\max,20}$  and  $n = 10$  (curves are obtained from a third order polynomial regression of the data)

The root mean square of the SIF ranges ( $\Delta K_{\text{rms}}$ ) was also proposed to predict crack growth under irregular load spectrums [189]. It is given by the following equation:

$$\Delta K_{rms} = \sqrt{\frac{\sum_{i=1}^q (\Delta K_i)^2}{q}} \quad (6.4)$$

where  $q$  is the total number of cycles in one load block. In the present study, the equation 4 reduces to

$$1 - R_{rms} = \frac{\Delta K_{rms}}{K_{max}} = \sqrt{\frac{(1 - R_{UL})^2 + n(1 - R_{BL})^2}{n + 1}} \quad (6.5)$$

Selecting  $R_{UL} = 0.1$ ,  $R_{BL} = 0.7$  and  $n = 10$ , equation 5 gives an equivalent  $R_{rms}$  ratio equal to 0.6. The two prediction methods based on LDS and  $\Delta K_{rms}$  are compared in Table 6.9 with the measured crack growth at  $K_{max,70}$ ,  $\Psi = 0.33$  and  $n = 10$  (these conditions correspond to the highest acceleration factors). Both methods are non-conservative since they underestimate the measured crack growth rates. The method based on  $\Delta K_{rms}$  results in a larger acceleration factor than that based on LDS. The two last columns of Table 6.9 give a comparison with crack growth under constant amplitude loading at  $R = 0.7$  and  $0.5$ . The crack growth at  $R = 0.7$  gives the worst prediction. On the other hand, the measured crack growths under constant amplitude loading at  $R = 0.5$  are close to those measured under periodic underloads. This means that the load block with periodic underloads can be substituted by a load block of constant amplitude loading with an equivalent  $R$  ratio that is lower than that given by equation 5 ( $R_{rms}$ ).

Table 6.9 Comparison of measured crack growth with different prediction methods for the three steels (acceleration factors are calculated at  $K_{max,70}$ ,  $\Psi = 0.33$  and  $n = 10$ )

Steels	$\Delta a   \Psi = 0.33$	$\Delta a   \Psi = 0.33$	$\Delta a   \Psi = 0.33$	$\Delta a   \Psi = 0.33$	$\Delta a   \Psi = 0.33$
	(mm/block)	$\Delta a  _{LDS}$	$\Delta a  _{\Delta K_{rms}}$	$\Delta a  _{R=0.7}$	$\Delta a  _{R=0.5}$
<b>415</b>	$4.86 \times 10^{-5}$	1.35	1.56	3.03	0.91
<b>A516</b>	$7.76 \times 10^{-5}$	1.71	1.92	4.32	1.12
<b>304L</b>	$1.72 \times 10^{-4}$	2.41	3.45	5.87	1.54

## 6.5 Discussion

As the crack tip interacts locally with the microstructure, the crack can deflect and branch. This results in a reduction of the effective stress intensity factor and crack growth rate [190]. In other words a deflected crack requires more elapsed cycles to grow along a certain distance as compared to a quasi-straight crack. However, this deceleration can be outweighed by a preferential microstructural path followed by the crack tip [75]. The crack growth rates were the highest for the 304L steel under constant amplitude loading. The quasi-straight crack path observed in the 304L steel (Figure 6.5c) as compared to the tortuous crack path in the other two steels (Figure 6.5a and b) can be one reason explaining the highest crack growth rates in this steel.

As explained in the Introduction, there is a debate in the literature whether crack growth acceleration under periodic underloads occurs during the underload cycle or during the baseline cycles [116, 117, 178]. In the present study, a fractography analysis was carried out to address this question. There was a clear distinction between underload striations and baseline cycles striations in the case of the 304L steel at  $K_{\max,20}$  (Figure 6.11). Striation spacing measurements were carried out using an image analysis software. The average striation spacing at  $R_{UL} = 0.1$  is close to the one measured at  $R = 0.1$  under constant amplitude loading ( $0.567 \pm 0.05$  versus  $0.497 \pm 0.05$   $\mu\text{m}/\text{striation}$ , respectively). Thus, acceleration of crack growth does not occur during the underloads.

The fatigue striations at  $R = 0.7$  under constant amplitude loading are poorly defined as compared to the baseline cycle striations under periodic underloads. In spite of that, it was found that the macroscopic crack growth in one cycle at  $R = 0.1$  ( $0.285 \pm 0.03$   $\mu\text{m}$ ) is comparable to that of 10 cycles at  $R = 0.7$  ( $0.272 \pm 0.01$   $\mu\text{m}$ ) as shown in Figure 6.7. Thus, assuming that the average microscopic crack growth remains proportional, the striation spacing of ten baseline cycles should be equal to that of an underload in one load block. However, the striation measurements in Figure 6.11a show that ten baseline cycles striation spacings,  $10\delta_{BL}$ , are on average three times larger than one underload striation spacing,  $\delta_{UL}$  ( $1.737 \pm 0.70$  versus  $0.567 \pm 0.05$   $\mu\text{m}$ , respectively). These observations substantiate that acceleration factors are due to a faster crack growth during baseline cycles rather than during underloads.

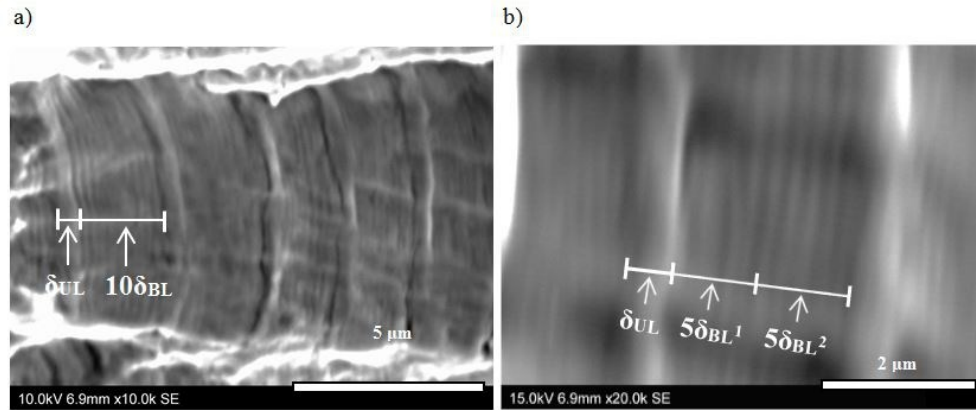


Figure 6.11 Striations on fatigue surfaces in the 304L steel at  $K_{\max,20}$  under periodic underloads ( $R_{BL} = 0.7$ ,  $R_{UL} = 0.1$  and  $n = 10$ ). Figure 5.11 (b) is an enlargement of Figure 5.11 (a) (the crack propagates from left to right in all cases)

A combination of high amount and slow decrease of the tensile residual stress after the underload can contribute to higher crack growth during baseline cycles as compared to constant amplitude loading [120, 175]. In the present study, considering baseline cycles striations of the 304L steel shown in Figure 6.11, there is not a large difference between the first five striation spacings,  $5\delta_{BL}^1$  and the second five ones,  $5\delta_{BL}^2$  ( $0.898 \pm 0.02 \mu\text{m}$  as compared to  $0.839 \pm 0.03 \mu\text{m}$ , respectively). It can be concluded that the decrease of the tensile residual stress is slow for this steel and cannot be seen on the striation spacings of the first 10 baseline cycles. More subsequent cycles are required to see a marked difference between striation spacings.

As stated in the literature, the strain-hardening can also lead to crack growth acceleration [125, 126]. In the present study, the periodic underloads can strain-harden the crack tip and lower the local, leading to a faster crack growth during the baseline cycles. The 304L steel has the highest acceleration factors and the 415 steel has the lowest ones (Figures 6.9 and 6.10). Intermediate values are obtained for the A516 steel. This difference in acceleration factors probably results from the different strain hardening behaviors of these steels (see tensile properties, Table 6.4).

Regarding the crack growth prediction methods, the LDS method provides a good prediction of crack growth in the 415 steel at low and high  $K_{\max}$ . However, this method underestimates the crack growth in the A516 steel and more importantly in the 304L steel. The prediction based on  $\Delta K_{\text{rms}}$  prediction underestimates the crack growth in all steels more than LDS does.

## 6.6 Conclusions

Fatigue crack growths in three steels, AISI 415, ASTM A516, and AISI 304L were measured under constant amplitude loading and variable amplitude loading at two  $K_{\max}$  levels. The tests under constant amplitude loading were conducted at 4 load ratios ( $R = 0.1, 0.3, 0.5,$  and  $0.7$ ). Those under variable amplitude loading consist of baseline cycles at three load ratios ( $R = 0.3, 0.5,$  and  $0.7$ ) intercut with periodic underloads at  $R = 0.1$ . For simplicity, this load sequence was termed periodic underloads. The crack growth rates under constant amplitude were employed in the linear damage summation method to predict the crack growth under periodic underloads. Thereafter, the measured crack growths were compared to this prediction.

The 304L steel has the highest crack growth rates as compared to the two other steels under constant amplitude loading. The quasi-straightness of the crack path can be one parameter explaining this difference. Walker equations were derived for each steel. They give good predictions of the crack growth rates at both  $K_{\max}$  and all  $R$  ratios.

Crack growths under periodic underloads are higher than those predicted by linear damage summation of crack growth under constant amplitude loading. The acceleration factors are the highest in the 304L steel (up to 2.53) and the lowest in the 415 steel (close to unity). Intermediate values are obtained for the A516 steel. The acceleration factors are maximum at the higher value of  $n$  ( $n = 10$  versus  $n = 3$ ) and at the lower  $K_{\max}$  level ( $19.43 \text{ MPa}\cdot\text{m}^{1/2}$ ) for all three steels. The higher the load ratio of baseline cycles, the higher the acceleration factors are in most conditions.

The fractography analysis of the 304L steel at  $K_{\max,20}$  show that acceleration factors are due to faster crack growth during the baseline cycles. A combination of high tensile residual stress and slow decrease of this stress after an underload can be one cause of this faster crack growth. Moreover, strain hardening induced by periodic underloads can decrease the ductility at the crack tip, also leading to higher crack growth during the subsequent baseline cycles.

In the present study where the SIF range of small load cycles are much lower than the fatigue threshold, the linear damage summation can be employed to predict the defects growth in the runners made of 415 steel due to large cycles like POV and SS. However, for the runners made of the other two steels, the acceleration factors should be considered in the prediction in order not to underestimate fatigue crack propagation.

**Acknowledgements**

This work was supported by the Natural Science and Engineering Research Council of Canada, Alstom Renewable Power Canada and Hydro-Québec Research Institute. The authors would like to thank Denis Thibault and Stéphane Godin for the X-ray diffraction analysis and the technologist Carlo Baillargeon for his assistance.

## CHAPTER 7 ARTICLE 2: FATIGUE THRESHOLD AT HIGH STRESS RATIO UNDER PERIODIC UNDERLOADS IN TURBINE RUNNER STEELS

Published in *International Journal of Fatigue*, Vol. 103, 2017, pp. 264-271

M. Hassanipour<sup>a</sup>, Y. Verreman<sup>a</sup>, J. Lanteigne<sup>b</sup>

<sup>a</sup>Department of Mechanical Engineering, École Polytechnique de Montréal, Montréal, Québec, Canada, H3T 1J4

<sup>b</sup>Institut de Recherche d'Hydro-Québec, Varennes, Québec, Canada, J3X 1S1

A review of different load procedures to reach the fatigue threshold under constant amplitude loading and periodic underloads is presented. The aim of this experimental work is to determine the effect of turbine start/stop sequences (periodic underloads) on the fatigue threshold of small cycles at high stress ratio (baseline cycles) in two steels used in turbine runners, i.e. AISI 415 and 304L steels. Keeping  $K_{\max}$  constant, a first load procedure is conducted with decreasing  $\Delta K$  to measure fatigue thresholds at  $2 \times 10^{-7}$  mm/cycle under both constant amplitude loading and periodic underloads at various frequencies. Then a second load procedure is conducted to measure fatigue thresholds under periodic underloads at one frequency with increasing  $\Delta K$  of baseline cycles from zero. The periodic underloads applied above a certain frequency decrease the fatigue threshold measured at crack propagation rate of  $2 \times 10^{-7}$  mm/cycle. The decrease in fatigue threshold due to periodic underloads is about five times higher when it is measured at  $6.7 \times 10^{-9}$  mm/cycle.

**Keywords:** Fatigue threshold; Constant  $K_{\max}$  procedure; Periodic underloads; Turbine runner steels; Linear damage summation

## Nomenclature

$a$	crack length
$\Delta a_{\text{block}}$	crack growth in one load block
$K_{\text{max}}$	maximum SIF
$\Delta K$	SIF range
$\Delta K_{\text{BL}}$	SIF range of baseline cycles
$\Delta K_{\text{eff}}$	effective SIF range
$\Delta K_{\text{th}}$	threshold SIF range
$\Delta K_{\text{th,conv}}$	conventional fatigue threshold ( $2 \times 10^{-7}$ mm/cycle)
$\Delta K_{\text{th,true}}$	true fatigue threshold ( $6.7 \times 10^{-9}$ mm/cycle)
$\Delta K_{\text{th,CAL}}$	true fatigue threshold under constant amplitude loading
$n$	number of baseline cycles over number of underload cycles
$R$	stress ratio
$R_{\text{UL}}$	stress ratio of an underload cycle
$r_{\text{yc}}'$	cyclic plastic zone size of an underload cycle

## Abbreviations

BL	baseline cycles
CAL	constant amplitude loading
L	longitudinal direction of the plate
LT	long-long transverse orientation
PUL	periodic underloads
SS	start/stop sequences
SIF	stress intensity factor
T	transverse direction of the plate
UL	single underload

## 7.1 Introduction

Critical regions of turbine runners are subjected to small stress amplitude cycles that are superimposed to a static tensile stress. These small cycles at very high frequency are generated by the pressure fluctuations in runners that are induced by hydraulic phenomena and rotor-stator interactions. Further large stress amplitude cycles at low frequency are generated by changes in the operating conditions of the power station that varies the static tensile stress, i.e., start/stop sequences, power output variations and load rejections.

In recently built runners, the amplitude of small cycles is low (a few MPa) and does not induce crack growth, so these cycles can be neglected on condition that the crack is not very large. In such a case, the relevant issue is to know the interaction effect between different large cycles on the crack growth. A first study on this effect was recently made by the authors for different steels used in turbine runners [191]. However, in aged runners in operation since many years, the stress amplitude of small cycles can reach higher values (tens of MPa) that contribute to the crack propagation [154, 155].

The small stress cycles reach a very high number (about  $7 \times 10^{10}$  cycles) during the 70 years design life of the runner [154]. If a pre-existing defect is subjected to these cycles, the SIF range at its tip must be below the fatigue crack growth threshold; otherwise, the defect will propagate and cause a premature failure of the runner. For this reason, the fatigue threshold at high R ratios has to be measured at very low crack growth rates.

Further, the static tensile stress is periodically decreased to zero by the start/stop (SS) sequences. These sequences, which are to be considered as periodic underloads, may cause a decrease in the fatigue threshold of baseline cycles at high R ratios [103, 108]. As a consequence, the critical length of a defect may be decreased. Therefore, the fatigue threshold of the baseline cycles intercut with periodic underloads should also be measured.

First we present a literature review of previous studies on load procedures conducted to measure fatigue threshold under constant amplitude loading and periodic underloads. The term "periodic underloads" is also used to name the variable amplitude loading consisting of baseline cycles intercut with periodic underloads.

In fatigue crack propagation tests at constant R-ratio, after a conventional pre-cracking, initial  $\Delta K$  and  $K_{\max}$  parameters have to be gradually decreased with respect to crack length,  $a$ , in order to

reach the fatigue threshold. However, a higher decreasing gradient of the aforementioned parameters induces a higher increase in the crack closure levels during the decreasing procedure [25]. This can decrease the crack growth rate at a given  $\Delta K$  in the near-threshold region and increase the fatigue threshold at a given crack growth rate [32]. As a consequence, different load procedures are proposed in the literature in order to minimize crack closure, while reaching the fatigue threshold.

In order to minimize crack closure while reaching the fatigue threshold some studies proposed a step-by-step decreasing  $K_{\max}$  procedure [192]. Throughout the test, the decrease in  $K_{\max}$  at each step should not be more than 10% and the crack length must grow three times beyond the previous monotonous plastic size [32, 109]. These conditions lead to an increase of the gradient,  $dK_{\max}/da$ , as  $K_{\max}$  decreases towards the fatigue threshold. Moreover, they were imposed to minimize the plasticity-induced crack closure in the lower Paris region. However, when the crack approaches the near-threshold region, the roughness-induced crack closure level becomes much higher than the plasticity-induced crack closure [39, 110].

Later, some authors proposed a continuous decreasing  $K_{\max}$  procedure (Figure 7.1a) where the relative decrease of the monotonous plastic zone with the crack length remains constant [161, 192]. This leads to the following equation,

$$\frac{1}{K_{\max}} \left( \frac{dK_{\max}}{da} \right) = C \quad , \quad \text{at constant R ratio} \quad (7.1)$$

As a result, the gradient,  $dK_{\max}/da$ , decreases as  $K_{\max}$  decreases towards the fatigue threshold. Further, a wide range of fatigue tests with different  $C$  gradients were conducted on different alloys in order to find conditions that minimize the crack closure while reaching fatigue threshold. The results suggested that the negative  $C$  gradient should not be lower than  $-0.08 \text{ mm}^{-1}$  [32]. The previous studies were gathered in order to write the body of the ASTM standard E647 [160].

Under loading at high  $R$  ratios using a decreasing gradient close to the one suggested by ASTM standard ( $C = -0.06 \text{ mm}^{-1}$ ), a higher fatigue threshold was obtained by increasing the initial  $K_{\max}$  in an 5083-H321 aluminum alloy [32, 35]. Based on fractographic observations, it was concluded that this effect is due to some crack closure induced by a high initial  $K_{\max}$ . This is confirmed by recent studies which also measured local crack closure at high  $R$  ratios using the ASTM load shedding procedure [85, 175]. Another study has shown that the fatigue threshold of an 2024-T3 aluminum

alloy is sensitive to the initial  $K_{\max}$  as well as to the decreasing gradient,  $dK_{\max}/da$ , while that of a 6Al-4V titanium alloy is less sensitive to these parameters [193].

In order to eliminate the effects of the initial  $K_{\max}$  and the decreasing gradient,  $dK_{\max}/da$ , while reaching the fatigue threshold at high R ratios, another procedure was proposed. It consists of keeping  $K_{\max}$  constant while  $\Delta K$  is gradually decreased until the fatigue threshold,  $\Delta K_{\text{th}}$ , is reached (Figure 7.1b). This decrease is made according to the following equation,

$$\frac{1}{\Delta K} \left( \frac{d\Delta K}{da} \right) = C \quad , \quad \text{at constant } K_{\max} \quad (7.2)$$

In this procedure where the monotonous plastic zone size remains constant throughout the test, a higher decrease in the cyclic plastic zone size does not induce a higher crack closure in the crack wake in aluminum and steel alloys [36, 194]. As a result, a high decreasing gradient,  $d\Delta K/da$ , can be applied and a fatigue threshold can be reached in a shorter time [36]. Other studies, conducted on a wide range of aluminum and titanium alloys using decreasing gradients,  $d\Delta K/da$ , between  $-0.06 \text{ mm}^{-1}$  and  $-0.62 \text{ mm}^{-1}$  have confirmed that there is no gradient effect [37, 195-197].

(a)

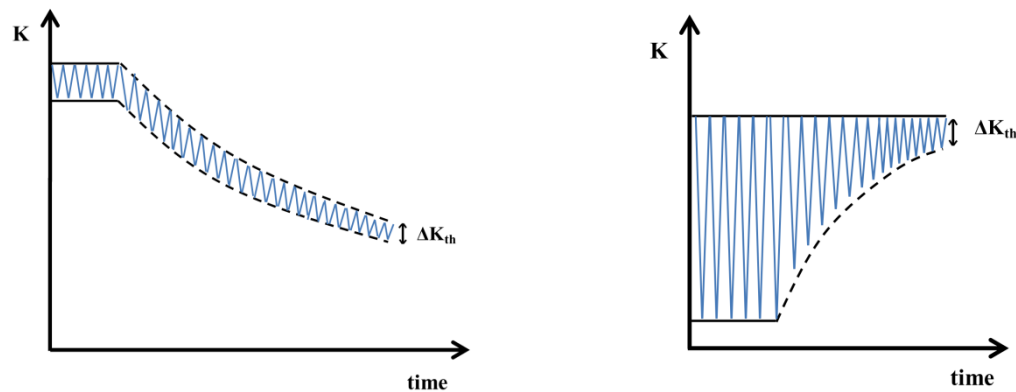


Figure 7.1 Two different load procedures to measure the fatigue threshold at high R ratio, (a) constant R ratio (ASTM standard), (b) constant  $K_{\max}$  [37]

However, the fatigue threshold measured by this procedure may depend on the  $K_{\max}$  level [195]. As  $K_{\max}$  is increased, mechanisms of static fracture (e.g. void growth) are promoted at the crack tip, which decreases the fatigue threshold for some alloys [198, 199].

In some studies on a 2024-T351 aluminum alloy and in low carbon steels, the step-by-step decreasing  $K_{\max}$  procedure was conducted to measure the fatigue threshold of baseline cycles at a high R ratio with underloads periodically applied during the  $K_{\max}$  decrease (Figure 7.2) [120, 128,

200]. The fatigue threshold at high R ratio was decreased by the periodic underloads. This decrease depends on two parameters. The first one is the ratio of the number of baseline cycles over that of underloads,

$$n = \frac{\Delta N_{BL}}{\Delta N_{UL}} \quad (7.3)$$

As shown in Figure 7.3, the fatigue threshold at high R ratio of the 2024-T351 aluminum alloy decreases with decreasing  $n$ , below  $n = 10^4$  [120, 128].

The second parameter is the ratio of the SIF range of baseline cycles over that of periodic underloads,

$$\Psi = \frac{\Delta K_{BL}}{\Delta K_{UL}} \quad (7.4)$$

As shown in Figure 7.3, the fatigue threshold of the 2024-T351 aluminum alloy under compressive periodic underloads ( $R_{UL} = -0.2$ ) is further decreased as compared to periodic underloads ( $R_{UL} = 0$ ).

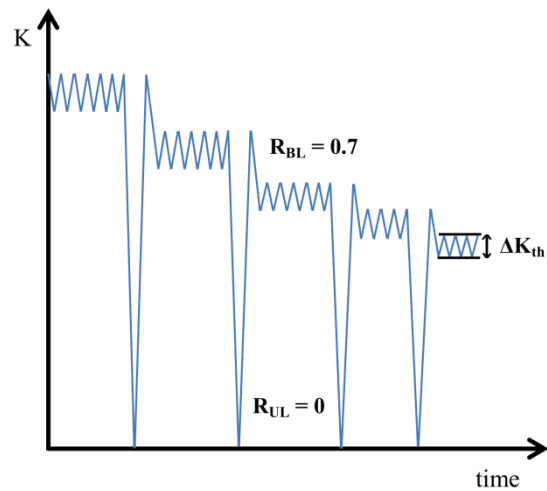


Figure 7.2 Step-by-step decreasing  $K_{max}$  load procedure to measure the fatigue threshold at constant high R ratio under PUL (adapted from [128])

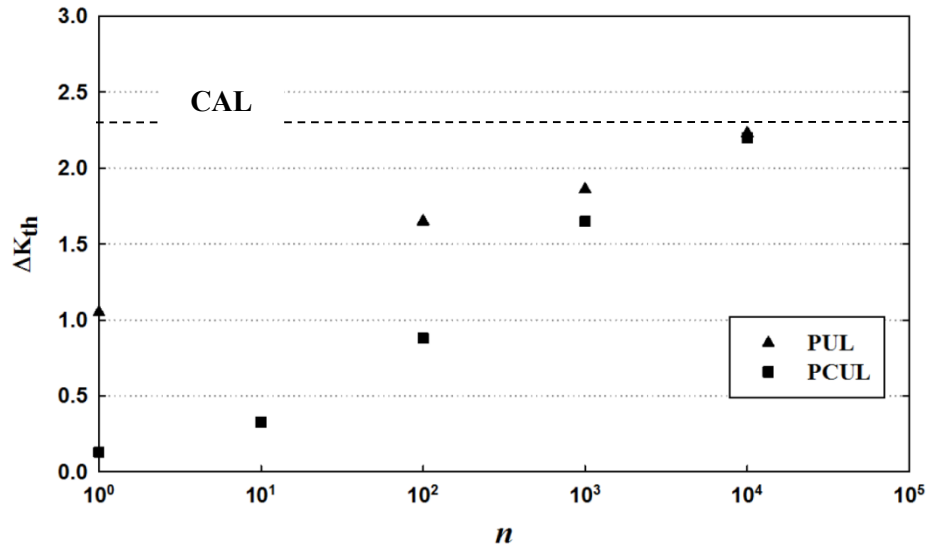


Figure 7.3 Effect of  $n$  ratio on the fatigue threshold at high R ratio of an 2024-T351 aluminum alloy under periodic underloads (PUL) and periodic compressive underloads (PCUL) (adapted from [128])

Regarding the constant  $K_{\max}$ , the periodic underloads decrease the fatigue threshold at high R ratios [133, 134]. In a study on a IMI 834 titanium alloy, several load procedures were conducted under constant amplitude loading at different  $K_{\max}$  levels, as well as under periodic underloads where several consecutive underloads are applied in each load block while  $\Delta K_{BL}$  is gradually decreased (Figure 7.4) [132]. The consecutive underloads are represented by only one large cycle in the figure. As  $K_{\max}$  increases, the fatigue thresholds under constant amplitude loading and periodic underloads decrease (Figure 7.5). The relative decrease in the fatigue threshold increases as  $K_{\max}$  decreases.

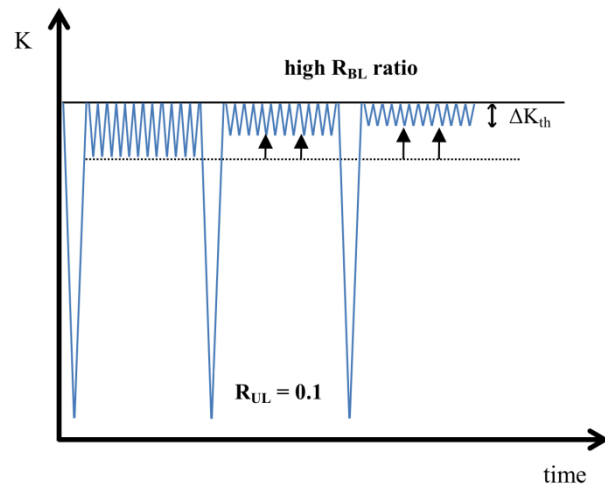


Figure 7.4 Constant  $K_{\max}$  procedure to measure the fatigue threshold at high R ratio under PUL (adapted from [132])

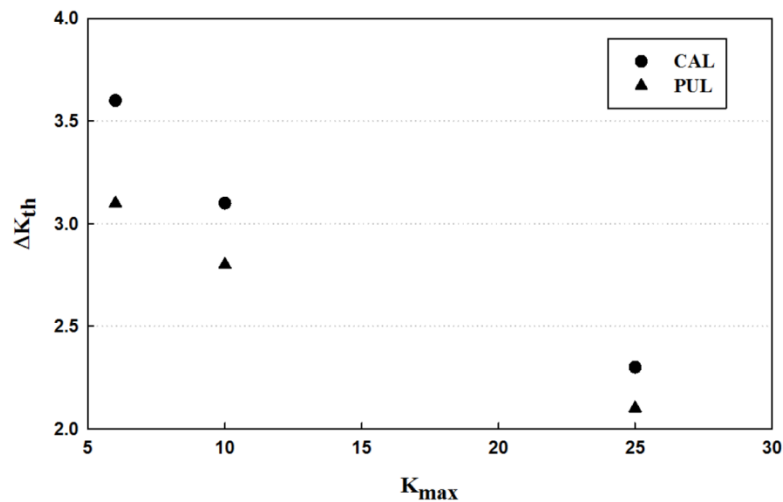


Figure 7.5  $K_{max}$  effect on the fatigue threshold under CAL and PUL (adapted from [132])

Note that in most of the aforementioned studies, fatigue threshold is conventionally measured under constant amplitude loading and periodic underloads at crack growth rates of about  $10^{-7}$  mm/cycle. However, it was pointed out that as the crack growth rate decreases, the effect of periodic underloads on the fatigue threshold can increase [108].

In the present experimental work, we measure the fatigue threshold of baseline cycles at crack growth rates of  $2 \times 10^{-7}$  and  $6.7 \times 10^{-9}$  mm/cycle at a constant  $K_{max}$  for two stainless steels, i.e. AISI 415 and 304L, used in turbine runners. Afterwards, we determine the effect of periodic underloads on the fatigue threshold of baseline cycles at those crack growth rates using two load procedures.

## 7.2 Materials and experimental procedure

### 7.2.1 Materials

Fatigue crack propagation in AISI 415 and 304L steels is investigated in this study. For simplicity, these steels are hereafter called the 415 and 304L steels. The 415 is a hot rolled martensitic stainless steel, which is annealed at  $1000^{\circ}$  C, then water cooled and tempered at  $600^{\circ}$  C. The 304L is a hot rolled and annealed austenitic stainless steel. The cast version of these two steels (CA6NM and CF3, respectively) are often used in turbine runners fabrication, however, here the wrought versions were chosen in order to have less dispersion in the results. The chemical composition of both steels are given in [191]. After polishing down to  $1 \mu\text{m}$  with diamond paste, the microstructures of the two steels are revealed using different etchants and etching techniques [191] (Figure 7.6). The austenitic grain sizes on each plane are measured using an image analysis software according to

the guidelines of ASTM E1382 [185]. The measured grain sizes on the three orthogonal planes are close together in each steel. The average values are  $100 \pm 45 \mu\text{m}$  in the 415 steel, and  $56 \pm 16 \mu\text{m}$  in the 304L steel.

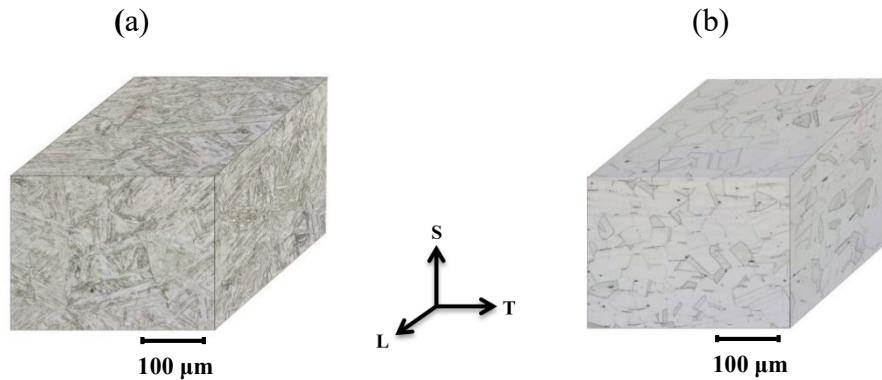


Figure 7.6 Microstructure of the two wrought steels: (a) 415 steel, and (b) 304L steel

Tensile properties of each steel in L and T directions are close together [191]. The average yield strengths are 725 MPa and 261 MPa and the average ultimate tensile strengths are 843 MPa and 704 MPa, in the 415 and 304L steels, respectively.

### 7.2.2 Fatigue testing

Tests were performed using a closed loop servo-hydraulic machine equipped with a 20 kN dynamic load cell. Compact tension specimens having geometry according to ASTM E647, 50.8 mm wide and 12.7 mm thick, were tested in LT orientation [160].

For each steel, one compact tension specimen is pre-cracked at  $K_{\max} = 11.11 \text{ MPa}\cdot\text{m}^{1/2}$  and  $R = 0.1$ . This value corresponds to a nominal stress of 170 MPa, applied to a semi-elliptical defect with dimensions of  $2.5 \text{ mm} \times 6 \text{ mm}$  at the surface of a turbine runner [154, 155]. Keeping  $K_{\max}$  constant, a first load procedure is conducted with decreasing  $\Delta K$  in order to measure fatigue thresholds under both constant amplitude loading and periodic underloads at various frequencies. Then a second load procedure is conducted to measure fatigue thresholds under periodic underloads at one frequency with increasing  $\Delta K_{\text{BL}}$  from zero.

Atmospheric conditions were periodically recorded with a thermo-hygrometer. The test temperature was  $23^\circ\text{C}$  with a relative humidity between 40 % and 45 %. All tests were conducted with a frequency equal to 15 Hz. The crack growths were optically measured and their rates were determined using the secant method.

Throughout the tests, the crack opening displacement was measured using a clip gauge installed at the mouth of the specimen. The load-displacement loops were analyzed after each test in order to evaluate the crack closure levels in the baseline and underload cycles using a 4% compliance offset criterion according to ASTM E647 [160].

**a) First load procedure (CAL and PUL)**

After the pre-cracking, the initial  $K_{\max}$  is held constant while  $\Delta K$  is decreased according to equation 2 with  $C = -0.29 \text{ mm}^{-1}$  until the crack reaches a growth rate equal to  $2 \times 10^{-7} \text{ mm/cycle}$  (Figure 7.7 and Figure 7.8, sequence 0-1). A conventional fatigue threshold,  $\Delta K_{\text{th,conv}}$ , is measured at this crack growth rate, that is a typical rate considered in most of studies on  $\Delta K_{\text{th}}$ .

Then, at constant  $K_{\max}$  and at  $\Delta K_{\text{BL}} = \Delta K_{\text{th,conv}}$ , periodic underloads at  $R_{\text{UL}} = 0.1$  are applied at a given frequency (Figure 7.7, point 2). The periodic underloads increase the crack growth rate of the baseline cycles, so the growth rate at point 1 in Figure 7.8 increases to the one at point 2.

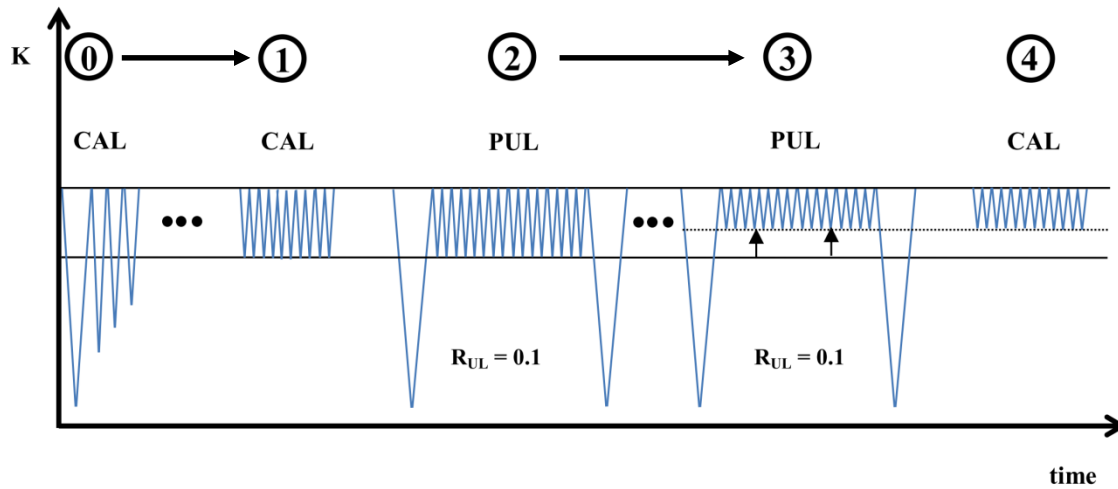


Figure 7.7 Load sequences in the first load procedure with decreasing  $\Delta K$  under CAL and PUL at a given  $n$  ratio

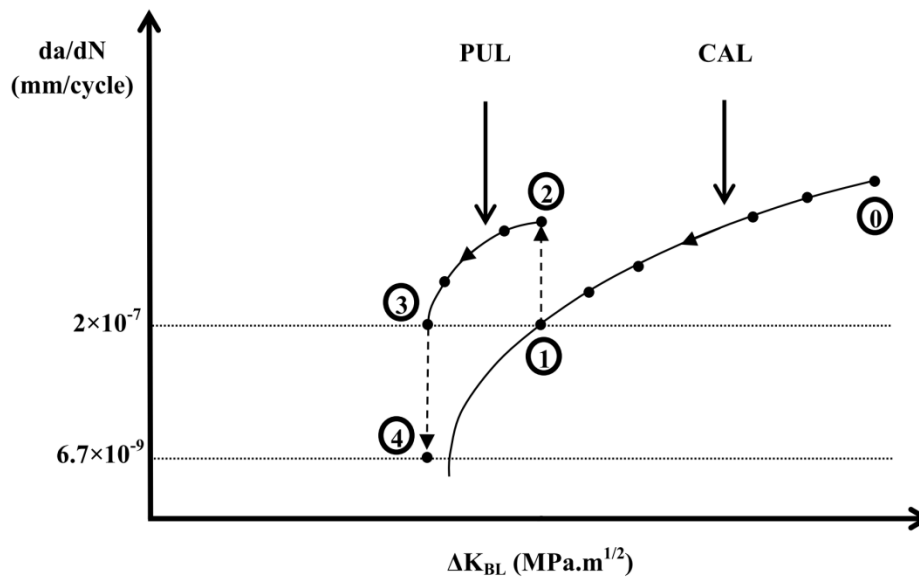


Figure 7.8 Expected results of load procedure in Figure 7.7 in a  $da/dN - \Delta K_{BL}$  plot

Next,  $\Delta K_{BL}$  is decreased according to equation 2 with  $C = -0.49 \text{ mm}^{-1}$  until the crack reaches a growth rate equal to  $2 \times 10^{-7} \text{ mm/cycle}$  (Figure 7.7 and Figure 7.8, sequence 2-3). Here, a conventional fatigue threshold,  $\Delta K_{th,conv}$ , is measured under periodic underloads.

Finally, the crack growth rate is measured at the last  $\Delta K_{th,conv}$  without periodic underloads, i.e. under constant amplitude loading (Figure 7.7, point 4). Therefore, the growth rate at point 3 in Figure 7.8 drops to the one at point 4. In this study, the limit of crack growth detection is  $5 \times 10^{-3}$

mm. If a crack is non-growing after  $0.75 \times 10^6$  cycles, its growth rate is below  $6.7 \times 10^{-9}$  mm/cycle. The  $\Delta K$  at  $6.7 \times 10^{-9}$  mm/cycle is what we call hereafter the true fatigue threshold,  $\Delta K_{th,true}$ .

The load procedure is first conducted at a small underload frequency, corresponding to  $n = 1.25 \times 10^6$ . Then the  $n$  ratio is gradually decreased from  $1.25 \times 10^6$  to  $1.25 \times 10^2$  (hereafter, we refer to  $n$  ratios ranging from  $10^6$  to  $10^2$  for simplicity). If no increase in crack growth rates is measured in sequence 1-2 at a given  $n$  ratio, the sequence 2-3-4 is not conducted.

#### **b) Second load procedure (PUL)**

Keeping  $K_{max} = 11.11 \text{ MPa.m}^{1/2}$ , a second load procedure is conducted in order to measure fatigue thresholds under periodic underloads with increasing  $\Delta K_{BL}$  step by step. The measurements are made at  $n = 1.25 \times 10^3$  only and we refer hereafter to  $n = 10^3$  for simplicity. The crack is subjected to 600 load blocks i.e.  $0.75 \times 10^6$  cycles in each step.

The first step is conducted under periodic underloads without baseline cycles (Figure 7.9 and Figure 7.10, point 0). In the next step, the initial value of  $\Delta K_{BL}$  corresponds to 20% of  $\Delta K_{th,conv}$  measured at  $n = 10^3$  in the first load procedure. This value is increased by 20% in each step until an increase in the crack growth rate is measured (Figure 7.9, sequence 0-1). The first  $\Delta K_{BL}$  that does increase the crack growth rate is the true fatigue threshold,  $\Delta K_{th,true}$ , under periodic underloads (Figure 7.10, point 1).

Next,  $\Delta K_{BL}$  is still increased by 20% in each step (Figure 7.9 and Figure 7.10, sequence 1-2) until the crack reaches a growth rate higher or equal to  $2 \times 10^{-7}$  mm/cycle. This gives another measurement of the conventional fatigue threshold,  $\Delta K_{th,conv}$ , under periodic underloads.

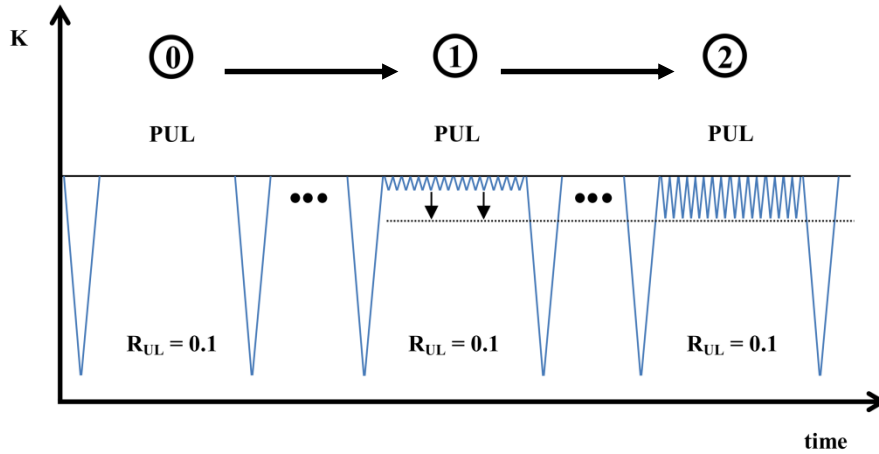


Figure 7.9 Load sequences in the second load procedure with increasing  $\Delta K_{BL}$  under PUL ( $n = 10^3$ )

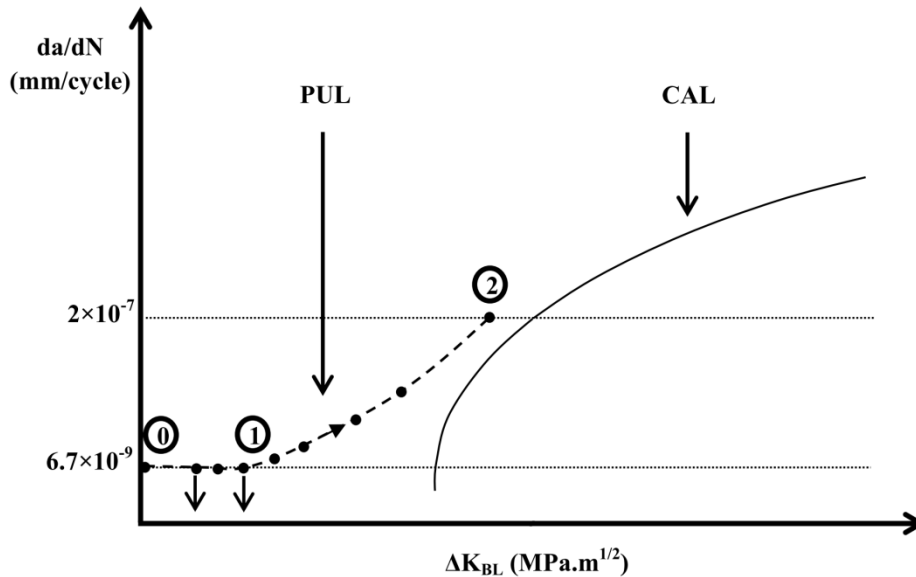


Figure 7.10 Expected results of load procedure in Figure 7.9 in a  $da/dN - \Delta K_{BL}$  plot

## 7.3 Results and discussion

### 7.3.1 First load procedure

The measured crack growth rates under constant amplitude loading in both steels are represented by a full line in Figure 7.11 and Figure 7.12. The conventional fatigue thresholds,  $\Delta K_{th,conv}$ , at  $2 \times 10^{-7}$  mm/cycle under constant amplitude loading (point 1) are close each other (3.32 and 3.35

MPa.m<sup>1/2</sup>, respectively). Periodic underloads at  $n = 10^6$  and  $10^5$  do not increase the crack growth rate of baseline cycles in both steels. However, as the periodic underloads are applied more frequently at  $n = 10^4$  and less, the crack growth rate of baseline cycles increases.

Figure 7.11 and Figure 7.12 show all crack growth rates measured in both steels using the load sequences in Figure 7.7. In particular, the variation in crack growth rates during the load sequences 1-2-3-4 at  $n = 10^2$  are indicated by dotted lines. At  $\Delta K_{BL} = \Delta K_{th,conv}$  under constant amplitude loading the crack growth rate in the 415 steel increases to  $5 \times 10^{-7}$  mm/cycle under periodic underloads (point 2, Figure 7.11), while the one in the 304L steel reaches  $10^{-6}$  mm/cycle (point 2, Figure 7.12).

It was presumed that strain hardening induced by periodic underloads lower the ductility in front of the crack tip. This effect is higher in steels with higher strain hardening and it induces a faster crack growth during the baseline cycles [191]. As a result, crack growth rate under periodic underloads  $n = 10^2$  at in the 304L steel is two times higher than the 415 steel.

This higher increase in crack growth rate under periodic underloads in the 304L steel is associated with a higher decrease in  $\Delta K_{BL}$  to reach again  $2 \times 10^{-7}$  mm/cycle at point 3. At  $n = 10^2$ , the conventional fatigue threshold,  $\Delta K_{th,conv}$ , at  $2 \times 10^{-7}$  mm/cycle is equal to 2.42 MPa.m<sup>1/2</sup> in the 304L steel as compared to 2.69 MPa.m<sup>1/2</sup> in the 415 steel.

At the aforementioned values of  $\Delta K_{BL}$ , the crack growth rates of baseline cycles without periodic underloads become non-measurable in both steels (below  $6.7 \times 10^{-9}$  mm/cycle; point 4). In the case of 304L steel a further increase in  $\Delta K_{BL}$  from 2.42 to 2.73 MPa.m<sup>1/2</sup> does not induce a crack growth. The true fatigue threshold,  $\Delta K_{th,true}$ , under constant amplitude loading stands between 2.73 and 2.85 MPa.m<sup>1/2</sup> in the 304L steel. It stands between 2.69 and 2.95 MPa.m<sup>1/2</sup> in the 415 steel.

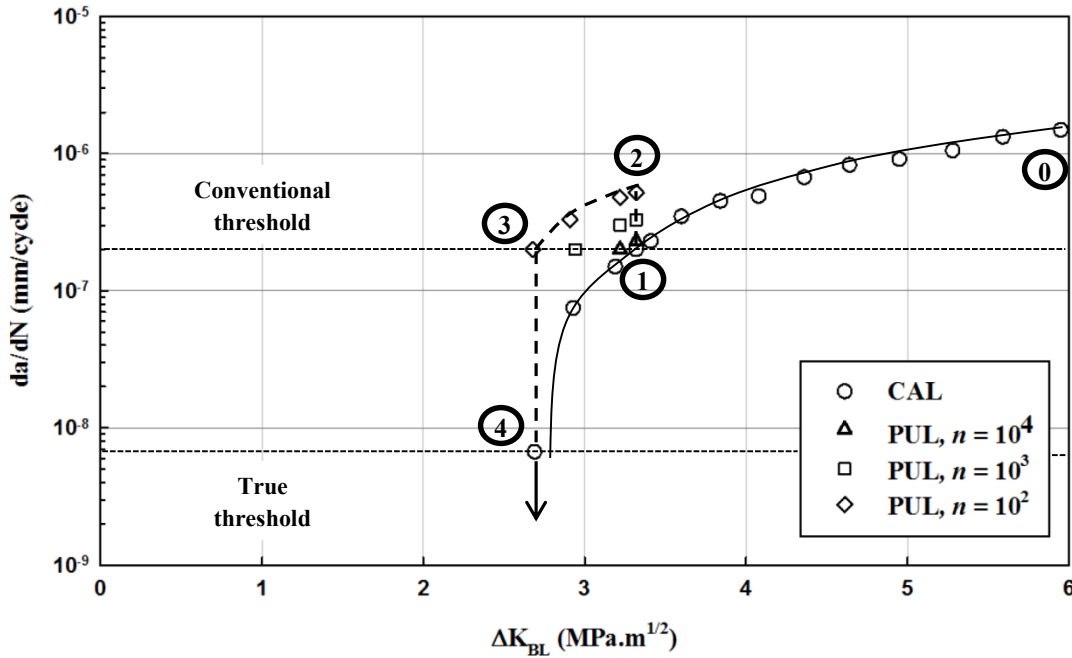


Figure 7.11 Log-linear plot of crack growth rates versus SIF range of baseline cycles under CAL and PUL at different  $n$  ratios in the 415 steel

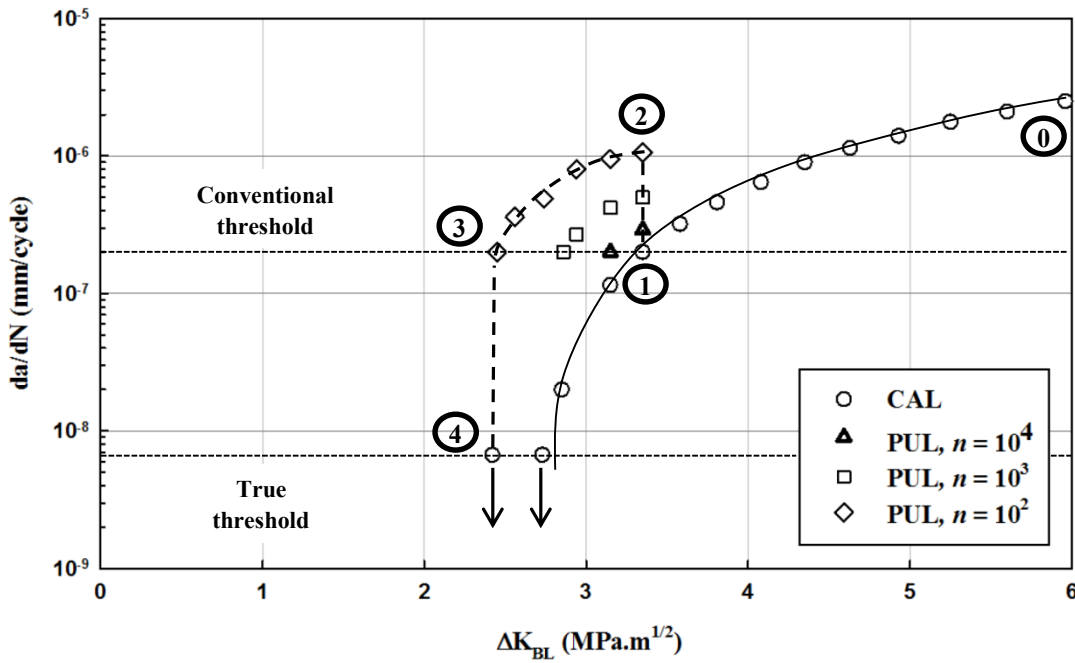


Figure 7.12 Log-linear plot of crack growth rates versus SIF range of baseline cycles under CAL and PUL at different  $n$  ratios in the 304L steel

The conventional fatigue threshold,  $\Delta K_{th,conv}$ , remains constant under periodic underloads at  $n \geq 10^5$  (Figure 7.13). However, it starts to decrease between  $10^5$  and  $10^4$ . At  $n = 10^3$ ,  $\Delta K_{th,conv}$  decreases

by 12% in the 415 steel and by 15% in the 304L steel. At  $n = 10^2$ , it decreases by 19% and 28%, respectively.

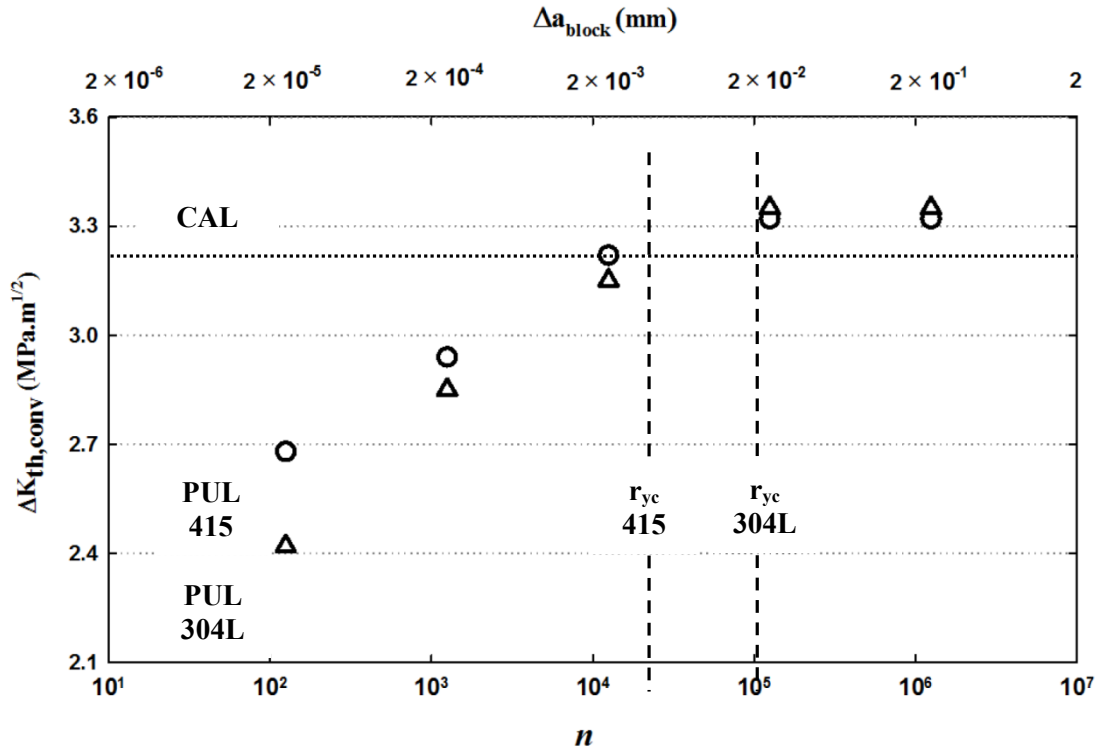


Figure 7.13 Decrease in  $\Delta K_{th,conv}$  due to periodic underloads in both steels

Applying an underload creates a large cyclic plastic zone in front of the crack. The crack growth rate of the subsequent baseline cycles can be affected as the crack grows through this zone [201]. The cyclic plastic zone size can be calculated by the following equation;

$$r_{yc}' = (1/3\pi) \times (\Delta K_{eff}/2\sigma_{yc})^2 \quad (7.5)$$

where the cyclic yield stress,  $\sigma_{yc}$ , is estimated at 690 MPa in the 415 steel and at 280 MPa in the 304L steel [202, 203]. While crack closure is never detected in the baseline cycles, the effective fraction of the SIF range,  $\Delta K_{eff}/\Delta K$  in an underload cycle is about 0.82 in the 415 steel and 0.72 in the 304L steel; the variations between  $n = 10^2$  and  $10^6$  being relatively low. At constant  $\Delta K = 10$  MPa.m<sup>1/2</sup> and  $R = 0.1$ , the cyclic plastic zone is estimated to be  $0.45 \times 10^{-2}$  mm in the 415 steel and  $2.16 \times 10^{-2}$  mm in the 304L steel.

In Figure 7.13, the horizontal upper scale gives the crack growth increment per load block,  $\Delta a_{block} = 2 \times 10^{-7}$  mm ( $n+1$ ), and the two vertical dashed lines give the underload cyclic plastic zone sizes in both steels.

At high  $n$ , the crack growth per block,  $\Delta a_{\text{block}}$ , is much higher than the cyclic plastic zone size,  $r_{yc}$ , so that the crack growth rate of baseline cycles is not affected. However, as  $n$  decreases,  $\Delta a_{\text{block}}$  decreases and becomes of the same order of magnitude as  $r_{yc}$ . The decrease in  $\Delta K_{\text{th,conv}}$  indicates that the mean crack growth rate of the baseline cycles starts to increase.

### 7.3.2 Second load procedure

The second load procedure is first used to measure the true fatigue threshold,  $\Delta K_{\text{th,true}}$ , under periodic underloads. As shown in Figure 7.14, crack growth rates are below  $6.7 \times 10^{-9}$  mm/cycle in the 415 steel with underload cycles only (point 0) and with baseline cycles until  $\Delta K_{\text{BL}} = 1.5$  MPa.m<sup>1/2</sup> (point 1). The first increase in crack growth rates are obtained at  $\Delta K_{\text{BL}} = 1.7$  MPa.m<sup>1/2</sup>. Thus, the true fatigue threshold stands between 1.5 and 1.7 MPa.m<sup>1/2</sup>.

Then crack growth rates are measured by increasing  $\Delta K_{\text{BL}}$  until  $2 \times 10^{-7}$  mm/cycle. The conventional fatigue threshold is close to that measured following the first load procedure (3.03 versus 2.93 MPa.m<sup>1/2</sup>).

The conventional fatigue threshold at  $2 \times 10^{-7}$  mm/cycle,  $\Delta K_{\text{th,conv}}$ , under constant amplitude loading decreases by 9% due to periodic underloads (from 3.32 to 3.03 MPa.m<sup>1/2</sup>). However, as shown in Figure 7.14, the decrease is much higher at very low crack growth rates. As previously mentioned, the true fatigue threshold  $\Delta K_{\text{th,true}}$  under constant amplitude loading stands between 2.69 and 2.95 MPa.m<sup>1/2</sup>, while that under periodic underloads stands between 1.5 and 1.7 MPa.m<sup>1/2</sup>. Therefore,  $\Delta K_{\text{th,true}}$  under constant amplitude loading decreases by an average of 43% due to periodic underloads.

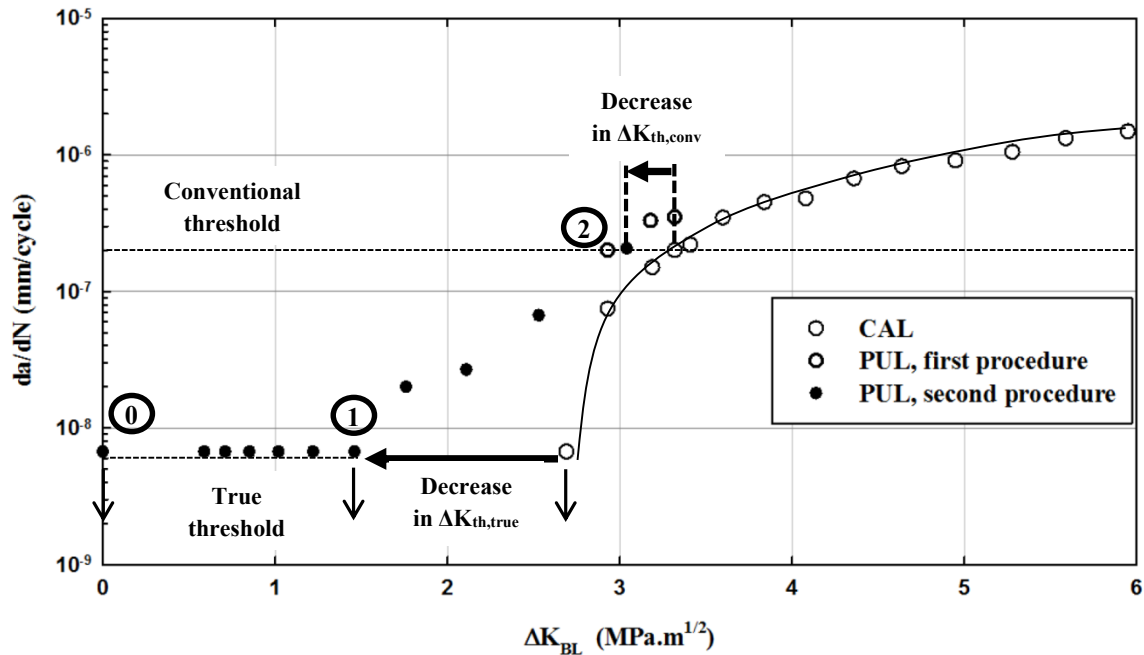


Figure 7.14 Effect of periodic underloads at  $n = 10^3$  on  $\Delta K_{th,conv}$  and  $\Delta K_{th,true}$  of the 415 steel in a log-linear  $da/dN - \Delta K_{BL}$  plot

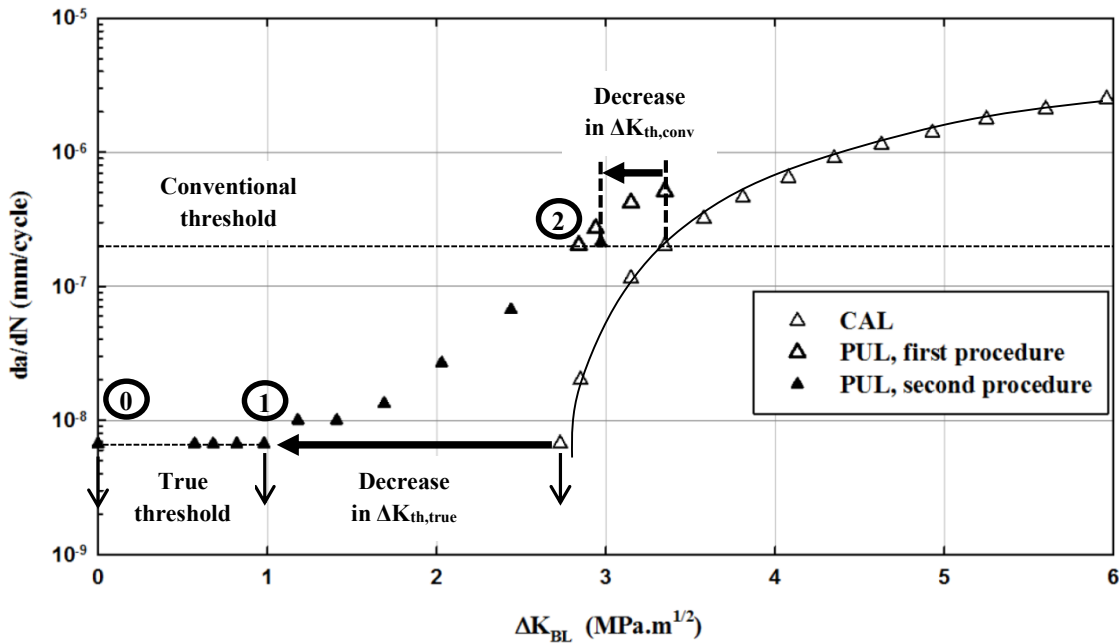


Figure 7.15 Effect of periodic underloads at  $n = 10^3$  on  $\Delta K_{th,conv}$  and  $\Delta K_{th,true}$  of the 304L steel in a log-linear  $da/dN - \Delta K_{BL}$  plot

A similar behavior is observed in the 304L steel. The conventional fatigue threshold at  $2 \times 10^{-7}$  mm/cycle,  $\Delta K_{th,conv}$  under constant amplitude loading decreases by 12% due to periodic underloads

(from 3.35 to 2.95 MPa.m<sup>1/2</sup>). However, as shown in Figure 7.15, the decrease is much higher at very low crack growth rates. The true fatigue threshold,  $\Delta K_{th,true}$ , under constant amplitude loading decreases by an average of 61% due to periodic underloads. The conventional fatigue threshold,  $\Delta K_{th,conv}$ , under periodic underloads value is only 4% higher than the one measured following the first load procedure.

## 7.4 Conclusions

The aim of the present study was to determine the effect of turbine runners start/stop (SS) sequences (periodic underloads) on the fatigue threshold of small cycles at high stress ratio (baseline cycles) in the 415 and 304L steels.

A first load procedure was conducted at constant  $K_{max}$  with decreasing  $\Delta K$  to measure a conventional fatigue threshold,  $\Delta K_{th,conv}$ , under constant amplitude loading and under periodic underloads at different  $n$  ratios. Then a second load procedure was conducted with increasing  $\Delta K_{BL}$  from zero to measured  $\Delta K_{th,true}$  and  $\Delta K_{th,conv}$  under periodic underloads at  $n = 1.25 \times 10^3$ .

According to the first procedure,  $\Delta K_{th,conv}$  starts to decrease under periodic underloads at  $n$  below  $10^5$ , when the crack growth per block becomes of the same magnitude as the underload cyclic plastic zone. While  $\Delta K_{th,conv}$  under constant amplitude are close together in both steels, the decrease in  $\Delta K_{th,conv}$  due to periodic underloads is higher in the 304L steel.

The conventional fatigue thresholds measured under periodic underloads following the first and second procedures are close together. According to the second load procedure,  $\Delta K_{th,true}$  decreases by 43% and 61% due to periodic underloads at  $n = 1.25 \times 10^3$  in the 415 and 304L steels, respectively, as compared to 9% and 12% decreases in  $\Delta K_{th,conv}$ .

The measured crack growth rates are higher than those predicted by linear damage summation (LDS). As  $\Delta K_{BL}$  increases from zero, the acceleration factor increases and it reaches a maximum value below  $\Delta K_{th,true}$  under constant amplitude loading. However, the crack growth rate predicted by LDS increases above  $\Delta K_{th,true}$ , which leads to a rapid decrease in the acceleration factor.

The periodic underloads do not decrease the fatigue threshold of baseline cycles above  $n = 1.25 \times 10^5$ . In turbine runners, the number of small cycles (baseline cycles) is around  $7 \times 10^{10}$  during the 70 years of design life. As a result, in order to avoid a decrease in the fatigue threshold, the number of start/stop sequences or other large cycles (periodic underloads) should be kept below  $5 \times 10^5$ .

**Acknowledgements**

This work was supported by the Natural Science and Engineering Research Council of Canada, Alstom Renewable Power Canada and Hydro-Québec Research Institute. The authors would like to the technologist Carlo Baillargeon for his assistance.

## CHAPTER 8 GENERAL DISCUSSION

### 8.1 Crack growth under constant amplitude loading

The results of the last four chapters are summarized and discussed in this chapter. Some additional results are presented and discussed.

It is straightforward to measure crack growth rates under constant amplitude loading in the Paris region. After a precracking, the initial  $\Delta K$  and  $K_{\max}$  should be increased with respect to crack length,  $a$ , at a constant R ratio. As an advantage, the shape and amount of the increasing gradients,  $dK_{\max}/da$ , do not affect crack growth rates in the Paris region [32].

In Chapter 5 and 6, crack growth rates were measured under constant amplitude loading in the Paris region for the 415, A516 and 304L steels. Measured crack growth rates in the 415 steel are lower than the 304L steels in the Paris region for all R ratios. The A516 has intermediate crack growth rates as compared to other two steels.

It becomes more complicated to measure crack growth rates in the near-threshold region. After a precracking, the initial  $\Delta K$  and  $K_{\max}$  should be decreased with respect to crack length,  $a$ , at a constant R ratio to reach a fatigue threshold [32]; however, a high amount of decreasing gradient,  $dK_{\max}/da$ , can induce extra crack closure level, which leads to an underestimation of the crack growth rate at a given  $\Delta K$  and an overestimation of the fatigue threshold. A load procedure with a slow and continuous decreasing gradient, i.e. so called the ASTM E647 procedure, is proposed to minimize extra crack closure while reaching the fatigue threshold [32]; however, initial  $K_{\max}$  level, and  $dK_{\max}/da$  can still induce extra crack closure [35].

In order to eliminate the consequences of the initial  $K_{\max}$  and its decreasing gradients, it was proposed to keep the  $K_{\max}$  constant while  $\Delta K$  is decreased to reach  $\Delta K_{th}$  at high R ratios. In this procedure, the  $dK_{\max}/da$  is equal to zero and only  $d\Delta K/da$  is gradually decreased to reach the fatigue threshold. Still only  $d\Delta K/da$  can induce extra crack closure but it is much lower than the one induced by both decreasing gradients [35].

Conducting the ASTM load procedure at high R ratio leads to an increase in measured crack growth rates; however, after a specific high R ratio, crack growth rates do not further increase and the fatigue threshold becomes constant [63]. On the other hand, in the constant  $K_{\max}$  procedure, crack

growth rates measured at high R ratios always increase and the fatigue threshold decreases. This is reported in some aluminum alloys and titanium alloys [195, 198].

The definition of fatigue crack growth threshold corresponds to a crack that do not grow below a certain  $\Delta K$  or the one that starts to grow by increasing  $\Delta K$  step by step from zero. It should be stated that the definition of the crack growth rate that corresponds to the fatigue threshold crack depends on the testing conditions such as precision of crack growth detection and the elapsed number of cycles. In many studies, the test condition cannot reach a crack growth rate below  $1 \times 10^{-7}$  mm/cycle [31, 120, 165]. Thus, they have defined a  $\Delta K$  corresponding to the aforementioned crack growth rate as the fatigue threshold [204, 205]. The aforementioned fatigue threshold is also recommended in American Standard ASTM E647 [160]. Since many studies have used the aforementioned definition, we preferred to call this fatigue threshold as the conventional fatigue threshold ( $\Delta K_{th,conv}$ ).

On the other hand, a  $\Delta K$  corresponding to a lower crack growth rate equal to  $1 \times 10^{-8}$  mm/cycle is defined as the fatigue threshold according to the British Standard [206]. In this study, when the crack starts or stops growing after a given  $\Delta K$  for a length of 0.005 mm and  $0.75 \times 10^7$  cycles, it is considered a true fatigue threshold. This corresponds to a growth rate equal to  $6.7 \times 10^{-9}$  mm/cycle ( $\Delta K_{th,true}$ ). Visual crack growth detected with an optical microscope has enabled this study to reach such precision.

In Chapter 5, crack growth rates were measured under constant amplitude loading using the ASTM test procedure at  $R = 0.1$  and  $0.7$ . Crack growth rates at  $R = 0.1$  in the 415 steel are lower than the ones in the 304L steel, in the Paris region, but become higher in the near-threshold region. As the  $\Delta K$  approaches  $\Delta K_{th,conv}$  the near-threshold region, crack closure levels increase in both steels and crack growth rates versus  $\Delta K_{eff}$  become close to each other. Crack closure is mainly induced by crack path irregularities and crack tip plasticity. The crack path deflection that is presumed to induce crack closure is higher in the 415 than the 304L steel. On the other hand, the plasticity that induces crack closure is lower in the 415 steel than the 304L steel. Thus, it can be stated that the crack closure is mainly induced by crack path irregularities in the 415 steel and mainly induced by plasticity in the 304L.

Crack closure is detected at  $R = 0.1$  but this is not the case at  $R = 0.7$ . Crack growth rates estimated by  $\Delta K_{eff}$  at  $R = 0.1$  are higher than the ones at  $R = 0.7$  in both steels. This leads to an estimated closure-free fatigue threshold at  $R = 0.1$  that is lower than the one at  $R = 0.7$ . This may be due to

an overestimation of crack closure in the load-COD curve at  $R = 0.1$  or to a local crack closure at  $R = 0.7$  [74, 85]. The observation on the crack path in the steels shows that similar crack path deflections also exist at high  $R$  ratio that may lead to crack closure.

Tensile residual stress is induced during the fabrication and welding procedure in runners [186]. This stress increases the maximum stress intensity factor at the crack tip, which can decrease the fatigue threshold. For this reason, crack growth rates are also measured using the constant  $K_{\max}$  procedure at  $K_{\max} = 19.44 \text{ MPa}\cdot\text{m}^{1/2}$  and compared to those at high  $R$  ratios measured at  $R = 0.7$  in Chapter 5 and at  $K_{\max} = 11.11 \text{ MPa}\cdot\text{m}^{1/2}$  in Chapter 7.

Conventional fatigue threshold,  $\Delta K_{\text{th,conv}}$ , measured at  $R = 0.7$ , corresponds to 3.35 and 3.38  $\text{MPa}\cdot\text{m}^{1/2}$  in the 415 and 304L steels, respectively. These  $\Delta K_{\text{th,conv}}$  at  $R = 0.7$  each decrease by 1% at  $K_{\max,1}$  in both steels. These values further decrease by 8% in the 415 and by 9% in the 304L steels at  $K_{\max,2}$  (Figure 8.1 and Figure 8.2). Crack closure was not observed at high  $R$  ratios for  $K_{\max,1}$  and  $K_{\max,2}$ .

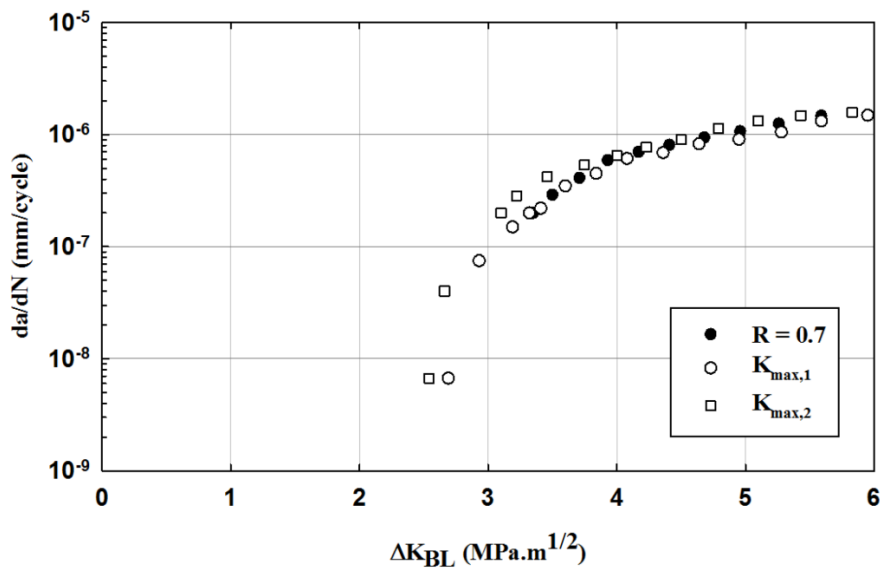


Figure 8.1 Effect of  $K_{\max}$  on crack growth rates at high  $R$  ratios in the 415 steel

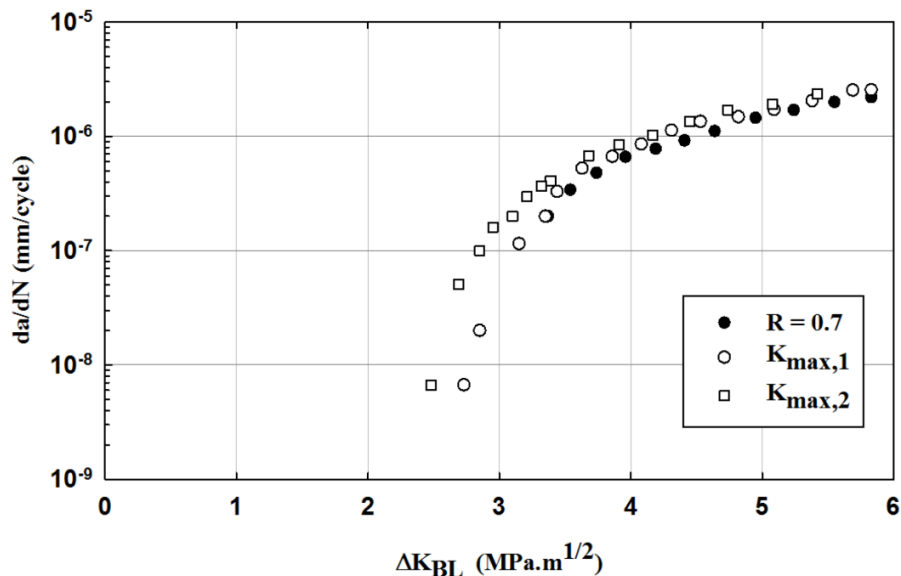


Figure 8.2 Effect of  $K_{max}$  on crack growth rates at high R ratios in the 304L steel

Tests conducted on the 415 and 304L steels show that only slightly higher crack growth rates are measured at  $K_{max,2}$  as compared to the ones at  $K_{max,1}$  and  $R = 0.7$ . At higher  $K_{max}$ , there is an 8% and 9% decrease in  $\Delta K_{th,conv}$  in the 415 and 304L steels, respectively. As the crack growth rates decrease, the decrease in  $\Delta K_{th,true}$  corresponds to 10% and 12%, respectively. Thus, there the  $K_{max}$  has a little effect of on the near-threshold region at high R ratios.

## 8.2 Crack growth under periodic underloads

It is more complicated to measure crack growth rates under periodic underloads in the Paris region than the ones under constant amplitude loading. A procedure similar the one used under constant amplitude loading can be conducted by increasing an initial  $K_{max}$  with respect to crack length,  $a$ , which leads to an increase in the initial  $\Delta K_{BL}$  and  $\Delta K_{UL}$  at a constant R ratio; however, increasing the  $d\Delta K_{BL}/da$  and  $d\Delta K_{UL}/da$  can affect the crack growth rate under periodic underloads [107]. Therefore, in Chapter 6, it was decided to conduct crack growth at a constant  $K_{max}$  in order to better measure the interaction between baseline cycles and underloads.

The results in Chapter 6, in the Paris region, showed that measured crack growths under periodic underloads in the 415 steel are close to the ones predicted by LDS. On the other hand, measured crack growths in the 304L steel are three times higher than those predicted by LDS. Intermediate values were obtained for the A516 steel. The 415 steel has the lowest strain hardening exponent,

the 304L has the highest one, and the A516 has intermediate values. Therefore, it is concluded that as the monotonous strain hardening increases in the steels, the acceleration factor increases.

That being said, the aforementioned conclusion is given by comparing three different steels with different strain hardening capacity. Many other factors may influence the acceleration factor in one steel as compared to the other two. Thus, acceleration factors should be compared in a same steel with different monotonous strain hardening. It should be mentioned that comparing the cyclic strain hardening curve for these steels should be compared, but we decided to compare them by the available measured monotonic strain hardening curve.

For this reason, tensile and CT specimens were fabricated from a new plate of A516 steel to compare their strain hardening and acceleration factors with those of A516 steel in Chapter 6 (old plates of A516 steel). These two different plates are referred to as the new A516 steel and old A516 steel.

Results show that the new A516 steel respects all tensile properties suggested by the ASTM A516 standard. On the other hand, the old A516 steel respects all values proposed by the standard except for the tensile strength (Table 8.1). The new A516 steel has a lower strain hardening exponent as compared to the old one (0.24 vs 0.29).

Table 8.1 Comparison of tensile properties in the old and new A516 steel with ASTM A516

Steels	0.2% Yield stress (MPa)	Tensile strength (MPa)	Maximum elongation ( $\epsilon_r$ )	Strain hardening exponent (s)
<b>New A516</b>	344	511	0.26	0.24
<b>Old A516</b>	300	476	0.37	0.29
<b>ASTM A516</b>	260 (min.)	485-620	0.21 (min.)	-

In order to calculate acceleration factors in the new A516 steel, crack growth rates should be measured under constant amplitude loading and periodic underloads. Using a CT specimen with the same geometry as the one specified in Chapter 6, crack growth rates are measured under constant amplitude loading at  $R = 0.1$  and  $R = 0.7$  to calculate the LDS in the new A516. The crack growth rate under constant amplitude loading at  $R = 0.1$  is  $3.02 \times 10^{-5}$  mm/cycle and at  $R = 0.7$  is

$1.77 \times 10^{-6}$  mm/cycle. These values are close to those in the old A516, which is  $2.91 \times 10^{-5}$  mm/cycle and  $1.77 \times 10^{-6}$  mm/cycle, respectively.

Crack growth rates were then measured under periodic underloads with underloads at  $R = 0.1$  followed by baseline cycles at  $R = 0.7$  with  $n = 3$  and 10 at  $K_{\max} = 19.44 \text{ MPa}\cdot\text{m}^{1/2}$ . Ratios between measured crack growths and those predicted by LDS are given as acceleration factors in the new A516 and are compared to those in the old one in Table 8.2. The new A516 steel has lower acceleration factors at both  $n$  values as compared to the new one. In other words, the old A516 steel with the higher strain hardening exponent has higher acceleration factors than the new one. Thus, it can be said that increasing the monotonous strain hardening in a steel such as the A516 results in an increase in acceleration factors.

Table 8.2 Comparison of acceleration factors in the old and new A516 steels at  $n = 3$  and 10 at

$$K_{\max} = 19.44 \text{ MPa}\cdot\text{m}^{1/2}$$

<b>Acceleration factors</b>		
<b>Steel</b>	<b><math>n = 3</math></b>	<b><math>n = 10</math></b>
<b>New A516</b>	1.26	1.61
<b>Old A516</b>	1.39	1.77

Regarding the fractography analysis in Chapter 6, it is concluded that an underload followed by baseline cycles causes an increase in crack growth during baseline cycles. Moreover, it is presumed that an underload also induces a combination of high tensile residual stress and strain hardening that increase crack growth during subsequent baseline cycles.

One of the most complicated procedures is the measurement of crack growth rates under periodic underloads in the near-threshold region. Many studies in literature applied decreasing gradients suggested by the ASTM E647 to reach the fatigue threshold of baseline cycles; periodic underloads are subsequently applied to see the effect of periodic underloads on the fatigue threshold [120]. Other load procedures applied the decreasing gradients suggested by the ASTM E647 for baseline cycles combined with periodic underloads to reach the fatigue threshold [120]; however, the aforementioned procedures generate a  $d\Delta K_{BI}/da$  and  $d\Delta K_{UI}/da$  that induce extra crack closure in the crack wake while reaching the fatigue threshold. Other studies conducted load procedures at a

constant  $K_{\max}$  under periodic underloads in order to eliminate the decreasing gradient,  $d\Delta K_{UL}/da$ , to minimize extra crack closure levels while reaching the fatigue threshold [132].

In Chapter 7 two load procedures were proposed at a constant  $K_{\max}$ . In the first load procedure, the  $\Delta K$  was decreased in order to reach the conventional fatigue threshold,  $\Delta K_{th,conv}$  under constant amplitude loading. The load procedure also leads to the measurement of the conventional fatigue threshold under periodic underloads for  $n$  ranging from  $1.25 \times 10^2$  and  $1.25 \times 10^6$ .

The conventional fatigue threshold,  $\Delta K_{th,conv}$ , under periodic underloads at  $n = 1.25 \times 10^5$  and  $1.25 \times 10^6$  is equal to the one under constant amplitude loading for the 415 and 304L steels; however, as the  $n$  decreases below  $10^5$ , the  $\Delta K_{th,conv}$  decreases to lower values. This decrease reaches a maximum at  $n = 10^2$  in both steels in our study, and is associated with a mean increase in crack growth rate under periodic underloads.

This maximum increase in the mean crack growth rate at  $n = 10^2$  and  $K_{\max} = 11.11 \text{ MPa}\cdot\text{m}^{1/2}$  can be compared with the one at  $K_{\max} = 19.44 \text{ MPa}\cdot\text{m}^{1/2}$  in the 415 and 304L steels in Chapter 6. For this reason, crack growth rates for baseline cycles are measured at  $R = 0.7$  followed by periodic underloads at  $R = 0.1$  at  $K_{\max} = 19.44 \text{ MPa}\cdot\text{m}^{1/2}$  and  $n = 10^2$ . This increase in crack growth rate is compared with the one at  $K_{\max} = 11.11 \text{ MPa}\cdot\text{m}^{1/2}$  in both steels and is shown in Figure 8.3. As the  $\Delta K_{BL}$  decreases from 5.83 to 3.32  $\text{MPa}\cdot\text{m}^{1/2}$ , acceleration factors increase from 1.35 to 2.35, respectively in the 415 steel. This factor increases from 2.5 to 5 in the 304L steel, respectively. This shows that as  $K_{\max}$  and  $\Delta K_{BL}$  decrease towards  $\Delta K_{th,conv}$  at  $2 \times 10^{-7} \text{ mm/cycle}$ , periodic underloads at  $R = 0.1$  have a higher effect on baseline cycles at  $R = 0.7$ .

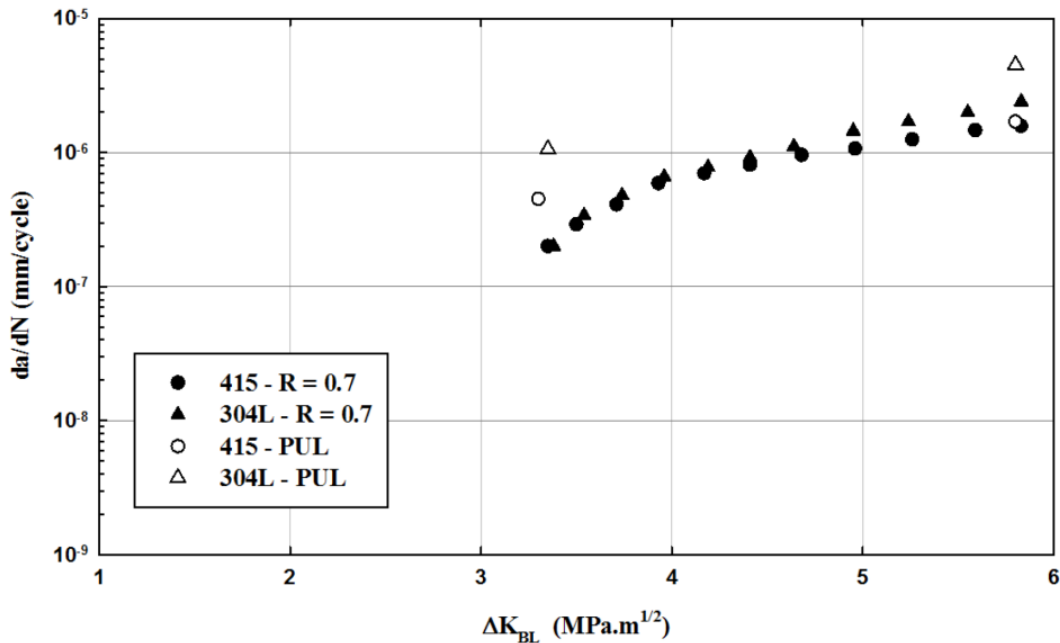


Figure 8.3 Log-linear of  $da/dN$  versus  $\Delta K_{BL}$  curve under CAL and PUL in the 415 and the 304L steels at  $n = 10^2$

In Chapter 7, the second load procedure is conducted at  $K_{max} = 11.11 \text{ MPa.m}^{1/2}$  under periodic underloads by increasing  $\Delta K_{BL}$  step-by-step to reach  $\Delta K_{th,true}$  and  $\Delta K_{th,conv}$ . This procedure shows that  $\Delta K_{th,true}$  under periodic underloads at  $6.7 \times 10^{-9} \text{ mm/cycle}$  is 5 times lower than the conventional one at  $2 \times 10^{-7} \text{ mm/cycle}$ . Therefore, it can be stated that the effect of periodic underloads is higher at lower crack growth rates. The first and second load procedures result in similar  $\Delta K_{th,conv}$  under periodic underloads.

The effect of  $K_{max}$  on crack growth rates under periodic underloads should also be investigated. For this reason, the proposed first and second load procedures in Chapter 7 are conducted at  $K_{max} = 19.44 \text{ MPa.m}^{1/2}$  and  $n = 10^3$ , and the results are compared to those obtained at  $K_{max} = 11.11 \text{ MPa.m}^{1/2}$ . For simplicity,  $K_{max}$  of  $11 \text{ MPa.m}^{1/2}$  and  $19.44 \text{ MPa.m}^{1/2}$  are hereafter called  $K_{max,1}$  and  $K_{max,2}$ .

It is complicated to define the true fatigue threshold,  $\Delta K_{th,true}$ , under periodic underloads at  $K_{max,2}$ . The crack path deflection increases at  $K_{max,2}$ , as a result the very low crack growth rates can increase or decrease depending on the crack path.

At  $K_{max,2}$ , crack is growing with underloads at  $\Delta K_{UL} = 17.49 \text{ MPa.m}^{1/2}$  with a growing rate equal to  $1.8 \times 10^{-8} \text{ mm/cycle}$  that does not increase as  $\Delta K_{BL}$  increases from zero to  $0.77 \text{ MPa.m}^{1/2}$ . A first increase in crack growth rate is detected at  $\Delta K_{BL} = 0.92 \text{ MPa.m}^{1/2}$ , however, it subsequently

decreases to that of underloads at  $\Delta K_{BL} = 1.33 \text{ MPa.m}^{1/2}$  (Figure 8.4). As  $\Delta K_{BL}$  increases to  $1.59 \text{ MPa.m}^{1/2}$ , the crack growth starts to increase continuously with  $\Delta K_{BL}$  until it reaches  $2 \times 10^{-7} \text{ mm/cycle}$ .

The  $\Delta K_{th,true}$  at  $K_{max,2}$  under constant amplitude loading stands between 2.54 and 2.66  $\text{MPa.m}^{1/2}$  at  $K_{max,2}$ , which is close to values at  $K_{max,1}$ . A first increase of the crack growth rates under periodic underloads leads to 67% decrease in  $\Delta K_{th,true}$  at  $K_{max,2}$  under constant amplitude loading. On the other hand, a continuous increase in the crack growth rates under periodic underloads leads to 44% decrease in  $\Delta K_{th,true}$  at  $K_{max,2}$  which is close to the 43% decrease in  $\Delta K_{th}$  at  $K_{max,1}$  (Figure 8.4).

As previously mentioned for the case of 415 steel, the conventional fatigue threshold,  $\Delta K_{th,conv}$ , under periodic underloads at  $K_{max,1}$  is 12% lower than the one under constant amplitude loading at  $K_{max,1}$  (3.12 versus 3.32  $\text{MPa.m}^{1/2}$ ). This value at  $K_{max,2}$  is 14% lower than the one under constant amplitude loading (2.66 versus 3.12  $\text{MPa.m}^{1/2}$ ).

Similar results are obtained in the 304L steel, the true fatigue threshold under constant amplitude loading is equal to 2.48  $\text{MPa.m}^{1/2}$  and 2.70  $\text{MPa.m}^{1/2}$  at  $K_{max,2}$ . The first increase of the crack growth of the underloads leads to 74% decrease in the  $\Delta K_{th,true}$  at  $K_{max,2}$ . On the other hand, a continuous increase in the crack growth rates leads to 62% decrease in the  $\Delta K_{th,true}$  which is close to 63% decrease in  $\Delta K_{th}$  at  $K_{max,1}$  (Figure 8.5).

The conventional fatigue thresholds,  $\Delta K_{th,conv}$ , at  $K_{max,1}$  is 15% lower than the one under constant amplitude loading (3.09 versus 3.35  $\text{MPa.m}^{1/2}$ ). The conventional fatigue threshold under periodic underloads at  $K_{max,2}$  is 19% lower than the one under constant amplitude loading (2.52 versus 3.09  $\text{MPa.m}^{1/2}$ ).

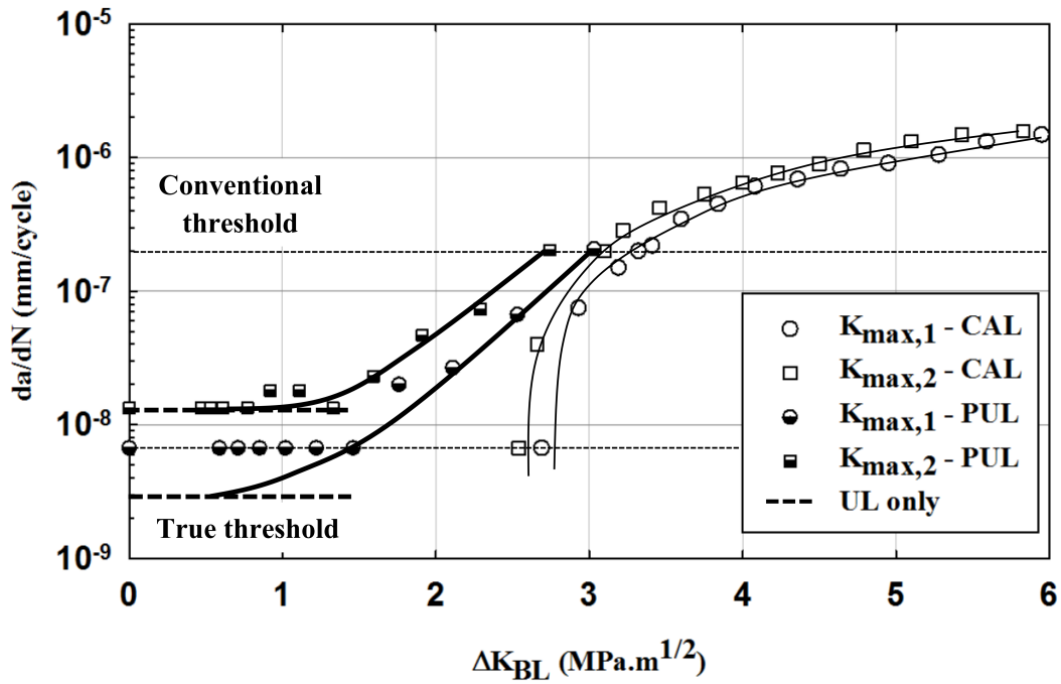


Figure 8.4 Crack growth rates versus linear  $\Delta K_{BL}$  from different test procedures under CAL and PUL in 415 steel

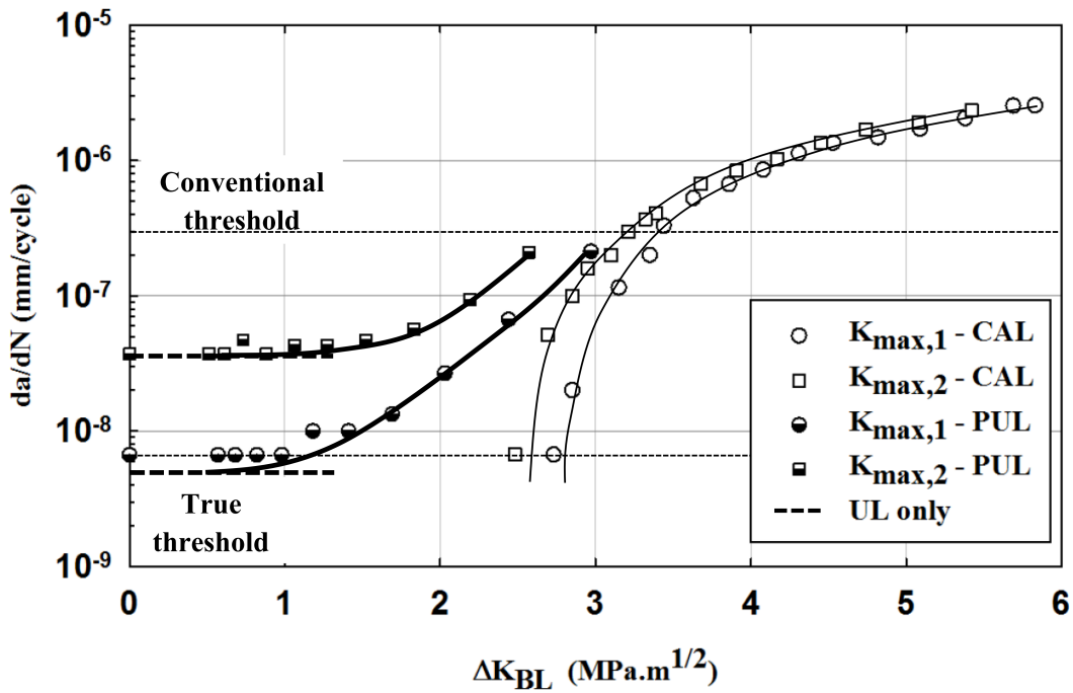


Figure 8.5 Crack growth rates versus linear  $\Delta K_{BL}$  from different test procedures under CAL and PUL in 304L steel

## CHAPTER 9 CONCLUSION AND RECOMMENDATIONS

### 9.1 Conclusions

In the 415 steel, crack growth rates versus  $\Delta K$  under constant amplitude loading at  $R = 0.1$  are lower than the ones in the 304L steel in the Paris region. As  $\Delta K$  approaches  $\Delta K_{th,conv}$  in the near-threshold region, crack closure levels increase in both steels and the crack growth rates versus the estimated  $\Delta K_{eff}$  become close to each other. It is presumed that crack closure is mainly induced by crack path irregularities in the 415 steel and mainly induced by plasticity in the 304L.

Crack growth rates and  $\Delta K_{th,conv}$  at  $R = 0.7$  are close together in both steels. An increase in  $K_{max}$  slightly decreases the conventional and real fatigue thresholds in both steels.

In the first study, it can be concluded that crack growth due to POVs and SS sequences can be linearly summed using the LDS prediction in the Paris region for the 415 steel; however, a maximum acceleration factor of 1.5 and 2.5 should be considered in the LDS prediction for the A516 and 304L steel, respectively. Increase in the monotonous strain hardening in turbine runner steels increases acceleration factors.

Fractography analysis revealed that an underload followed by the baseline cycles causes an increase in the crack growth during baseline cycles, which leads to higher acceleration factors.

It is presumed that a combination of high tensile residual stress and slow decrease of this stress after an underload can be one cause of this faster crack growth. Moreover, strain hardening induced by periodic underloads can decrease ductility at the crack tip, also leading to higher crack growth during subsequent baseline cycles.

In the second study, periodic underloads do not decrease the fatigue threshold of small cycles (baseline cycles) above  $n = 1.25 \times 10^5$ . In turbine runners, the number of small cycles is around  $7 \times 10^{10}$  during the 70 years of design life. As a result, in order to avoid a decrease in the fatigue threshold, the number of start/stop sequences or other large cycles (periodic underloads) should be kept below  $5 \times 10^5$ .

Periodic underloads applied below  $n = 1.25 \times 10^5$  decrease the conventional fatigue threshold measured at  $2 \times 10^{-7}$  mm/cycle. This decrease is higher in the 304L steel as compared to 415 steel. According to the second load procedure,  $\Delta K_{th,true}$  under constant amplitude loading decreases by 43% and 61% due to periodic underloads at  $n = 1.25 \times 10^3$  in the 415 and 304L steels, respectively,

as compared to 9% and 12% decreases in  $\Delta K_{th,conv}$ . The decreases in the conventional fatigue thresholds due to periodic underloads following the first and second procedures are similar.

Tensile residual stress is induced in runners during the fabrication and welding. This leads to an increase in  $K_{max}$  level at the tip of the defects in runners and may propagate them. At  $K_{max,2}$ , the conventional fatigue threshold decreases by 8% and 9% in the in the 415 and 304L steels. As the crack growth rates decrease, the decrease in  $\Delta K_{th,true}$  corresponds to 10% and 12%, respectively. There is a similar decrease in the conventional and real fatigue threshold due to periodic underloads or large cycles at  $K_{max,1}$  and  $K_{max,2}$ .

## 9.2 Further recommendations

In the turbine runners stress spectrum, a startup and a spin-no-load (SNL) occur before reaching the maximum stress. The startup and SNL are shown in Figure 9.1 in a repeated start/stop sequence (sequence A). It was assumed that both types of stress do not induce a crack growth at the beginning of the stress spectrum. Consequently, they were neglected, and the effect of interaction between small stress cycles and SS sequences on crack growth was investigated in Chapter 6; however, some studies have considered that periodic startups can induce crack growth [155]. Consequently, it was suggested to decrease the maximum stress reached by periodic startups [155]. This raises the question about what the maximum stress level that periodic startups and the SNL can reach without inducing crack growth is. A test procedure can be conducted to address this question.

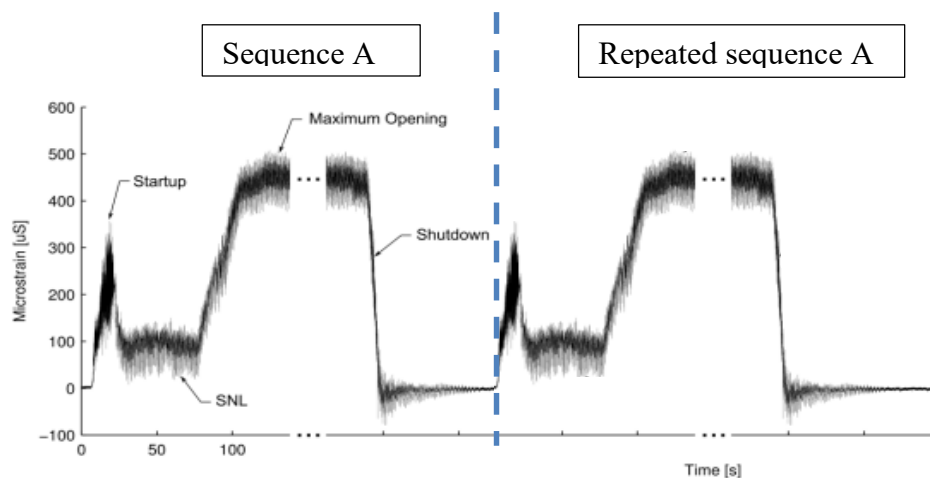


Figure 9.1 Startup and SNL in an operating turbine runner with a repeated sequence

A general stress spectrum in hydraulic turbine runners mainly consists of small cycles, power out variations (POVs), and start/stop (SS) sequences [154]. Therefore, the interaction between three aforementioned stress cycles on crack growth could have been studied; however, the stress spectra were simplified to investigate and understand the effect of two stress cycles on crack growth in two studies. By considering the results and test procedures proposed in this study, we recommend that future studies investigate the interaction between three stress cycles on crack growth and fatigue threshold of small cycles as shown in Figure 9.2.

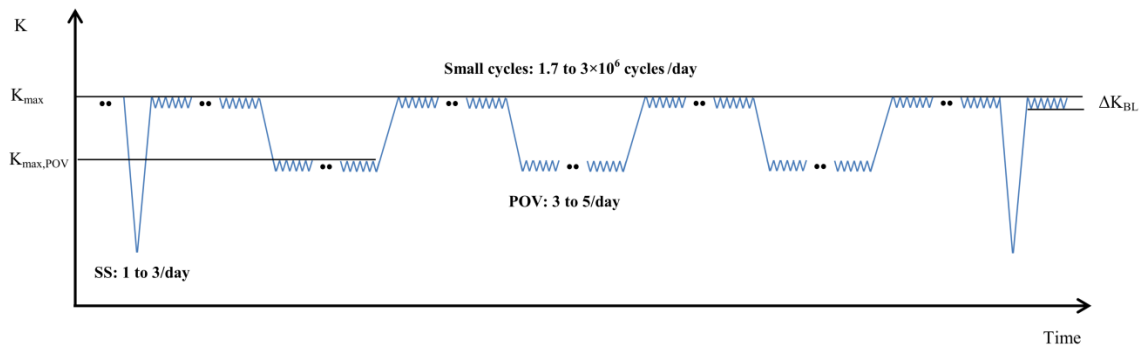


Figure 9.2 Stress spectrum with three stress cycles imposed at the defect tip

As previously mentioned, as crack growth in a load block,  $\Delta a_{\text{block}}$ , decreases and becomes of the same order of magnitude as underload cyclic plastic zone,  $r_{\text{yc}}$ , the  $\Delta K_{\text{th,conv}}$  under constant amplitude loading starts to decrease. This indicates that the mean crack growth rate of baseline cycles starts to increase. A prediction model to predict the decrease in  $\Delta K_{\text{th,conv}}$  and increase in the mean crack growth rate as a function of the  $\Delta a_{\text{block}}$  over  $r_{\text{yc}}$  can be studied and proposed in future works.

## REFERENCES

- [1] H. Huth, "Fatigue design of hydraulic turbine runners," PhD thesis, Norwegian University of Science and Technology, 2005.
- [2] G. Franke, C. Powell, R. Fisher, U. Seidel, and J. Koutnik, "On pressure mode shapes arising from rotor/stator interactions," *Sound and Vibration*, vol. 39, no. 3, pp. 14-18, 2005.
- [3] B. Nennemann, T. Vu, and M. Farhat, "CFD prediction of unsteady wicket gate-runner interaction in Francis turbines: A new standard hydraulic design procedure," in *HYDRO 2005*, 2005.
- [4] M. Sabourin, J. L. Gagné, S. Giroux, A. St-Hilaire, and J. de la Bruere Terrault, "Mechanical loads and fatigue analysis of a Francis runner," *Hydro Vision*, 2004.
- [5] C. Trivedi, B. Gandhi, and C. J. Michel, "Effect of transients on Francis turbine runner life: a review," *Journal of Hydraulic Research*, vol. 51, no. 2, pp. 121-132, 2013.
- [6] T. L. Anderson, *Fracture Mechanics: Fundamentals and Applications*, 3th ed. CRC press, pp. 12-13, 2005.
- [7] R. I. Stephens, A. Fatemi, R. R. Stephens, and H. O. Fuchs, *Metal fatigue in engineering*. John Wiley & Sons, 2000.
- [8] A. Coutu, M. D. Roy, C. Monette, and B. Nennemann, "Experience with rotor-stator interactions in high head Francis runner," *Proceedings of 24th IAHR symposium on hydraulic machinery and systems at Foz do Iguassu, Brazil*, 2008.
- [9] ASTM.E1823, "Standard Terminology Relating to Fatigue and Fracture Testing," 2012.
- [10] R. I. Stephens, A. Fatemi, R. R. Stephens, and H. O. Fuchs, *Metal fatigue in engineering*, 2nd ed. New York ; Toronto: Wiley, pp. 67-69, 2001.
- [11] S. Suresh, *Fatigue of materials*, 2nd ed. Cambridge University Press, pp. 322-326, 1998.
- [12] R. W. Hertzberg, "Deformation and fracture mechanics of engineering materials," 1989.
- [13] T. L. Anderson, *Fracture Mechanics: Fundamentals and Applications*, 3th ed. CRC press, pp. 513-514, 2005.
- [14] J. Schijve, *Fatigue of structures and materials*. Kluwer Academic Pub, 2001.

- [15] K. Walker, "The effect of stress ratio during crack propagation and fatigue for 2024-T3 and 7075-T6 aluminum," *Effects of environment and complex load history on fatigue life*, ASTM STP 462, pp. 1-14, 1970.
- [16] N. Dowling, *Mechanical Behavior of Materials* (USA). pp. 421-427, 2007.
- [17] C. Bathias and A. Pineau, *Fatigue des matériaux et des structures. 1, Introduction, endurance, amorçage et propagation des fissures, fatigue oligocyclique et gigacyclique* (Mécanique et ingénierie des matériaux). Paris: Hermès Science, 2008.
- [18] K. Tanaka, "Mechanics and micromechanics of fatigue crack propagation," *Fracture mechanics: perspectives and directions (twentieth symposium)*, ASTM STP 1020, pp. 151-183, 1989.
- [19] C. Bathias and A. Pineau, *Fatigue des matériaux et des structures. 2, Fissures courtes, mécanismes et approche locale, fatigue-corrosion et effet de l'environnement, chargements d'amplitude variable* (Mécanique et ingénierie des matériaux). Paris: Hermès science : Lavoisier, pp. 17-19, 2008.
- [20] R. Ritchie and J. Lankford, "Small fatigue cracks: a statement of the problem and potential solutions," *Materials Science and Engineering*, vol. 84, pp. 11-16, 1986.
- [21] D. Broek, *Elementary Engineering Fracture Mechanics*, 4th ed. Martinus Nijhoff, pp. 441-446, 1986.
- [22] D. Broek, *The Practical Use of Fracture Mechanics*, 2nd ed. Kluwer Academic Publishers, pp. 226-228, 1988.
- [23] G. R. Irwin, "Analysis of stresses and strains near the end of a crack traversing a plate," *Trans. ASME Journal of Applied Mechanics*, vol. 24, pp. 361-364, 1957.
- [24] J. Schijve, *Fatigue of Structures and Materials* (The Netherlands: Kluwer Academic Publishers). 2001.
- [25] R. O. Ritchie and S. Suresh, "Some considerations on fatigue crack closure at near-threshold stress intensities due to fracture surface morphology," *Metallurgical Transactions A*, vol. 13, no. 5, pp. 937-940, 1982.
- [26] M. Williams, "The bending stress distribution at the base of a stationary crack," *Journal of Applied Mechanics*, vol. 28, no. 1, pp. 78-82, 1961.

- [27] D. Dugdale, "Yielding of steel sheets containing slits," *Journal of the Mechanics and Physics of Solids*, vol. 8, no. 2, pp. 100-104, 1960.
- [28] J. Rice, "Mechanics of crack tip deformation and Extension by fatigue," *Fatigue crack propagation, ASTM STP 415*, pp. 247-311, 1966.
- [29] R. McClung, "The influence of applied stress, crack length, and stress intensity factor on crack closure," *Metallurgical and Materials Transactions A*, vol. 22, no. 7, pp. 1559-1571, 1991.
- [30] B. Budiansky and J. Hutchinson, "Analysis of closure in fatigue crack growth," *Journal of Applied Mechanics*, vol. 45, no. 2, pp. 267-276, 1978.
- [31] R. Ritchie, "Near-threshold fatigue-crack propagation in steels," *International Materials Reviews*, vol. 24, no. 1, pp. 205-230, 1979.
- [32] R. Bucci, "Development of a proposed ASTM standard test method for near-threshold fatigue crack growth rate measurement," *Fatigue crack growth measurement and data analysis, ASTM STP 738*, no. 738, pp. 5-28, 1981.
- [33] P. Paris, M. Gomez, and W. Anderson, "Rational Analytic Theory of Fatigue," *Trend in Engineering* vol. 13, pp. 9-14, 1961.
- [34] R. Ritchie, "Influence of microstructure on near-threshold fatigue-crack propagation in ultra-high strength steel," *Metal Science*, vol. 11, no. 8-9, pp. 8-9, 1977.
- [35] C. van Kranenburg, W. He, J. Zuidema, and F. Veer, "Influence of measurement method on fatigue crack growth threshold," in *ECF15, Stockolm* 2004.
- [36] W. Herman, R. Hertzberg, and R. Jaccard, "A simplified laboratory approach for the prediction of short crack behavior in engineering structures," *Fatigue & Fracture of Engineering Materials & Structures*, vol. 11, no. 4, pp. 303-320, 1988.
- [37] R. Hertzberg, W. A. Herman, T. Clark, and R. Jaccard, "Simulation of short crack and other low closure loading conditions utilizing constant  $K_{max}$   $\Delta K$ -decreasing fatigue crack growth procedures," *Small-crack Test Methods, ASTM STP 1149*, vol. 1149, pp. 197-220, 1992.
- [38] D. Taylor, *Fatigue thresholds*. Butterworth-Heinemann, pp. 170-172, 1989.

- [39] R. Vecchio, R. Hertzberg, and R. Jaccard, "Overload induced crack growth rate attenuation behavior in aluminium alloys," *Scripta Metallurgica*, vol. 17, no. 3, pp. 343-346, 1983.
- [40] J. Masounave and J. P. Bailon, "Dependence of the Threshold Stress Intensity Factor on the Cyclic Stress Ratio in Fatigue of Ferritic-Pearlitic Steels," *Scripta Metallurgica*, vol. 9, no. 7, pp. 723-730, 1975.
- [41] J. Masounave and J. P. Bailon, "Effect of grain size on the threshold stress intensity factor in fatigue of a ferritic steel," *Scripta Metallurgica*, vol. 10, no. 2, pp. 165-170, 1976.
- [42] O. Vosikovsky, "The effect of stress ratio on fatigue crack growth rates in steels," *Engineering Fracture Mechanics*, vol. 11, no. 3, pp. 595-602, 1979.
- [43] J. Schijve, "Fatigue crack closure: observations and technical significance," *Mechanics of Fatigue Crack Closure, ASTM STP 982*, pp. 5-34, 1988.
- [44] W. Elber, "Fatigue crack closure under cyclic tension," *Engineering Fracture Mechanics*, vol. 2, no. 1, pp. 37-45, 1970.
- [45] W. Elber, "The significance of fatigue crack closure," *Damage tolerance in aircraft structures, ASTM STP 486*, pp. 230-242, 1971.
- [46] J. Newman Jr, "Prediction of fatigue crack growth under variable-amplitude and spectrum loading using a closure model," *Design of fatigue and fracture resistant structures, ASTM STP 761*, pp. 255-277, 1982.
- [47] J. C. Newman Jr, "A crack-closure model for predicting fatigue crack growth under aircraft spectrum loading," *Methods and models for predicting fatigue crack growth under random loading, ASTM STP 748*, pp. 53-84, 1981.
- [48] P. Bernard, T. Lindley, and C. Richards, "Mechanisms of overload retardation during fatigue crack propagation," *Fatigue crack growth under spectrum loads, ASTM STP 595*, pp. 78-97, 1976.
- [49] J. Telesman and D. M. Fisher, "Influence of fatigue crack wake length and state of stress on crack closure," *NASA Tech. Memo.*, p. 25, 1986.
- [50] E. Hornbogen, "Martensitic transformation at a propagating crack," *Acta Metallurgica*, vol. 26, no. 1, pp. 147-152, 1978.

- [51] A. Pineau and R. Pelloux, "Influence of strain-induced martensitic transformations on fatigue crack growth rates in stainless steels," *Metallurgical and Materials Transactions B*, vol. 5, no. 5, pp. 1103-1112, 1974.
- [52] D. A. Porter, K. E. Easterling, and M. Sherif, *Phase Transformations in Metals and Alloys, (Revised Reprint)*. CRC press, 2009.
- [53] J. Bressanelli and A. Moskowitz, "Effects of strain rate, temperature, and composition on tensile properties of metastable austenitic stainless steels," *ASM Trans Quart*, vol. 59, no. 2, pp. 223-239, 1966.
- [54] D. Thibault, P. Bocher, M. Thomas, J. Lanteigne, P. Hovington, and P. Robichaud, "Reformed austenite transformation during fatigue crack propagation of 13%Cr-4%Ni stainless steel," *Materials Science and Engineering: A*, vol. 528, no. 21, pp. 6519-6526, 2011.
- [55] Z. Khan and M. Ahmed, "Stress-induced martensitic transformation in metastable austenitic stainless steels: Effect on fatigue crack growth rate," *Journal of Materials Engineering and Performance*, vol. 5, no. 2, pp. 201-208, 1996.
- [56] A. W. Thompson, "Fatigue crack propagation in austenitic stainless steels," *Engineering Fracture Mechanics*, vol. 7, no. 1, pp. 61-66, IN7-IN8, 67-68, 1975.
- [57] A. McEvily, W. Zagran, J. Gonzalez, and S. Matsuoka, "Fatigue crack growth in type 304 stainless steel," *Materials science monographs*, vol. 46, pp. 271-279, 1988.
- [58] S. Suresh, "Fatigue crack deflection and fracture surface contact: micromechanical models," *Metallurgical Transactions A*, vol. 16, no. 1, pp. 249-260, 1985.
- [59] S. Suresh, "Micromechanisms of fatigue crack growth retardation following overloads," *Engineering Fracture Mechanics*, vol. 18, no. 3, pp. 577-593, 1983.
- [60] R. Ritchie, "Mechanisms of fatigue crack propagation in metals, ceramics and composites: role of crack tip shielding," *Materials Science and Engineering: A*, vol. 103, no. 1, pp. 15-28, 1988.
- [61] C. Beevers, "Fatigue crack growth characteristics at low stress intensities of metals and alloys," *Metal Science*, vol. 11, no. 8-9, pp. 8-9, 1977.

- [62] C. Beevers, "Some aspects of the influence of microstructure and environment on  $\Delta K$  thresholds," *Fatigue Thresholds*, pp. 257-275, 1981.
- [63] R. A. Schmidt and P. C. Paris, "Threshold for fatigue crack propagation and the effects of load ratio and frequency," ASTM STP 536, pp. 79-94, 1973.
- [64] *ASTM.E407, Standard Practice for Microetching Metals and Alloys*, 2011.
- [65] K. Minakawa, G. Levan, and A. McEvily, "The influence of load ratio on fatigue crack growth in 7090-T6 and IN9021-T4 P/M aluminum alloys," *Metallurgical and Materials Transactions A*, vol. 17, no. 10, pp. 1787-1795, 1986.
- [66] D.-L. Chen, B. Weiss, and R. Stickler, "A new evaluation procedure for crack closure," *International journal of fatigue*, vol. 13, no. 4, pp. 327-331, 1991.
- [67] M. Halliday and C. Beevers, "Some aspects of fatigue crack closure in two contrasting titanium alloys," *Journal of Testing and Evaluation*, vol. 9, pp. 195-201, 1981.
- [68] M. A. Sutton, W. Zhao, S. R. McNeill, J. D. Helm, R. S. Piascik, and W. T. Riddell, "Local crack closure measurements: Development of a measurement system using computer vision and a far-field microscope," in *Advances in fatigue crack closure measurement and analysis: second volume, ASTM STP 1343*, pp. 145-156, 1999.
- [69] W. Riddell, R. Piascik, M. Sutton, W. Zhao, S. McNeill, and J. Helm, "Determining fatigue crack opening loads from near-crack-tip displacement measurements," in *Advances in Fatigue Crack Closure Measurement and Analysis: Second Volume*, ASTM STP 1343, pp. 157-174, 1999.
- [70] J. M. Larsen, J. C. Williams, and A. W. Thompson, "Crack-closure effects on the growth of small surface cracks in titanium-aluminum alloys," in *Mechanics of Fatigue Crack Closure*: ASTM International, ASTM STP 982, pp. 149-167, 1988.
- [71] S. Hudak and D. L. Davidson, "The dependence of crack closure on fatigue loading variables," in *Mechanics of Fatigue Crack Closure*, ASTM STP 982, pp. 121-139, 1988.
- [72] J. E. Allison, R. C. Ku, and M. A. Pompetzki, "A comparison of measurement methods and numerical procedures for the experimental characterization of fatigue crack closure," in *Mechanics of Fatigue Crack Closure*, ASTM STP 982, pp. 171-185, 1988.

- [73] H. O. Liknes and R. R. Stephens, "Effect of geometry and load history on fatigue crack growth in Ti-62222," in *Fatigue Crack Growth Thresholds, Endurance Limits, and Design*, ASTM STP 1372, pp. 175-191, 2000.
- [74] P. C. Paris, H. Tada, and J. K. Donald, "Service load fatigue damage—a historical perspective," *International journal of fatigue*, vol. 21, pp. S35-S46, 1999.
- [75] N. Fleck, "Influence of stress state on crack growth retardation," *Basic Questions in Fatigue.*, vol. 1, pp. 157-183, 1984.
- [76] D. Chen, B. Weiss, and R. Stickler, "Effect of stress ratio and loading condition on the fatigue threshold," *International journal of fatigue*, vol. 14, no. 5, pp. 325-329, 1992.
- [77] D. Chen, B. Weiss, and R. Stickler, "Contribution of the cyclic loading portion below the opening load to fatigue crack growth," *Materials Science and Engineering: A*, vol. 208, no. 2, pp. 181-187, 1996.
- [78] D. Chen, B. Weiss, and R. Stickler, "A model for crack closure," *Engineering Fracture Mechanics*, vol. 53, no. 4, pp. 493-509, 1996.
- [79] J. K. Donald, "Introducing the compliance ratio concept for determining effective stress intensity," *International journal of fatigue*, vol. 19, no. 93, pp. 191-195, 1997.
- [80] C. D. Carman, C. C. Turner, and B. M. Hillberry, "A method for determining crack opening load from load-displacement data," in *Mechanics of Fatigue Crack Closure*, ASTM STP 982, pp. 214-221, 1988.
- [81] W. Yisheng and J. Schijve, "Fatigue crack closure measurements on 2024-T3 sheet specimens " *Fatigue & Fracture of Engineering Materials & Structures*, vol. 18, no. 9, pp. 917-921, 1995.
- [82] K. Donald and P. C. Paris, "An evaluation of  $\Delta K_{eff}$  estimation procedures on 6061-T6 and 2024-T3 aluminum alloys," *International journal of fatigue*, vol. 21, pp. S47-S57, 1999.
- [83] G. H. Bray and J. K. Donald, "Separating the influence of  $K_{max}$  from closure-related stress ratio effects using the adjusted compliance ratio technique," in *Advances in Fatigue Crack Closure Measurement and Analysis: Second Volume*, ASTM STP 1343, pp. 57-79, 1999.

- [84] D. Kujawski, "Methods for crack opening load and crack tip shielding determination: a review," *Fatigue & Fracture of Engineering Materials & Structures*, vol. 26, no. 11, pp. 1053-1067, 2003.
- [85] Y. Yamada and J. Newman, "Crack-closure behavior of 2324-T39 aluminum alloy near-threshold conditions for high load ratio and constant  $K_{max}$  tests," *International Journal of Fatigue*, vol. 31, no. 11, pp. 1780-1787, 2009.
- [86] R. Hertzberg, C. Newton, and R. Jaccard, "Crack closure: correlation and confusion," *Mechanics of fatigue crack closure, ASTM STP 982*, pp. 139-148, 1988.
- [87] A. Vasudevan, K. Sadananda, and N. Louat, "Reconsideration of fatigue crack closure," *Scripta metallurgica et materialia*, vol. 27, pp. 1673-1678, 1992.
- [88] A. Vasudevan and K. Sadananda, "Classification of fatigue crack growth behavior," *Metallurgical and Materials Transactions A*, vol. 26, no. 5, pp. 1221-1234, 1995.
- [89] R. Pippan, H. Stüwe, and K. Golos, "A comparison of different methods to determine the threshold of fatigue crack propagation," *International journal of fatigue*, vol. 16, no. 8, pp. 579-582, 1994.
- [90] A. Noroozi, G. Glinka, and S. Lambert, "A two parameter driving force for fatigue crack growth analysis," *International journal of fatigue*, vol. 27, no. 10, pp. 1277-1296, 2005.
- [91] A. Noroozi, G. Glinka, and S. Lambert, "A study of the stress ratio effects on fatigue crack growth using the unified two-parameter fatigue crack growth driving force," *International journal of fatigue*, vol. 29, no. 9, pp. 1616-1633, 2007.
- [92] G. Marci, "Effect of the active plastic zone on fatigue crack growth rates," in *Fracture Mechanics: Proceedings of the Eleventh National Symposium on Fracture Mechanics: Part I*, ASTM STP 677, pp. 168-186, 1979.
- [93] H. Döker and G. Marci, "Threshold range and opening stress intensity factor in fatigue," *International journal of fatigue*, vol. 5, no. 4, pp. 187-191, 1983.
- [94] G. Marci, "The  $\Delta K$  eff-concept: A unique and complete description of fatigue crack propagation," *Engineering Fracture Mechanics*, vol. 55, no. 1, pp. 95-114, 1996.
- [95] S. D. Antolovich, A. Saxena, and G. R. Chanani, "A model for fatigue crack propagation," *Engineering Fracture Mechanics*, vol. 7, no. 4, pp. 649-652, 1975.

- [96] H. Neuber, "Theory of stress concentration for shear-strained prismatical bodies with arbitrary nonlinear stress-strain law," *Journal of Applied Mechanics*, vol. 28, pp. 544-549, 1961.
- [97] G. Dieter, E., *Mechanical Metallurgy*, 3rd ed. McGraw-Hill, pp. 287-288, 1986.
- [98] S. Majumdar and J. Morrow, "Correlation between fatigue crack propagation and low cycle fatigue properties," *Fracture toughness and slow-stable cracking, ASTM STP 559*, pp. 159-182, 1974.
- [99] K. Smith, T. Topper, and P. Watson, "A stress-strain function for the fatigue of metals (Stress-strain function for metal fatigue including mean stress effect)," *Journal of materials*, vol. 5, pp. 767-778, 1970.
- [100] G. Glinka, "A notch stress-strain analysis approach to fatigue crack growth," *Engineering Fracture Mechanics*, vol. 21, no. 2, pp. 245-261, 1985.
- [101] R. G. Forman, V. Kearney, and R. Engle, "Numerical analysis of crack propagation in cyclic-loaded structures," *Journal of Basic Engineering*, vol. 89, no. 3, pp. 459-463, 1967.
- [102] A. McEvily, "Current aspects of fatigue," *Metal Science*, vol. 11, no. 8-9, pp. 274-284, 1977.
- [103] M. Skorupa, "Load interaction effects during fatigue crack growth under variable amplitude loading—a literature review. Part II: qualitative interpretation," *Fatigue & Fracture of Engineering Materials & Structures*, vol. 22, no. 10, pp. 905-926, 1999.
- [104] K. D. Singh, M. R. Parry, and I. Sinclair, "Variable amplitude fatigue crack growth behavior—a short overview," *Journal of mechanical science and technology*, vol. 25, no. 3, pp. 663-673, 2011.
- [105] W. Geary, "A review of some aspects of fatigue crack growth under variable amplitude loading," *International Journal of Fatigue*, vol. 14, no. 6, pp. 377-386, 1992.
- [106] R. I. Stephens, D. K. Chen, and B. W. Hom, "Fatigue crack growth with negative stress ratio following single overloads in 2024-T3 and 7075-T6 aluminum alloys," *Fatigue crack growth under spectrum loads, ASTM STP 595*, 1976.
- [107] E. Von Euw, R. Hertzberg, and R. Roberts, "Delay effects in fatigue crack propagation," *stress analysis and growth of cracks: proceedings of the 1971 national symposium on fracture mechanics: part 1, ASTM STP 513*, pp. 230-259, 1972.

- [108] M. Skorupa, "Load interaction effects during fatigue crack growth under variable amplitude loading—a literature review. Part I: empirical trends," *Fatigue & Fracture of Engineering Materials & Structures*, vol. 21, no. 8, pp. 987-1006, 1998.
- [109] W. J. Mills and R. W. Hertzberg, "Load interaction effects on fatigue crack propagation in 2024-T3 aluminum alloy," *Engineering Fracture Mechanics*, vol. 8, no. 4, pp. 657-664, IN15-IN16, 665-667, 1976.
- [110] C. Ward-Close and R. Ritchie, "On the Role of Crack Closure Mechanisms in Influencing Fatigue Crack Growth Following Tensile Overloads in a Titanium Alloy: Near Threshold Versus Higher AK Behavior," *Mechanics of Fatigue Crack Closure*, ASTM STP 982, pp. 93-111, 1988.
- [111] D. M. Shuter and W. Geary, "Some aspects of fatigue crack growth retardation behaviour following tensile overloads in a structural steel," *Fatigue & Fracture of Engineering Materials & Structures*, vol. 19, no. 2 - 3, pp. 185-199, 1996.
- [112] Y. K. Tür and Ö. Vardar, "Periodic tensile overloads in 2024-T3 Al-alloy," *Engineering Fracture Mechanics*, vol. 53, no. 1, pp. 69-77, 1996.
- [113] S. Hopkins and C. Rau, "Effect of Various Programmed Overloads on the Threshold for High-Frequency Fatigue Crack Growth," *Fatigue Crack Growth Under Spectrum Loads*, ASTM STP 595, pp. 125-141, 1976.
- [114] E. Zaiken and R. Ritchie, "On the development of crack closure and the threshold condition for short and long fatigue cracks in 7150 aluminum alloy," *Metallurgical and Materials Transactions A*, vol. 16, no. 8, pp. 1467-1477, 1985.
- [115] Ö. Vardar and N. Yildirim, "Crack growth retardation due to intermittent overloads," *International Journal of Fatigue*, vol. 12, no. 4, pp. 283-287, 1990.
- [116] N. A. Fleck, "Fatigue crack growth due to periodic underloads and overloads," *Acta Metallurgica*, vol. 33, no. 7, pp. 1339-1354, 1985.
- [117] N. Ohrloff, A. Gysler, and G. Lutjering, "Fatigue crack propagation behaviour under variable amplitude loading," *Fatigue Crack Growth Under Variable Amplitude Loading (edited by J. Petit, D. L. Davidson, S. Suresh and P. Rabbe)*, Elsevier Applied Science, London, pp. 24-34, 1988.

- [118] C. Robin, M. L. Busch, M. Chergui, H. P. Lieurade, and G. Pluvinage, "Influence of series of tensile and compressive overloads on 316L crack growth," *Fatigue Crack Growth Under Variable Amplitude Loading*, pp. 87-97, 1988.
- [119] M. L. Busch and J. L. Lebrun, "X-ray diffraction study of stress distributions following a single tensile overload," *Fatigue Crack Growth Under Variable Amplitude Loading*, pp. 76-86, 1988.
- [120] T. H. Topper and M. T. Yu, "The effect of overloads on threshold and crack closure," *International Journal of Fatigue*, vol. 7, no. 3, pp. 159-164, 1985.
- [121] K. T. V. Rao and R. Ritchie, "Mechanisms for the Retardation of Fatigue Cracks Following Single Tensile Overloads Behavior in Aluminum-Lithium Alloys," 1988.
- [122] J. Schijve, "Fatigue cracks, plasticity effects and crack closure," *Engineering Fracture Mechanics*, vol. 11, no. 1, pp. 182-196, 1979.
- [123] K. Venkateswara Rao and R. Ritchie, "Micromechanisms of transient fatigue crack growth behaviour in aluminium-lithium alloys following single tensile overloads," *Fatigue crack growth under variable amplitude loading. London: Elsevier Applied Science*, pp. 134-145, 1988.
- [124] C. S. Shin and S. H. Hsu, "On the mechanisms and behaviour of overload retardation in AISI 304 stainless steel," *International journal of fatigue*, vol. 15, no. 3, pp. 181-192, 1993.
- [125] J. Schijve, "The effect of pre-strain on fatigue crack growth and crack closure," *Engineering Fracture Mechanics*, vol. 8, no. 4, pp. 575-581, 1976.
- [126] R. E. Jones, "Fatigue crack growth retardation after single-cycle peak overload in Ti-6Al-4V titanium alloy," *Engineering Fracture Mechanics*, vol. 5, no. 3, pp. 585-604, 1973.
- [127] J. F. Knott and A. C. Pickard, "Effects of overloads on fatigue-crack propagation: aluminium alloys," *Metal Science*, vol. 11, no. 8-9, pp. 8-9, 1977.
- [128] M. T. Yu, T. H. Topper, and P. Au, "The Effects of Stress Ratio, Compressive Load and Underload on the Threshold Behavior of a 2024-T 351 Aluminium Alloy," *Proceedings of the 2nd Conference on Fatigue and Fracture Thresholds*, vol. 1, pp. 179-190, 1984.

- [129] A. A. Dabayeh, R. X. Xu, B. P. Du, and T. H. Topper, "Fatigue of cast aluminium alloys under constant and variable-amplitude loading," *International journal of fatigue*, vol. 18, no. 2, pp. 95-104, 1996.
- [130] D. Damri, "The effect of underload cycling on the fatigue threshold in a structural steel," *Scripta metallurgica et materialia*, vol. 25, no. 2, pp. 283-288, 1991.
- [131] D. Damri, "Some observations on the cyclic unloading effects of a fatigue crack," *International journal of fatigue*, vol. 13, no. 3, pp. 271-277, 1991.
- [132] Y. Lenets and T. Nicholas, "Load history dependence of fatigue crack growth thresholds for a Ti-alloy," *Engineering Fracture Mechanics*, vol. 60, no. 2, pp. 187-203, 1998.
- [133] R. Koterazawa, Y. Qinsheng, W. Tian-jian, and T. Nosh, "Acceleration of fatigue crack growth under intermittent overstressing with different mean stress levels," *Fatigue & Fracture of Engineering Materials & Structures*, vol. 17, no. 9, pp. 1033-1041, 1994.
- [134] R. Koterazawa and T. Nosh, "Acceleration of crack growth under intermittent overstressing in different environments," *Fatigue & Fracture of Engineering Materials & Structures*, vol. 15, no. 1, pp. 103-113, 1992.
- [135] E. Zaiken and R. Ritchie, "On the role of compression overloads in influencing crack closure and the threshold condition for fatigue crack growth in 7150 aluminum alloy," *Engineering Fracture Mechanics*, vol. 22, no. 1, pp. 35-48, 1985.
- [136] T. H. Topper, D. L. DuQuesnay, and M. A. Pompetzki, "Crack closure, damage, and short crack growth under variable amplitude loading," *Theoretical Concept and Numerical Analysis of Fatigue*, pp. 201-235, 25-27 May, 1992.
- [137] R. L. Carlson and G. A. Kardomateas, "Effects of compressive load excursions on fatigue crack growth," *International journal of fatigue*, vol. 16, no. 2, pp. 141-146, 1994.
- [138] R. Yang, "Prediction of crack growth under complex loading cycles," *International journal of fatigue*, vol. 16, no. 6, pp. 397-402, 1994.
- [139] M. A. Miner, "Cumulative damage in fatigue," *Journal of Applied Mechanics*, vol. 12, no. 3, pp. 159-164, 1945.
- [140] R. I. Stephens and H. O. Fuchs, *Metal fatigue in engineering*. Wiley New York, 2001.

- [141] O. Wheeler, "Spectrum loading and crack growth," *Journal of Basic Engineering*, vol. 94, p. 181, 1972.
- [142] J. Willenborg, R. Engle, and H. Wood, "A crack growth retardation model using an effective stress concept," ed: Technical report of air force flight dynamics lab wright-patterson 1971.
- [143] T. Gray and J. Gallagher, "Predicting fatigue crack retardation following a single overload using a modified Wheeler model," *Mechanics of Crack Growth, ASTM STP 590*, pp. 331-344, 1976.
- [144] U. H. Padmadinata, "Investigation of crack-closure prediction models for fatigue in aluminum alloy sheet under flight-simulation loading," PhD thesis, 1990.
- [145] B. Chang, R. Engle, and J. Stolpestad, "Fatigue Crack Growth Behavior and Life Predictions for 2219-T851 Aluminum Subjected to Variable-Amplitude Loadings," p. 3, *Fracture Mechanics, ASTM STP 743*, pp. 3-27, 1981.
- [146] J. Chang, R. Engle, and R. Hiyama, "Application of an improved crack growth prediction methodology on structure preliminary design," *Design of Fatigue and Fracture Resistant Structures, ASTM STP 761*, pp. 278-295, 1982.
- [147] M. Sander and H. Richard, "Fatigue crack growth under variable amplitude loading Part II: analytical and numerical investigations," *Fatigue & Fracture of Engineering Materials & Structures*, vol. 29, no. 4, pp. 303-319, 2006.
- [148] G. Wang and A. Blom, "A modified Dugdale-Barenblatt model for fatigue crack growth predictions under general load conditions," *FFA TN*, vol. 79, 1987.
- [149] D. Aliaga, A. Davy, and H. Schaff, "A simple crack closure model for predicting fatigue crack growth under flight simulation loading," *Mechanics of fatigue crack closure, ASTM STP 982*, pp. 491-504, 1988.
- [150] G. Baudin, R. Labourdette, and M. Robert, "Prediction of crack growth under spectrum loadings with ONERA model," *ONERA, TP*, p. 18, 1988.
- [151] A. De Koning, "A simple crack closure model for prediction of fatigue crack growth rates under variable-amplitude loading," *Fracture Mechanics*, pp. 63-85, 1981.

- [152] D. Dougherty, A. De Koning, and B. Hillberry, "Modelling high crack growth rates under variable amplitude loading," *Advances in fatigue lifetime predictive techniques, ASTM STP 1122*, pp. 214-233, 1992.
- [153] A. DeKoning and D. Dougherty, "Prediction of low and high crack growth rates under constant and variable amplitude loading," 1988.
- [154] M. Sabourin, D. Bouffard, and F. Paquet, "Life prediction of hydraulic runners using fracture mechanics analysis," in *Waterpower XV*, Chattanooga, Tennessee, 2007.
- [155] M. Gagnon, S. A. Tahan, P. Bocher, and D. Thibault, "Impact of startup scheme on Francis runner life expectancy," in *25th IAHR Symposium on Hydraulic Machinery and Systems, September 20, 2010 - September 24, 2010*, Timisoara, Romania, 2010, vol. 12: Institute of Physics Publishing.
- [156] M. Gagnon and D. Thibault, "Response Spectra and Expected Fatigue Reliability: A Look at Hydroelectric Turbines Behavior," *Procedia Engineering*, vol. 133, pp. 613-621, 2015.
- [157] M. Gagnon, S. Tahan, P. Bocher, and D. Thibault, "Impact of startup scheme on Francis runner life expectancy," *IOP Conference Series: Earth and Environmental Science*, vol. 12, no. 1, p. 012107, 2010.
- [158] *ASTM.E8/E8M, Standard Test Methods for Tension Testing of Metallic Materials*, 2011.
- [159] J. Schijve, "Four lectures on fatigue crack growth," Delft University of Technology 1977.
- [160] *ASTM.E647, Standard Test Method for Measurement of Fatigue Crack Growth Rates*, 2011.
- [161] A. Saxena, S. Hudak, J. Donald, and D. Schmidt, "Computer-controlled decreasing stress intensity technique for low rate fatigue crack growth testing," *Journal of Testing and Evaluation*, vol. 6, pp. 167-174, 1978.
- [162] A. Saxena and S. J. Hudak, "Review and extension of compliance information for common crack growth specimens," *International Journal of Fracture*, vol. 14, no. 5, pp. 453-468, 1978.
- [163] J. E. Srawley, "Wide range stress intensity factor expressions for ASTM E 399 standard fracture toughness specimens," *International Journal of Fracture*, vol. 12, no. 3, pp. 475-476, 1976.

- [164] S. C. Forth, J. C. Newman Jr, and R. G. Forman, "On generating fatigue crack growth thresholds," *International journal of fatigue*, vol. 25, no. 1, pp. 9-15, 2003.
- [165] G. Marci, "Fatigue crack propagation threshold: what is it and how is it measured?," *Journal of testing and evaluation*, vol. 26, no. 3, pp. 220-233, 1998.
- [166] J. Colin, A. Fatemi, and S. Taheri, "Fatigue behavior of stainless steel 304L including strain hardening, prestraining, and mean stress effects," *Journal of Engineering Materials and Technology*, vol. 132, no. 2, p. 021008, 2010.
- [167] J. E. Allison, R. C. Ku, and M. A. Pompetzki, "A comparison of measurement methods and numerical procedures for the experimental characterization of fatigue crack closure," in *Mechanics of Fatigue Crack Closure*: ASTM International, 1988.
- [168] M. Sabourin, D. Thibault, D. A. Bouffard, and M. Levesque, "New parameters influencing hydraulic runner lifetime," in *25th IAHR Symposium on Hydraulic Machinery and Systems*, Timisoara, Romania, 2010, vol. 12: Institute of Physics Publishing.
- [169] J. Lanteigne, M. Sabourin, T. Bui-Quoc, and D. Julien, "A comprehensive research programme on crack propagation characteristics of the base material used in hydraulic turbine runners," presented at the Waterpower XV, Chattanooga, USA, 2007.
- [170] J. Lanteigne, M. Sabourin, T. Bui-Quoc, and D. Julien, "The characteristics of the steels used in hydraulic turbine runners," *IAHR 24th Symposium on Hydraulic Machinery and Systems, Foz Do Iguassu, Brazil*, 2008.
- [171] V. W. Trebules, R. Roberts, and R. Hertzberg, "Effect of multiple overloads on fatigue crack propagation in 2024-T3 aluminum alloy," *Progress in flaw growth and fracture toughness testing, ASTM STP 536*, pp. 115-146, 1973.
- [172] T. Iwasaki, A. Katou, and M. Kawahara, "Fatigue crack growth under random loading," *Naval Architecture and Ocean Engineering*, vol. 20, pp. 194-216, 1982.
- [173] T. Nicholas, *High Cycle Fatigue : a Mechanics of Materials Perspective*. Elsevier, pp. 191-193, 2006.
- [174] B. Powell and T. Duggan, "Crack growth in Ti-6Al-4V under the conjoint action of high and low cycle fatigue," *International Journal of Fatigue*, vol. 9, no. 4, pp. 195-202, 1987.

- [175] A. A. Dabayeh and T. H. Topper, "Changes in crack-opening stress after underloads and overloads in 2024-T351 aluminium alloy," *International journal of fatigue*, vol. 17, no. 4, pp. 261-269, 1995.
- [176] J. Schijve, "The significance of fractography for investigations of fatigue crack growth under variable-amplitude loading," *Fatigue and Fracture of Engineering Materials and Structures*, vol. 22, no. 2, pp. 87-100, 1999.
- [177] J. C. McMillan and R. Pelloux, "Fatigue crack propagation under programmed and random loads," *Fatigue crack propagation, ASTM STP 415*, pp. 505-535, 1966.
- [178] M. J. Doré and S. J. Maddox, "Accelerated Fatigue Crack Growth in 6082 T651 Aluminium Alloy Subjected to Periodic Underloads," *Procedia Engineering*, vol. 66, pp. 313-322, 2013.
- [179] T. L. Anderson and T. Anderson, *Fracture mechanics: fundamentals and applications*. CRC press, 2005.
- [180] M. Fine and R. Ritchie, "Fatigue-crack initiation and near-threshold crack growth," *Fatigue and Microstructure*, pp. 245-278, 1979.
- [181] S. Majumdar and J. Morrow, "Correlation between fatigue crack propagation and low cycle fatigue properties," *ASTM STP*, vol. 559, pp. 159-182, 1974.
- [182] R. A. Young, *The Rietveld Method*, 1st ed. Oxford University Press, pp. 1-38, 1993.
- [183] W. D. Callister and D. G. Rethwisch, *Materials Science and Engineering: an Introduction*. Wiley New York, 2007.
- [184] *ASTM.E384, Standard Test Method for Knoop and Vickers Hardness of Materials*, 2012.
- [185] *ASTM.E1382, Standard Test Methods for Determining Average Grain Size Using Semiautomatic and Automatic Image Analysis*, 2004.
- [186] D. Thibault, P. Bocher, M. Thomas, M. Gharghour, and M. Côté, "Residual stress characterization in low transformation temperature 13% Cr–4% Ni stainless steel weld by neutron diffraction and the contour method," *Materials Science and Engineering: A*, vol. 527, no. 23, pp. 6205-6210, 2010.
- [187] D. Thibault, P. Bocher, and M. Thomas, "Residual stress and microstructure in welds of 13% Cr–4% Ni martensitic stainless steel," *Journal of Materials Processing Technology*, vol. 209, no. 4, pp. 2195-2202, 2009.

- [188] J. Newman Jr and I. Raju, "An empirical stress-intensity factor equation for the surface crack," *Engineering Fracture Mechanics*, vol. 15, no. 1, pp. 185-192, 1981.
- [189] J. Barsom, "Fatigue crack growth under variable amplitude loading in various bridge steels," *Fatigue crack growth under spectrum loads, ASTM STP 595*, pp. 217-235, 1976.
- [190] S. Suresh, "Crack deflection: implications for the growth of long and short fatigue cracks," *Metallurgical Transactions A*, vol. 14, no. 11, pp. 2375-2385, 1983.
- [191] M. Hassanipour, Y. Verreman, J. Lanteigne, and J. Q. Chen, "Effect of Periodic Underloads on Fatigue Crack Growth in Three Steels Used in Hydraulic Turbine Runners," *International journal of fatigue*, vol. 85, pp. 40-48, 2015.
- [192] S. Hudak Jr, A. Saxena, R. Bucci, and R. Malcolm, "Development of standard methods of testing and analyzing fatigue crack growth rate data," *Technical Report AFML-TR-78-40, Westinghouse R&D Center, Westinghouse Electric Corporation, Pittsburgh, PA*, pp. 103-107, 1978.
- [193] R. W. Bush, J. K. Donald, and R. J. Bucci, "Pitfalls to avoid in threshold testing and its interpretation," *Fatigue Crack Growth Thresholds, Endurance Limits, and Design, ASTM STP 1372*, pp. 269-284, 2000.
- [194] H. Doker, V. Bachmann, and G. Marci, "A comparison of different methods of determination of the threshold for fatigue crack propagation," in *International Symposium on Fatigue Thresholds*, Warley, UK, vol. 1, pp. 45-58, 1981.
- [195] G. Marci, D. Castro, and V. Bachmann, "Fatigue crack propagation threshold," *Journal of Testing and Evaluation*, vol. 17, no. 1, pp. 28-39, 1989.
- [196] G. Marci, D. Castro, and V. Bachmann, "Closure measurements via a generalized threshold concept," *Fracture Mechanics: Twenty-First Symposium, ASTM STP 1074*, no. 1074, pp. 563-580, 1990.
- [197] G. Marci, "Fatigue crack growth threshold concept and test results for Al- and Ti-alloys," *Fatigue Crack Growth Thresholds, Endurance Limits and Design, ASTM STP 1372*, pp. 81-95, 2000.

- [198] J. Newman, W. Riddell, and R. Piascik, "Effects of  $K_{max}$  on Fatigue Crack Growth Threshold in Aluminum Alloys," *Fatigue crack growth thresholds, endurance limits, and design, ASTM STP 1372*, pp. 63-80, 2000.
- [199] A. Tesch, R. Pippan, and H. Döker, "New testing procedure to determine  $da/dN-\Delta K$  curves at different, constant R-values using one single specimen," *International journal of fatigue*, vol. 29, no. 7, pp. 1220-1228, 2007.
- [200] B. Powell, M. Hawkyard, and L. Grabowski, "The growth of cracks in Ti-6Al-4V plate under combined high and low cycle fatigue," *International journal of fatigue*, vol. 19, no. 93, pp. 167-176, 1997.
- [201] P.A. Deschenes, "private discussion, "Fatigue crack propagation in a residual stress field", MSc Thesis," École polytechnique de Montréal, Université de Montréal, to be published in 2016.
- [202] J. Colin, A. Fatemi, and S. Taheri, "Cyclic hardening and fatigue behavior of stainless steel 304L," *Journal of Materials Science*, vol. 46, no. 1, pp. 145-154, 2011.
- [203] P. Robichaud, "Master thesis," École de technologie supérieure, Université du Québec, 2007.
- [204] M. A. Pompetzki, T. H. Topper, and D. L. DuQuesnay, "The effect of compressive underloads and tensile overloads on fatigue damage accumulation in SAE 1045 steel," *International journal of fatigue*, vol. 12, no. 3, pp. 207-213, 1990.
- [205] G. Marci, "Fatigue crack growth threshold concept and test results for Al-and Ti-alloys," in *Fatigue Crack Growth Thresholds, Endurance Limits, and Design*: ASTM International, 2000.
- [206] D. Taylor, "Fatigue thresholds: their applicability to engineering situations," *International journal of fatigue*, vol. 10, no. 2, pp. 67-79, 1988.